Journal of Materials Chemistry A

Materials for energy and sustainability

rsc.li/materials-a

ROYAL SOCIETY
OF CHEMISTRY
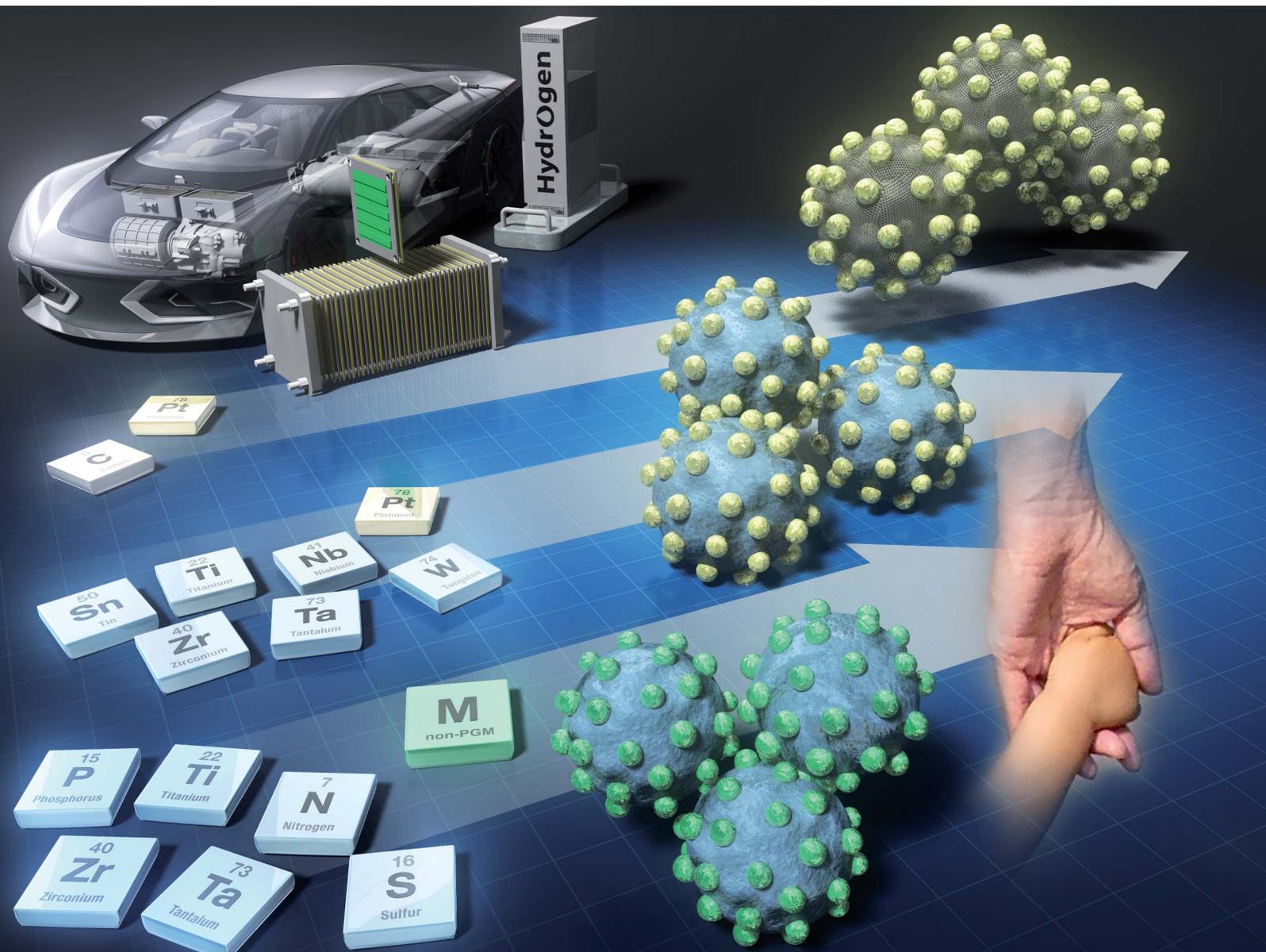
REVIEW ARTICLE
Mitsuharu Chisaka
Review of carbon-support-free platinum and non-platinum
catalysts for polymer electrolyte fuel cells: will they feature
in future vehicles?

REVIEW

Review of carbon-support-free platinum and non-platinum catalysts for polymer electrolyte fuel cells: will they feature in future vehicles?

Mitsuharu Chisaka [ID] *

Polymer electrolyte fuel cells have attracted considerable attention as possible replacements for internal combustion engines (ICEs) in light duty vehicles for journeys typically over 300 miles as well as for medium/heavy duty vehicles. In these vehicle types, carbon black is currently used as the support for platinum (Pt)-based catalysts at the cathode and anode. Carbon black is protected from corrosion during startup/shutdown and unwanted fuel (H_2) starvation by controlling the potential of both electrodes using high-cost system-level measures. Carbon-support-free Pt-based cathode catalysts, which are durable at the high potentials experienced during startup/shutdown due to the reverse current decay mechanism, have therefore been studied extensively over the last two decades. Anodes with impeded oxygen reduction reaction (ORR) activity have also been developed over the last decade to suppress cathode degradation, as the high potential at the cathode is caused by the reduction of contaminated O_2 molecules at the anode. During H_2 starvation, the potential of the anode exceeds that of the cathode, which reverses the cell voltage. Theoretical studies have predicted that binary and nonbinary stoichiometric oxides should be stable under these cathode and anode conditions. This paper focuses on non-carbon supports beyond the typical oxides. Both conductivity and the surface area are crucial in decreasing Pt loading to the platinum group metal (PGM) level used in exhaust gas catalytic converters in conventional gasoline-fueled ICE-powered vehicles. As the conductivity of powders/particles is a particular focus of this article, reports on suboxides and nitrides with metallic characters are covered. Some Pt/non-carbon catalysts exhibit higher ORR activity and durability against startup/shutdown at the cathodes, as well as higher durability against cell reversal at the anodes, compared with conventional carbon-supported Pt or platinum–cobalt (PtCo) catalysts under specific conditions such as high Pt loading or low relative humidity. The origin of these beneficial properties is reviewed. In contrast to these positive results, negative reports of non-carbon supports for the anode and cathode are also highlighted, and the advantages and disadvantages of using non-carbon supports are discussed. Recent improvements in carbon-support-free, non-PGM cathode materials with the use of conductive TiN and associated challenges are also reviewed.

1 Introduction

In many countries, the transport sector generates the largest share of greenhouse gas (GHG) emissions, for example, accounting for 29% of 2022 GHG emissions in the United States (US).[1] Light duty vehicles (LDVs; <10 000 lbs in weight) and medium/heavy duty vehicles (MDVs/HDVs, >10 000 lbs in weight) are responsible for the majority of GHG emissions from the US transport sector (59% and 23% from LDVs and MDVs/HDVs, respectively).[2] Policies to reduce GHG and particulate emissions from LDVs have been implemented worldwide, to reduce the future impact of climate change and to protect

public health. Some cities, regions, and countries have planned to phase out conventional internal combustion engines (ICEs) in LDVs between 2025 and 2040,[3] while California, the first state to introduce emission regulations, plans to phase out ICEs even in MDVs/HDVs. The California Air Resources Board (CARB) aims to phase out ICEs in all buses and trucks by 2045, with earlier goals recently being specified for trucks (2036)[4] and public buses (2029).[5]
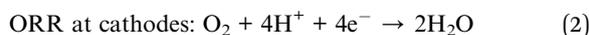
Electric vehicles (EVs) and fuel cell vehicles (FCVs) powered by secondary batteries such as lithium-ion batteries (LIBs) and polymer electrolyte fuel cells (PEFCs), respectively, are potential alternative zero-emission vehicles to replace ICE-powered conventional vehicles. Unlike EVs, FCVs are expected to be used in LDVs for journeys over 300 miles,[6] as well as in MDVs/HDVs.[7] Although a decade has passed since the launch of mid-sedan FCVs in 2014, these vehicles still represent a small

Department of Sustainable Energy, Hirosaki University, 3 Bunkyo-cho, Hirosaki, Aomori 036-8561, Japan. E-mail: chisaka@hirosaki-u.ac.jp; Fax: +81-172-39-3559; Tel: +81-172-39-3559
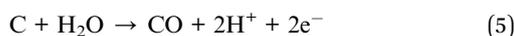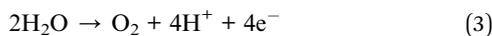
18636 | *J. Mater. Chem. A*, 2024, 12, 18636–18673

This journal is © The Royal Society of Chemistry 2024

percentage of the current market share. Currently, carbon black-supported platinum (Pt/C or Pt/CB) and platinum–cobalt (PtCo/C or PtCo/CB) catalysts are used to catalyze the hydrogen oxidation reaction (HOR) at the anode and the oxygen reduction reaction (ORR) at the cathode in PEFC catalyst layers, respectively.[8,9] Due to the slower kinetics of the ORR compared with the HOR, the platinum loading of the cathode is four-fold that of the corresponding anode.[9] The high platinum loading requirement is assumed to be the greatest cost barrier to the widespread adoption of FCVs.[10] Therefore, efforts have been made over the last two decades to reduce the amount of platinum required in PEFCs by an order of magnitude to ~20 g per 128 kW for a mid-sedan passenger vehicle.[6,8] However, a further reduction to ~6 g per vehicle is necessary to make PEFC-powered passenger vehicles affordable and allow their widespread adoption.[9] This value is equivalent to the mass of platinum group metal (PGM) catalysts required in a catalytic converter used for the exhaust gas of a gasoline-fueled LDV.[11]

In addition to the high costs, carbon-supported platinum-based catalysts currently lack stability, with the instability of platinum/platinum alloy catalysts and the corrosion of carbon supports being two major challenges in improving the durability of PEFC stacks.[10] In an ideal PEFC, the anode and cathode reactions are as follows (eqn (1) and (2)):

$$\text{HOR at anodes: } H_2 \rightarrow 2H^+ + 2e^- \tag{1}$$

$$\text{ORR at cathodes: } O_2 + 4H^+ + 4e^- \rightarrow 2H_2O \tag{2}$$

During the startup and shutdown of PEFCs, the anode becomes contaminated with O_2 molecules originating either from the cathode or the air. Later, the contaminating O_2 molecules are reduced to water as the anode Pt/C catalyzes the ORR (eqn (2)), giving rise to a counter cathode potential of up to ~1.5 V *versus* the reversible hydrogen electrode (RHE) *via* a reverse current decay mechanism.[12] Because in-plane proton conductivity in the catalyst layers is insufficient, protons in the anode ORR are sourced from the counter cathode, at which either the oxygen evolution reaction (OER) *via* eqn (3) or the carbon oxidation reaction (COR) *via* eqn (4) and/or (5) proceeds, as shown in Fig. 1.[12] The carbon black in the PtCo/C cathode is easily oxidized at such high potentials.

$$2H_2O \rightarrow O_2 + 4H^+ + 4e^- \tag{3}$$

$$C + 2H_2O \rightarrow CO_2 + 4H^+ + 4e^- \tag{4}$$

$$C + H_2O \rightarrow CO + 2H^+ + 2e^- \tag{5}$$

The oxidation of carbon black supports has been experimentally confirmed by monitoring CO_2 gas formation at PEFC cathodes.[13] The PtCo nanoparticles on the carbon supports can no longer be used once the carbon supports are corroded. The startup/shutdown cycles cause more severe damage to the performance of conventional PEFC catalyst layers employing carbon black *via* the corrosion than load cycles, which induce the instability of platinum/platinum alloys.[14] To avoid this

issue, carbon supports are usually protected by system-level measures, such as reducing the cathode air flow rate during shutdown to minimize O_2 diffusion to the anode through a membrane and injecting a small amount of H_2 into the anode during FCV off-time to react with O_2 contaminants.[15] These measures further increase the cost of FCVs.

The COR ends when the contaminant O_2 molecules are consumed after startup or when the load current is switched off after the shutdown of PEFCs. The cathode catalysts are thus left at a high potential for a short time during startup and shutdown if the system-level measures described above are not taken. The Fuel Cell Commercialization Conference in Japan (FCCJ) defined a protocol for evaluating the durability of FCVs against startup/shutdown, in which the potential was cycled between 1.0 and 1.5 V at a high scan rate of 0.5 V s^{-1} in both a half-cell and a single cell, in 2011.[16] The protocol has been most widely used in the last decade and was later followed by the US Department of Energy (DOE) protocol, which set an identical potential range and scan rate.[17] In the current review, this protocol is denoted as the "FCCJ startup/shutdown cycle" for the sake of simplicity. The protocols for evaluating the durability against the normal driving mode of FCVs have also been defined by the FCCJ and DOE, and both protocols have been updated since 2007. The FCCJ revised the protocol only once in 2011, in which the potential was cycled with symmetric rectangular waves (held at 0.6 V for 3 s as "load on" and then held at 1.0 V for 3 s as "load off" mode)[16] and has been most widely used to date. The DOE protocol has been revised several times. In 2016, rectangular waves similar to those described in the FCCJ were set, and the sole difference was the upper potential at 0.95 V in the DOE protocol.[17] These protocols are hereafter referred to as FCCJ or DOE load cycles.

Researchers in this community have paid less attention to the anode catalyst layers and have focused on developing cathode counterparts. The kinetics of the HOR in PEFC anodes are 3–4 orders of magnitude faster than those of the ORR in the cathodes[18] to achieve low anode platinum loading, which is one-quarter of that of the cathode,[9] while maintaining an anode potential below ~0.1 V *versus* RHE. The standard electrode potential for eqn (4) and (5) is 0.207 and 0.518 V, respectively, *versus* the standard hydrogen electrode (SHE), and thus the COR does not proceed in Pt/C anodes during the normal operation of FCVs. However, the COR proceeds under some operating conditions such as "sub-zero startup," which refers to startup at temperatures below 273 K to form ice, which blocks hydrogen flow fields, rapid load change with high fuel utilization, uneven current distribution in flow fields, and uneven reactant flux distributions between cells in a stack. Under these conditions, there is insufficient H_2 gas for oxidation to maintain the current, and instead, both the OER (eqn (3)) and the COR (eqn (4) and/or (5)) proceed at the H_2-starved anode to compensate for the current shortage. The anode potential increases to reverse the cell voltage and achieve a minus value during H_2 starvation, as shown in Fig. 2.[19] The anode potential after this phenomenon, which is called a cell reversal, shortly increases beyond 1.5 V *versus* RHE, and continuously increases. Similar to the cathode during startup/shutdown, carbon supports are easily oxidized *via*
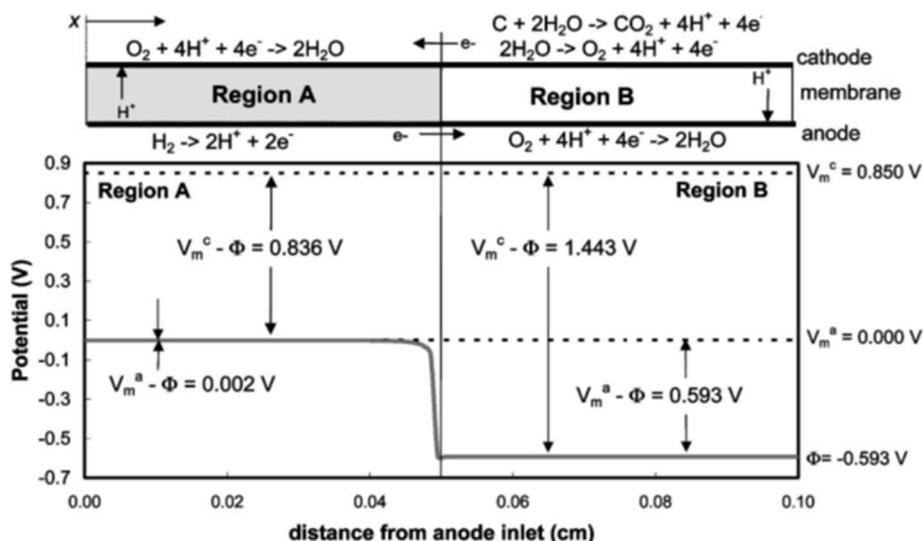
Fig. 1 Potential distributions along the anode flow path under reverse current conditions, where V_m^c, V_m^a and Φ denote the potential of cathode metal, anode metal and electrolyte, respectively. Reproduced with permission.[12] Copyright 2005, The Electrochemical Society.
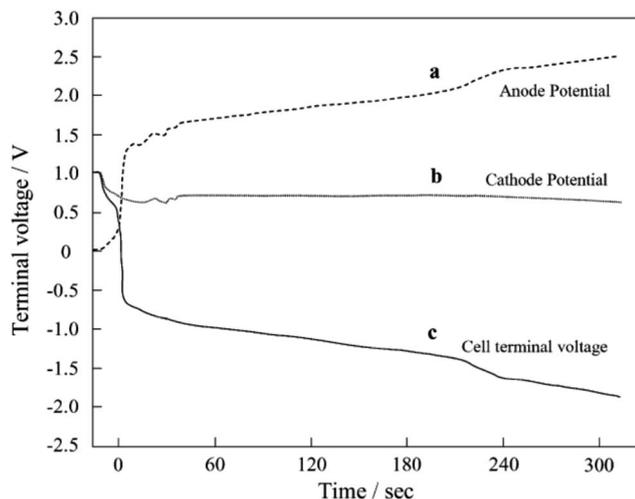

Fig. 2 (a) Anode potential, (b) cathode potential, and (c) cell voltage *versus* time curves during cell reversal. Reproduced with permission.[19] Copyright 2004, Elsevier.

eqn (4) at such high potentials. The evolved O_2 gas at the carbon-free platinum black anode[20] and Pt/C anode[21] due to the OER (eqn (3)) and CO_2 gas at the Pt/C anode due to the COR (eqn (4))[21,22] during cell reversal were experimentally confirmed by gas analyses. Interestingly, Baumgartner *et al.* reported that CO_2 and CO gases have also been detected from PEFC anodes during cell reversal, although the precise mechanism for CO formation has not been clarified.[22]

Upon cell reversal, the carbon supports at the Pt/C anodes face corrosion for longer durations than the PtCo/C cathodes during startup/shutdown, considerably reducing cell performance.[19–21] In general, the COR proceeds with a high overpotential and is thus accompanied by heat loss, which leads to pinholes in the membrane.[23,24] Anode H_2 fuel and cathode air can be mixed through the pinholes to further generate heat,[24]

which may cause a fire in the worst case. To avoid cell reversal, current system-level measures include monitoring all cell voltages[25] and low fuel utilization. However, once again, these measures increase the system cost of FCVs.[25]

The issues described in relation to currently available carbon black supports at the anode and cathode of the PEFC catalyst layers have motivated researchers to develop carbon-support-free platinum-based catalysts. Furthermore, the scarcity and price of PGMs have driven the development of PGM-free catalysts. The ultimate catalyst is therefore a carbon-support-free, non-PGM catalyst. In this paper, non-carbon-support alternatives to carbon black in the cathode and anode of PEFCs are reviewed first in Section 2. Pathways to enhance the startup/shutdown durability of cathodes developed in the last two decades include durable non-carbon cathode supports and HOR-selective anodes that impede the undesired ORR at the anode. As the conductivity of the new catalyst is crucial in all pathways, this paper focuses on conductivity at the bulk and the particulate, including contact resistance. Non-carbon anode supports that are durable against cell reversal have recently been developed with and without OER catalysts. Some negative reports on non-carbon supports in the anode and the cathode are also highlighted, and the merits and demerits of the use of non-carbon supports are discussed at the end of Section 2. The ultimate carbon-support-free, non-PGM catalysts are then reviewed in Section 3. Finally, the possible use of these carbon-support-free catalysts in FCVs is summarized, including the challenges and recommended experimental conditions for future work.

2 Carbon-support-free platinum/platinum alloy catalysts

2.1 Cathode catalysts

The cathode potential operates between 0.6 and 0.95/1.0 V *versus* RHE in FCVs in a normal operation mode.[16,17] The normal

18638 | *J. Mater. Chem. A*, 2024, **12**, 18636–18673

This journal is © The Royal Society of Chemistry 2024

Li Li^+	Be Be^{2+}											B $H_3BO_3(a)$	C $CO_2(a)$ $CO_2(g)$	N (N/A)	O (N/A)	F (N/A)	
Na Na^+	Mg Mg^{2+}											Al Al^{3+}	Si $H_2SiO_3(a)$ (H_4SiO_4)	P $H_4P_2O_7(a)$	S HSO_4^-	Cl (N/A)	
K K^+	Ca Ca^{2+}	Sc Sc^{3+}	Ti TiO_2	V VO_4^-	Cr Cr^{3+}	Mn Mn^{2+}	Fe Fe^{3+} (Fe_2O_3)	Co Co^{2+}	Ni Ni^{2+}	Cu Cu^{2+}	Zn Zn^{2+}	Ga Ga^{3+}	Ge GeO_2	As $HAsO_4(a)$	Se $H_2SeO_3(a)$	Br (N/A)	
Rb Rb^+	Sr Sr^{2+}	Y Y^{3+}	Zr ZrO^{2+}	Nb Nb_2O_5	Mo MoO_3	Tc (N/A)	Ru RuO_2	Rh $RhO_2(g)$	Pd PdO_2	Ag Ag^+	Cd Cd^{2+}	In In^{3+}	Sn SnO_2	Sb Sb_2O_5	Te $Te(OH)_3^+$ (H_2TeO_4)	I (N/A)	
Cs Cs^+	Ba Ba^{2+}		Hf HfO_2	Ta Ta_2O_5	W $O_2W(OH)_2$	Re ReO_4^-	Os $OsO_4(a)$ (OsO_2)	Ir IrO_2	Pt Pt	Au Au	Hg (N/A)	Tl Tl^+	Pb Pb^{2+}	Bi Bi_2O_3	Po (N/A)	At (N/A)	

Fig. 3 Most stable substances under typical polymer electrolyte fuel cell (PEFC) cathode conditions derived from thermochemically calculated pH–potential diagrams. The potential and the temperature were set at 1.0 V *versus* the reversible hydrogen electrode (RHE) at pH = 0 and 353 K, respectively. Insoluble elements/compounds are shown in red, and the gray background indicates N/A. Reproduced with permission.[26] Copyright 2010, The Electrochemical Society.

potential range is much lower than that during startup/shutdown as mentioned in Section 1, and thus the cathode environment in the normal mode is gentler to catalysts compared with during startup/shutdown. However, few elements are stable even in the normal operating mode of PEFC cathodes, as shown in Fig. 3. Sasaki *et al.* reported the stability of 54 elements in PEFC cathodes, in which the potential was set at 1.0 V *versus* RHE at pH = 0 by using thermochemical calculations.[26] The temperature was set at 353 K, which is the operating temperature of current PEFCs employing a perfluorosulfonate ionomer (PFSI) membrane such as Nafion™ produced by DuPont. Most elements exist as ions that may leach out, while stable elements exist as binary oxides, oxide hydrates, or metals under the given conditions. Pt is stable as the metallic element according to Fig. 3, while it is well-known to dissolve as Pt ions and then deposit on other Pt particles (Ostwald ripening) in the cathodes during long-term operation at 1.0 V. It then migrates from the cathodes to membranes, where it is redeposited to form a "Pt band" in the membranes.[27] This inconsistency could be due to (i) deficiencies in the database, which describes the most stable substances,[26] while minor soluble species such as Pt^{2+} and Pt^{4+} cause gradual Ostwald ripening, (ii) potential cycling in the normal driving mode (so-called "load cycling"), which accelerates Pt dissolution during the operation of FCVs,[27] and (iii) small amounts of hydrogen peroxide byproducts formed during the ORR *via* a two-electron reaction represented by eqn (6) as they dissolve Pt.[28,29]

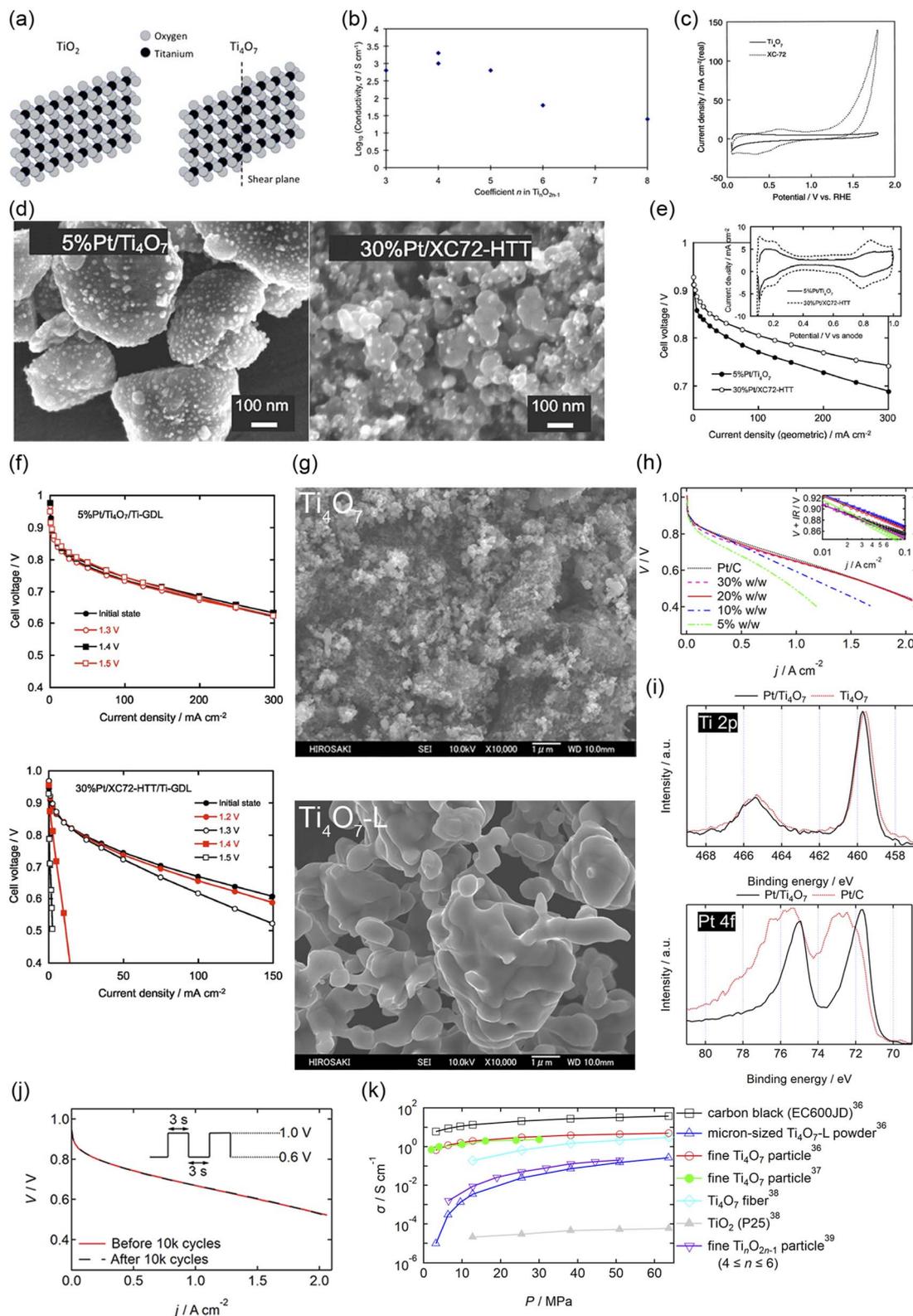$$O_2 + 2H^+ + 2e^- \rightarrow H_2O_2 \qquad (6)$$
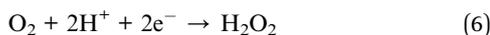
Ten years after the publication of the work by Sasaki *et al.*, the Nørskov group investigated the stability of 47 814 nonbinary metal oxides at 0.6–1.0 V (for the ORR) and 1.2–2.0 V (for the OER) *versus* RHE at pH = 0 using theoretical calculations.[30] The stable candidates screened were Sb/Ti/Sn/Ge/Mo/W-based oxides. These theoretical calculation results based on binary[26] and nonbinary[30] oxides suggest that the abovementioned oxides are the most promising candidates for stable-support alternatives to the currently available carbon black. However, it is noted that there may be exceptions in the elements excluded from the screening using theoretical calculations. Lv *et al.* reported that nano-sized ZrO_2 particles are electrochemically stable after 48 h of potential holding at 1.2 V *versus* RHE in 0.5 mol dm^{-3} H_2SO_4 solution, displaying negligible changes in the cyclic voltammograms (CVs).[31] ZrO_2 is dissolved away during the harsh oxidative treatment used in the study by Lv *et al.*, judging from Fig. 3, while it survives as it was sufficiently stable or the dissolution process was kinetically slow. Both the instability of Pt[27] and the stability of ZrO_2 (ref. 31) reported in previous studies are inconsistent with Fig. 3 and suggest the absence of a perfect database for screening stable candidates in the PEFC cathodes, in which several factors affect the stability. In particular, factors (i)–(iii) mentioned in the previous paragraph are not simultaneously included in any database and therefore, in this subsection, cathode Pt/Pt-alloy catalysts on non-carbon supports are reviewed without limiting the scope to stoichiometric oxides. Suboxides, oxides and nitrides are considered as their particles can show high conductivity after applying pressure below that of hot-pressing membrane electrode assemblies (MEAs), typically 10 MPa. The conductivity is comparable to or only one order of magnitude lower than that of carbon black at room temperature, at least in some compositions.

2.1.1 Platinum/platinum alloy catalysts on oxide supports

2.1.1.1 Titanium suboxide-supported catalysts. Oxide materials have been assumed to be the most stable supports for PEFC cathodes, and thus many research groups have focused on developing oxide supports. The predicted stable binary oxides shown in Fig. 3 have one common theme in that the metals are at the highest oxidation state, which is reasonable for stability

This journal is © The Royal Society of Chemistry 2024

J. Mater. Chem. A, 2024, **12**, 18636–18673 | **18639**

Fig. 4 (a) Crystal structure of rutile TiO_2 and Ti_4O_7. (b) A conductivity *versus* n in Magnèli-phase Ti_nO_{2n-1} curve. Reproduced with permission.[33] Copyright 2010, Elsevier. (c) Cyclic voltammograms (CVs) of Ti_4O_7 and carbon black; Vulcan XC-72 electrodes in membrane electrode assemblies (MEAs) supplied with N_2 at a scan rate of 100 mV s^{-1} at 353 K. The counter electrodes were made with commercial 40% w/w Pt/C and supplied with fully humidified H_2 to be a reversible hydrogen electrode (RHE). Therefore, the counter electrode also served as a reference electrode. Reproduced with permission.[34] Copyright 2005, Elsevier. (d) Scanning electron microscopy (SEM) images of 5% w/w Pt/Ti_4O_7 and 30% w/w Pt/C after annealing at 1273 K for 3 h under H_2, denoted as 30% w/w Pt/XC72-HTT. (e) Cell voltage *versus* current density curves for MEAs fabricated using 5% w/w Pt/Ti_4O_7 and 30% w/w Pt/XC72-HTT in the cathode at 353 K. Platinum loading was set at 0.24 and 0.29 mg$_{Pt}$ cm^{-2} for

18640 | J. Mater. Chem. A, 2024, 12, 18636–18673

This journal is © The Royal Society of Chemistry 2024

in the highly oxidative environment of the PEFC cathodes. Except for PGM oxides, which have a black color, these oxides are all white or yellow in color, indicating their insulating nature. The geometrical current density of PEFCs is on the order of A cm^{-2}, which is at least two orders of magnitude higher than that of conventional LIBs or even post-LIBs, such as state-of-the-art solid-state lithium batteries.[32] Insulating materials have been used in the electrodes of the abovementioned batteries with low current densities, although they are used with difficulty in PEFCs with high current densities. Therefore, several strategies, such as introducing oxygen vacancies or doping other metals, have been used to enhance the conductivity of stable binary non-PGM oxides.

Among various oxides, titanium oxides have been most widely investigated as supports for PEFC cathodes owing to their high conductivity and natural abundance. Fig. 4(a) shows the crystal structure of rutile TiO_2 and Ti_4O_7, one of the members of the Magnèli-phase titanium suboxide group, Ti_nO_{2n-1} ($4 \leq n \leq 10$), which were discovered by Andersson and Magnèli in 1956.[33,40] Rutile TiO_2, the most thermodynamically stable and most common titanium dioxide polymorph in nature, consists of TiO_6 octahedra in which six oxygen atoms at the corners surround a titanium atom at the center. Each octahedron shares two opposite edges and free corner oxygen atoms to link adjacent octahedra. In Ti_nO_{2n-1}, oxygen vacancies are present in every nth layer to produce shear planes. The electrical conductivities reported to date are shown in Fig. 4(b). The highest value at $n = 4$ is above 1000 S cm^{-1} at room temperature,[41] which is 16 orders of magnitude higher than that of rutile TiO_2 and comparable to that of graphite.[42] The reported high conductivity motivated several researchers to develop Ti_4O_7 as supports for PEFC cathodes. Pioneering studies by Ioroi *et al.* in the 2000s displayed the significant potential of this material, although issues remained in terms of their use in vehicles. Fig. 4(c) shows the CVs of Ti_4O_7 powder synthesized by annealing commercial TiO_2 powder at 1323 K for 6 h under H_2 gas and commercial carbon black particles, Vulcan XC-72, in a PEFC single cell. Vulcan XC-72 has been the standard carbon support in Pt/C until the 2000s. Ti_4O_7 exhibited high stability up to 1.8 V *versus* RHE to show a small anodic current, whereas Vulcan XC-72 was oxidized to show a rapid increase in the

anodic current as the potential increased above 0.9 V. These CVs also indicate that ~20% of the Ti_4O_7 surface was electrochemically active, which is much lower than the ~68% calculated for Vulcan XC-72 using the loading, theoretical double-layer capacitance and Brunauer–Emmett–Teller (BET) surface area.[34] The electrochemically active surface area (ECSA) refers to the area which is accessible to protons and electrons. The low ECSA value of Ti_4O_7 may be due to the low coverage of PFSI on Ti_4O_7 powder, as PFSI produces paths for protons, or the low electrical conductivity of Ti_4O_7 powder, as discussed later. The BET surface area of the Ti_4O_7 powder was reported to be 0.95 m^2 g^{-1}, which is two orders of magnitude lower than that of Vulcan XC-72, 250 m^2 g^{-1}.[34] The low surface area is due to its high synthesis temperature of 1323 K, which induces agglomeration of Ti_4O_7 powder to yield sub-micrometer to micrometer-sized particles. Fig. 4(d) shows the scanning electron microscopy (SEM) images of Ti_4O_7-supported platinum (Pt/Ti_4O_7) catalysts and commercial carbon-supported platinum catalysts after annealing at 1273 K for 3 h under H_2 gas (Pt/XC72-HTT). The bright spots in these images represent Pt particles. Owing to the small surface area of large Ti_4O_7 powder, the mass fraction of Pt was controlled to 5% w/w to prevent Pt particle coagulation, which is much lower than that in Pt/XC72-HTT, at 30% w/w.[35] The 5% w/w Pt/Ti_4O_7 catalysts displayed a lower cell voltage at any current density in a single cell than 30% w/w Pt/XC72-HTT owing to the smaller ECSA, as shown in Fig. 4(e). Although the initial performance of 5% w/w Pt/Ti_4O_7 was lower, the stability at high potentials was greater compared with 30% w/w Pt/XC72-HTT, as shown in Fig. 4(f). An MEA with the 5% w/w Pt/Ti_4O_7 cathode catalyst layer on a titanium gas diffusion layer (Ti-GDL) displayed negligible changes in cell voltages at any current density, even after holding the cell voltage at 1.5 V for 1 h. In contrast, an MEA with 30% w/w Pt/XC72-HTT/Ti-GDL deteriorated to complete loss of ORR activity. The CVs during voltage holding indicate that XC72-HTT was oxidized from 1.2 V. Control experiments using conventional carbon cloth GDLs revealed that even carbon atoms in the GDLs were oxidized at 1.5 V for 1 h, and thus carbon should be eliminated from both catalyst layers and GDLs under harsh conditions without using high-cost potential protecting systems.[35] These pioneering studies by Ioroi *et al.* clearly indicate the advantages of Ti_4O_7,

---

5% w/w Pt/Ti_4O_7 and 30% w/w Pt/XC72-HTT, respectively. The anode and cathode gases were fully humidified H_2 and O_2, respectively. The inset shows their corresponding CVs. (f) Cell voltage *versus* current density curves for MEAs fabricated using 5% w/w Pt/Ti_4O_7 and 30% w/w Pt/XC72-HTT in the cathode catalyst layer formed on a hydrophobic titanium fiber gas diffusion layer (Ti-GDL) before (initial state) and after voltage holding at 1.2–1.5 V for 1 h at 353 K. Reproduced with permission.[35] Copyright 2008, The Electrochemical Society. (g) Field emission (FE)-SEM images of (top) fine Ti_4O_7 particles synthesized *via* a carbothermal reduction reaction route and (bottom) micrometer-sized Ti_4O_7 powder synthesized from commercial TiO_2 powder (Ti_4O_7-L). (h) Cell voltage *versus* current density (V–j) curves of five MEAs fabricated using commercial 46% w/w Pt/C and Pt/Ti_4O_7 with four different Pt mass fractions, 5%, 10%, 20%, and 30% w/w in the cathode at 353 K. Pt/C was used in the anode of all MEAs and the Pt loading at the anode and cathode was 0.2 and 0.5 mg$_{Pt}$ cm^{-2}, respectively. The anode and cathode gases were fully humidified H_2 and O_2 with 83% relative humidity (RH), respectively. (i) Ti 2p and Pt 4f X-ray photoelectron spectra of the 20% w/w Pt/Ti_4O_7 catalyst (solid curves). For reference, a Ti 2p spectrum of Ti_4O_7 and a Pt 4f spectrum of commercial Pt/C are shown by the dashed curves. (j) V–j curves of an MEA fabricated using 20% w/w Pt/Ti_4O_7 in the anode and cathode before (solid curve) and after (dashed curve) 10 000 voltage cycles with symmetric rectangular waves (held at 0.6 V for 3 s and then at 1.0 V for 3 s); hereafter referred to as FCCJ load cycles. Pt loading and operating conditions are identical to those of (h). Reproduced with permission.[36] Copyright 2021, Royal Society of Chemistry. (k) Powder/particle conductivity *versus* pressure (σ–P) curves of commercial carbon black, Ketjen Black EC600JD, and micron-sized Ti_4O_7-L powders shown at the bottom of (g),[36] fine Ti_4O_7 particles,[36,37] Ti_4O_7 fibers, commercial TiO_2, P25 particles[38] and fine $Ti_{2n}O_{2n-1}$ ($4 \leq n \leq 6$) particles.[39] Reproduced with permission.[36–39] Copyright 2021, Royal Society of Chemistry, Copyright 2024, Royal Society of Chemistry, Copyright 2016, Elsevier and Copyright 2011, The Electrochemical Society.

This journal is © The Royal Society of Chemistry 2024

J. Mater. Chem. A, 2024, **12**, 18636–18673 | 18641

while revealing challenges for their use in vehicles. The former include the high stability after holding the cell voltage at 1.5 V for 1 h and the latter include low initial cell performance and a low Pt mass fraction in Pt/Ti_4O_7 due to the large Ti_4O_7 powder. A strong reductive atmosphere such as pure hydrogen at a high temperature above 1273 K has been required to synthesize Ti_4O_7 from natural TiO_2.[33] During high-temperature annealing, the size of the starting material TiO_2 increases to form agglomerated Ti_4O_7 powder, typically of a micrometer order. Indeed, the most widely used commercial Ti_4O_7, Ebonex® has a size of 3–500 μm.[33] A small quantity of Pt particles can readily be deposited on such large Ti_4O_7 powder, and the resulting catalyst layer thickness may be much larger than that of the current PtCo/C catalyst layers, which is typically ∼10 μm.[9] Recent analyses on the MEAs of the latest FCV revealed an anode and cathode catalyst layer thickness of 3.42 and 8.81 μm, respectively.[8] A particle size of around 100 nm is needed to increase the surface area of Ti_4O_7 to an order of at least one hundred m^2 g^{-1} (equivalent to that of conventional carbon black), and thus to increase the mass fraction of Pt without increasing the Pt size to enhance the cell performance. Ioroi et al. later developed a new pulsed ultraviolet (UV) laser irradiation method to synthesize Ti_nO_{2n-1} particles without using high-temperature annealing. Although the crystal structure was not a single Ti_4O_7 phase, the BET surface area was successfully increased to 20 m^2 g^{-1} after optimizing the solvent to acetonitrile, in which TiO_2 nanoparticles were irradiated using a UV laser.[43] Seneviratne et al. developed Ti_4O_7 nanofiber supports by annealing electrospun TiO_2 nanofibers at 1323 K for 6 h under a 50% v/v H_2/N_2 gas mixture. The BET surface area, 51 m^2 g^{-1} of TiO_2 nanofibers, decreased to 6 m^2 g^{-1} of Ti_4O_7 nanofibers during the annealing process.[44] Yao et al. successfully synthesized Ti_4O_7 nanofiber supports with a BET surface area of 26 m^2 g^{-1} by annealing SiO_2-coated TiO_2 nanotubes at 1323 K for 4 h under pure H_2 gas. The SiO_2 shell covering the Ti_4O_7 fibers was removed using 2% HF solution for 45 h. Although such a multistep method, combined with the use of toxic HF, may increase the cost of synthesis, the size growth and decrease in the surface area during high-temperature annealing were successfully suppressed by the SiO_2 shell. The durability of the Ti_4O_7 fiber-supported Pt nanoparticles outperformed the durability of commercial Pt/C catalysts against accelerated degradation tests (ADTs), in which the potential was cycled between 0.6 and 1.4 V versus SHE in a half-cell employing 0.5 mol dm^{-3} H_2SO_4 solution. The high durability was reported due to (1) highly stable Ti_4O_7 fiber supports and (2) strong metal-support interactions (SMSIs), as confirmed by X-ray photoelectron spectroscopy (XPS). The Pt 4f binding energy of the Pt/Ti_4O_7 fibers shifted lower, and the changes in binding energy during ADTs were smaller compared with those of commercial Pt/C.[45] The term SMSI was first introduced by Tauster et al. in 1978 to explain the dramatic changes in the chemisorption properties of Group VIII noble metals on TiO_2[46] and is believed to be the origin of the enhancement in many catalytic properties of supported metal catalysts, including the ORR activity of carbon-free PEFC cathode catalysts.[47] As Pt particles can bind to Ti_4O_7 more strongly than to carbon, Al_2O_3, and SiO_2, they are less

mobile on Ti_4O_7 to suppress Pt particle size growth with increasing temperature compared with Pt/C, Pt/Al_2O_3, and Pt/SiO_2.[48,49] Therefore, the durability of Pt/Ti_4O_7 in PEFC cathodes is expected to exceed that of Pt/C. The SiO_2 coating route was also used for the synthesis of particulate Ti_4O_7 with a BET surface area of 6 m^2 g^{-1} by the Hwang group.[50] Although significant efforts have been made to suppress the growth of Ti_4O_7 support size, the reported BET surface area was below 100 m^2 g^{-1} as mentioned above, and a single-cell performance with Pt/Ti_4O_7 cathodes comparable to that with their Pt/C counterpart has not been reported until recently. In 2021, we successfully synthesized >2 g of Ti_4O_7 fine particles with a BET surface area of 172 m^2 g^{-1} via an inexpensive carbothermal reduction reaction route, as shown in Fig. 4(g). Pt nanoparticles were highly dispersed on the Ti_4O_7 particles, and the Pt mass fraction was successfully increased to 30% w/w owing to the high surface area of Ti_4O_7. The average Pt particle size of the optimized 20% w/w Pt/Ti_4O_7 determined by a CO pulse method was 4.2 nm, slightly exceeding that of commercial Pt/C, and the single-cell performance with the Pt/Ti_4O_7 cathode was similar to that of the Pt/C cathode, as shown in Fig. 4(h). The SMSIs between Pt nanoparticles and Ti_4O_7 supports were observed, as shown in Fig. 4(i). The Ti $2p_{3/2}$ peak binding energy shifted to higher binding energy regions after Pt nanoparticles were supported, indicating the decreased electron density of titanium in Pt/Ti_4O_7 compared with Ti_4O_7. Pt/Ti_4O_7 showed a lower Pt $4f_{7/2}$ peak binding energy than commercial Pt/C, indicating that the electron density of Pt nanoparticles in Pt/Ti_4O_7 exceeded that of Pt/C. These Ti 2p and Pt 4f spectra indicate that the electrons from the titanium atoms in Ti_4O_7 supports were transferred to the platinum atoms in Pt nanoparticles.[36] These results are in good agreement with previous oxide-supported platinum catalysts, in which SMSIs are reported to enhance ORR activity.[51–53] As the durability against startup/shutdown cannot be evaluated with conventional GDLs utilizing carbon paper or carbon cloth,[35] the durability of Pt/Ti_4O_7 against FCCJ load cycles was evaluated with an MEA utilizing Pt/Ti_4O_7 in the anode and cathode, as shown in Fig. 4(j). The cell voltage, V, did not change at any current density, j, after 10 000 cycles, indicating that HOR and ORR activity was retained during the cycles. The load cycle durability is among the highest in the state-of-the-art Pt/oxide catalysts, as shown in Table 1. The enhanced cell performance is due to (1) the high surface area which allows an increased Pt mass fraction without increasing the Pt nanoparticle size and (2) the high conductivity, as shown in Fig. 4(k). The conductivity of powders, σ, is determined by bulk and contact resistance, and the latter depends on the morphology, size, and size distributions. In many papers on Pt or Pt-alloy/non-carbon catalysts, only one σ-value of non-carbon supports measured at a specific pressure, P, has been reported. The selected P differs across these papers, and the specific P value is not even described in some papers, making it difficult to compare the reported σ-values of non-carbon supports against each other. Some researchers reported σ at various P values, and the σ values of Ti_4O_7,[36–38] mixed Magnèli-phase Ti_nO_{2n-1} ($4 \leq n \leq 6$),[39] commercial TiO_2 (ref. 38) and commercial carbon black[38] are compared in Fig. 4(k). The σ-value of fine Ti_4O_7 particles shown

18642 | J. Mater. Chem. A, 2024, 12, 18636–18673

This journal is © The Royal Society of Chemistry 2024

Table 1 Load cycle durability of Pt or Pt–Co supported on various oxides evaluated in a single cell[g]

Cathode catalyst[a]	w_{Pt}	m_{Pt}[b]	Back pressure[c]	Load cycle protocol	T_{cell}[d]	Oxidant	ΔV[e]	Reference
Pt/Ti$_4$O$_7$	20% w/w	0.5	Ambient pressure	0.6 V (3 s)–1.0 V (3 s)	353 K	O$_2$ 83% RH	0 mV	36
Pt/Ti$_3$O$_5$Mo$_{0.2}$Si$_{0.4}$	20% w/w	0.2	N/A[f]	0.6 V–1.0 V at 0.5 V s^{-1} (triangle waves)	323 K	O$_2$ 100% RH	16 mV	54
Pt/TiO$_2$	60.4% w/w	0.4	0.27 MPa-absolute	0.7 V (30 s)–0.9 V (30 s)	353 K	Air 100% RH	0.09 V	55
Pt/Ta$_{0.3}$Ti$_{0.7}$O$_2$	20% w/w	0.4	Ambient pressure	0.6 V (3 s)–0.95 V (3 s)	353 K	Air 75% RH	~15 mV	56
Pt/RuO$_2$-TiO$_2$	40% w/w	0.35	N/A	0.6 V (3 s)–0.95 V (3 s)	353 K	Air 100% RH	0.03 V	14
Pt/IrO$_2$-TiO$_2$	8.9% w/w	0.45	0.15 MPa-absolute	0.6 V–1.0 V at 50 mV s^{-1} (triangle waves)	353 K	Air 100% RH	0.07 V	57
						O$_2$ 100% RH	0.07 V	
Pt/Cu,N-doped TiO$_2$	40% w/w	0.2	Ambient pressure	0.6 V–1.0 V at 50 mV s^{-1}	348 K	O$_2$ 100% RH	0.07 V	58
Pt$_3$Co/Sn$_{0.98}$Nb$_{0.02}$O$_2$-VGCF	N/A	0.3	N/A	0.6 V (3 s)–1.0 V (3 s)	353 K	Air 100% RH	0.09 V	59
Pt/Nb-doped SnO$_2$	18.5% w/w	0.1	Ambient pressure	0.6 V (3 s)–0.94 V (60 s)	353 K	O$_2$ 100% RH	0.08 V	60
Pt/Sb-doped SnO$_2$	20% w/w	0.4	Ambient pressure	0.6 V (3 s)–0.95 V (3 s)	353 K	Air 90% RH	0.20 V	61

[a] Anode catalysts were commercial Pt/C except for ref. 36, in which 20% w/w Pt/Ti$_4$O$_7$ was used for the anode and cathode. [b] Cathode platinum loading in mg$_{Pt}$ cm^{-2}. [c] Cathode back pressure. [d] Cell temperature. [e] Decrease in V at $j = 1$ A cm^{-2} after 10 000 cycles except for ref. 54, 55, 59 and 61, which used 50 000 (assumption, the cycle number was not clearly described in ref. 54) and 5000 cycles, respectively. Ref. 57 and 60 report a decrease in $V + IR$ after 10 000 cycles. [f] It was 0.1 MPa without clear descriptions as gauge or absolute pressure in ref. 54. [g] N/A, not applicable; RH, relative humidity; VGCF, vapor-grown carbon fiber.

in Fig. 4(g) is high (0.7 S cm^{-1} from the lowest P of 3 MPa) and exceeds 1 S cm^{-1} at $P \geq 6$ MPa, which is just one order of magnitude lower than that of commercial carbon black used in Pt/C (Ketjen Black EC600JD). The results shown in Fig. 4(h) and (k) suggest that the σ-value of fine Ti$_4$O$_7$ particles was sufficiently high not to restrict cell performance, at least under the conditions used. Li *et al.* recently synthesized fine Ti$_4$O$_7$ particles using our carbothermal reduction reaction route with some modifications.[37] The σ-value reported in our paper[36] was well reproduced by Li *et al.*[37] as shown by the open[36] and filled circles,[37] respectively, in Fig. 4(k). The 172 m^2 g^{-1} BET surface area reported in our paper[36] was also well reproduced by Li *et al.*, at 166 m^2 g^{-1}.[37] Micrometer-sized Ti$_4$O$_7$ synthesized by a conventional method, annealing commercial TiO$_2$ powder under a reductive atmosphere (denoted as Ti$_4$O$_7$-L), resulted in a σ-value five orders of magnitude lower, at $P = 3$ MPa, two orders of magnitude lower at $P = 25$ MPa compared with fine Ti$_4$O$_7$ particles. This differing dependence of σ on P may be the result of the difference in size, as shown in Fig. 4(g). As the particle size decreases, the tensile strain increases, distorting the crystal lattice to incorporate oxygen vacancies, which is known to increase the conductivity of oxides.[62] Indeed, Raman spectra showed that fine Ti$_4$O$_7$ particles contained a large number of oxygen vacancies on the surface.[36] Thus, contact resistance between Ti$_4$O$_7$ particles, which is dominant for σ at low P, is suppressed owing to the high surface conductivity.
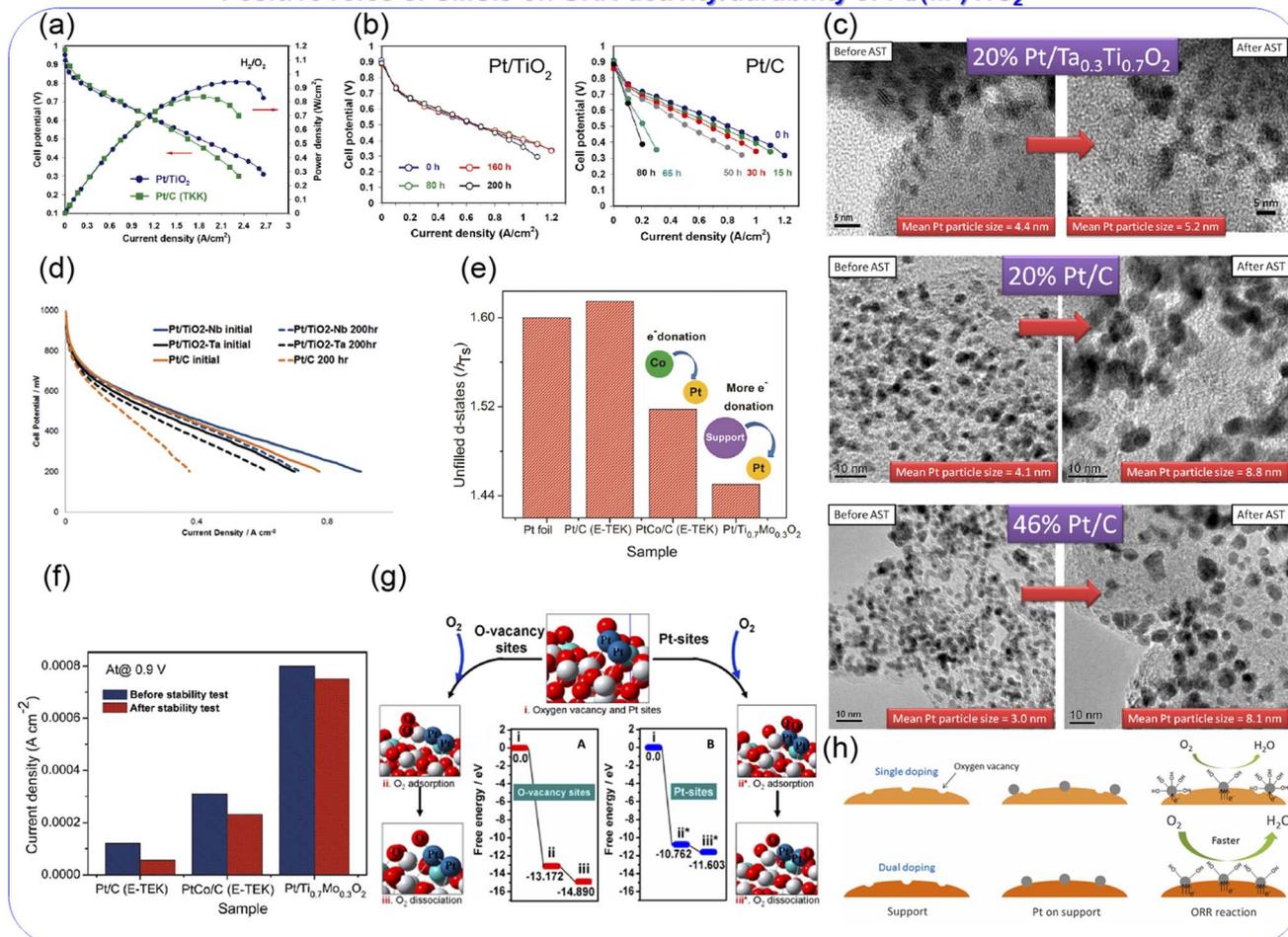
Controlling the size to the order of 10 or 100 nm, as well as maintaining phase purity in the crystal structure, is necessary for the use of Ti$_4$O$_7$ as a support for PEFC cathodes. The catalyst mass, which is vital for its use in vehicles, should increase by changing the support from carbon black to Ti$_4$O$_7$ at a lower Pt mass fraction in Pt/Ti$_4$O$_7$ than Pt/C when the Pt loading is kept constant. The Pt mass fraction of a standard Pt/C (TEC10E50E; Tanaka Kikinzoku Kogyo) is 46–48% w/w and that in Pt/Ti$_4$O$_7$ optimized in ref. 36 was 20% w/w. Li *et al.* succeeded in increasing the Pt mass fraction optimized for use in PEFC anodes to 40% w/w with a smaller Pt particle size (3–4 nm) and narrower size distribution than our work[36] by using an ethanol

reduction method to deposit Pt nanoparticles on Ti$_4$O$_7$ with a size of 200–300 nm.[37] The enlargement of the surface area of Ti$_4$O$_7$ by decreasing its size produces a larger number of sites on which to deposit Pt nanoparticles. A Ti$_4$O$_7$ particle size of approximately 100 nm will be sufficient to produce 46% w/w Pt/Ti$_4$O$_7$, similar to the standard Pt/C. The density of Ti$_4$O$_7$, 4.32 g cm^{-3},[63] is approximately twice as large as that of carbon, 2.2 g cm^{-3}, and thus the volume of Pt/Ti$_4$O$_7$ is lower than that of Pt/C at an identical platinum mass fraction. Therefore, catalyst layer thickness can be reduced by replacing Pt/C with Pt/Ti$_4$O$_7$ at a constant platinum mass fraction and constant platinum loading. Indeed, the thickness of the 40% w/w Pt/Ti$_4$O$_7$ catalyst layer was much lower than that of the 47% w/w Pt/C catalyst layer.[37]

Another challenge for the widespread use of Ti$_4$O$_7$ is its scalability, and the batch size has not been described in many publications. We have recently reported that simple substitutional vanadium doping increased the batch size of Ti$_4$O$_7$ synthesized *via* a conventional high-temperature solid-state reaction route to 2 g. Vanadium cations, V^{4+} and V^{3+}, were dissolved into a Ti$_4$O$_7$ lattice without segregating to form vanadium oxides up to (Ti$_{0.91}$V$_{0.09}$)$_4$O$_7$.[64] A combination of vanadium doping and the carbothermal reduction reaction may further increase the batch size.

Esfahani *et al.* utilized Mo-doped Ti$_3$O$_5$ (ref. 65) and Mo, Si-codoped Ti$_3$O$_5$ (ref. 54 and 66) as supports for Pt particles. Although Ti$_3$O$_5$ is less conductive in bulk than Ti$_4$O$_7$,[33] their conductivity was enhanced by doping with Mo and Si.[66] The term "doping" has been most frequently used to describe the introduction of foreign elements into metal oxides, nitrides, *etc.*, although the precise meaning differs by author. When V^{4+} substituted for Ti^{4+} in Ti$_4$O$_7$, the peaks in the X-ray diffraction (XRD) patterns shifted to higher angles with increasing vanadium doping level as the ionic radius of V^{4+} is lower than that of Ti^{4+}.[64] In this case, the term "doping" is taken to mean substitution. In other cases, foreign elements occupy an interstitial position or form other phases. The term "doping" has even been used without evaluating the crystal structure in some papers. In

This journal is © The Royal Society of Chemistry 2024

J. Mater. Chem. A, 2024, **12**, 18636–18673 | **18643**

Positive roles of SMSIs on ORR activity/durability of Pt/(M-)TiO₂

Negative roles of SMSIs on ORR activity/durability of Pt/(M-)TiO₂
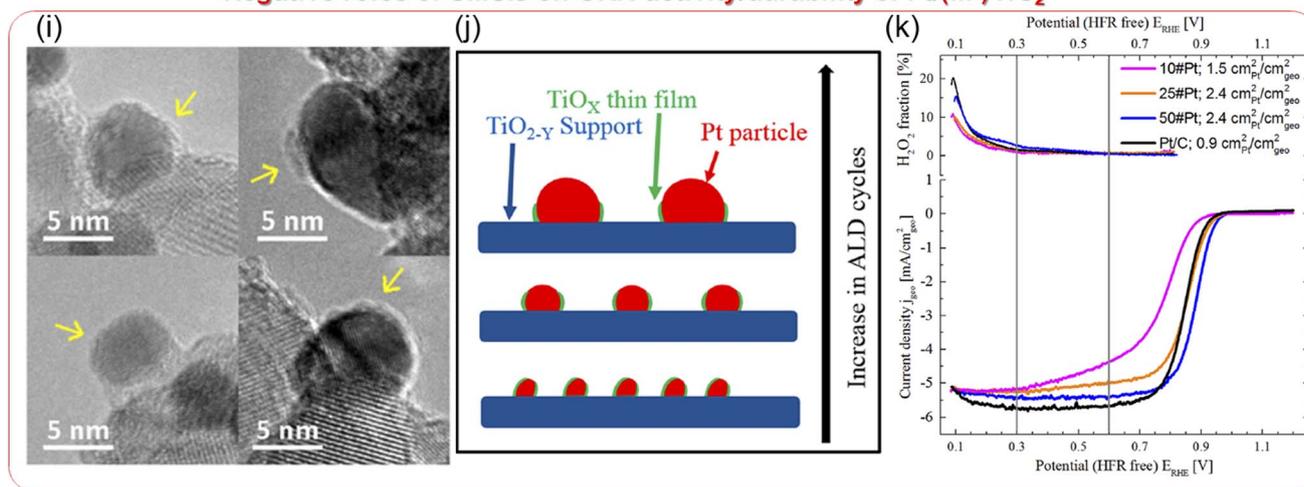
Fig. 5 (a) Cell potential *versus* current density curves of MEAs fabricated using Pt/TiO₂ and Pt/C in cathodes and Pt/C in anodes at 348 K. The Pt loading was set at 0.5 and 0.4 mg$_{Pt}$ cm^{-2} in the anode and cathode, respectively. The anode and cathode gases were fully humidified H₂ and O₂, respectively. (b) Cell potential *versus* current density curves of MEAs fabricated using Pt/TiO₂ and Pt/C in cathodes and Pt/C in anodes at 353 K before and after cell potential holding at 1.2 V for various durations. The anode and cathode gases were H₂ and O₂, respectively, with 50% RH. During potential holding, the cell was supplied with fully humidified H₂ and N₂ at the anode and cathode, respectively. The Pt loading was set at 0.5 and 0.4 mg$_{Pt}$ cm^{-2} in the anodes and cathodes, respectively. Reproduced with permission.[67] Copyright 2009, American Chemical Society. (c) Transmission electron microscopy (TEM) images of 20% w/w Pt/Ta₀.₃Ti₀.₇O₂, 20% w/w Pt/C, and commercial 46% w/w Pt/C particles before and after 10 000 voltage cycles between 1.0 and 1.5 V at 0.5 V s^{-1}, hereafter denoted as FCCJ startup/shutdown cycles in a single cell. Reproduced with permission.[56] Copyright 2014, American Chemical Society. (d) Cell potential *versus* current density curves of MEAs fabricated using a phosphoric-acid-doped polybenzimidazole (PBI) membrane, 20% w/w Pt/TiO₂-Nb, and 20% w/w Pt/TiO₂-Ta in the cathodes and 20% w/w Pt/

18644 | *J. Mater. Chem. A*, 2024, **12**, 18636–18673

This journal is © The Royal Society of Chemistry 2024

the current paper, all articles that contributed to the development of carbon-support-free catalysts are reviewed, and the term "doping" is taken to mean any of the cases described above. The Mo, Si-codoped Ti_3O_5 contains seven phases (Ti_3O_5, Ti_6O, Mo, MoO_2, Mo_9O_{26}, Si, and SiO_2), and the presence of these different phases makes it difficult to clarify the role of each element. However, the reported durability is among the highest in the reported oxide-supported catalysts, as shown in Table 1.

2.1.1.2 Titanium dioxide-supported catalysts.

Titanium dioxide, TiO_2, is the most widely studied metal oxide owing to its abundance and potential for use in a number of applications including photocatalysis, photovoltaic cells, gas sensors, and anodes in secondary batteries based on lithium, sodium, potassium, and aluminum ions. TiO_2-based materials are also the most studied non-carbon PEFC cathode catalyst supports. The main advantage of TiO_2 is its higher surface area compared with Magnèli-phase Ti_nO_{2n-1}, which is due to the lower synthesis temperature because TiO_2 does not need to be reduced at high temperatures. In contrast, the principal disadvantage of TiO_2 is its lower conductivity, as displayed in Fig. 4(k). The Popov group reported high surface-area TiO_2 supports for PEFC cathodes, including mesoporous TiO_2 with a BET surface area of 250–266 $m^2\ g^{-1}$, which was successfully synthesized via a template-assisted route using Pluronic P123 as a surfactant.[55,67] Pt nanoparticles were deposited on high surface-area mesoporous TiO_2 to yield high platinum mass fractions of 40% w/w and 60% w/w for Pt particle sizes of 4.2 nm and 5.1 nm, respectively.[55] Pt/TiO_2 exhibited a single-cell performance comparable to that of commercial Pt/C when the cell voltage exceeded 0.6 V, as shown in Fig. 5(a). At a cell voltage below 0.6 V, Pt/TiO_2 displayed even higher current density than Pt/C owing to the thinner catalyst layer, improving mass-transport properties. As the density of TiO_2 is approximately twice that of carbon, the Pt/TiO_2 catalyst layers were thinner than their Pt/C counterparts (<3 μm).[67] Pt/TiO_2 exhibited considerably higher durability against cell potential held at 1.2 V compared with Pt/C, as shown in Fig. 5(b). Although these results from the Popov group are encouraging, other researchers have extended their work to use TiO_2-carbon composites to further enhance the conductivity of TiO_2

supports. Composites of oxides and carbon materials such as carbon black[74] and carbon nanotubes (CNTs)[75] rely on the conductivity of the carbon materials, which decreases following exposure to high PEFC potentials due to carbon corrosion, as described in Section 1. A more favorable approach than using TiO_2-carbon composites is to enhance the conductivity of TiO_2 by doping with other cations or anions.

2.1.1.2.1 Cation-doped titanium dioxide-supported catalysts.

Pentavalent cations such as Nb^{5+}, Ta^{5+}, and V^{5+} are the most studied dopants for TiO_2 as a PEFC cathode catalyst support. When pentavalent cations (M^{5+}) substituted for Ti^{4+} in TiO_2, one Ti cation vacancy is created for every four M^{5+} introduced, or Ti^{4+} is reduced to Ti^{3+} for every M^{5+} introduced to compensate for the charge imbalance caused by M^{5+} substitution. This introduces shallow donor levels below the conduction band edge of TiO_2 and increases the metallic character. The doping of hexavalent cations such as Mo^{6+} and W^{6+} into TiO_2 has also been researched, and Nb-doped TiO_2 has been investigated by many groups since the late 2000s. A higher ORR activity has been reported for Nb-doped TiO_2 compared with Pt/C in half-cells employing acidic media,[76–79] as well as a higher durability of Nb-doped TiO_2 than Pt/C in single cells.[80,81] These advantages of Nb-doped TiO_2 have been attributed to SMSIs.[76,78,79,81] However, the initial single-cell performance of Nb-doped TiO_2 remains lower than that of Pt/C,[80,81] and careful optimization of some factors is therefore needed. As mentioned in Section 2.1.1.1, each titanium atom in rutile TiO_2 coordinates six oxygen atoms to form a TiO_6 octahedron. Anatase, another form of TiO_2 which is often used as a Pt-catalyst support, also consists of TiO_6 octahedra, but differs in the number of shared edges (two for rutile versus four for anatase). Therefore, the coordination number of the titanium atoms in both anatase and rutile TiO_2 is 6. The ionic radii of 6-coordinated titanium and its dopants are listed in Table 2.[82] The ionic radius of Nb^{5+} at 64 pm is close to that of Ti^{4+} (60.5 pm), and thus Nb^{5+} readily substituted for Ti^{4+} to increase the doping level. Both the anatase/rutile ratio and Nb-doping level significantly affect the conductivity and BET surface area of Nb-doped TiO_2,[83] which are critical for the single-cell performance of Pt/Nb-doped TiO_2. Most studies on Nb-doped TiO_2 have been performed using a single composition, i.e., a single Nb-doping level or sole crystal

---

C in the anodes at 423 K before and after holding the open-circuit potential for 200 h. Pt loading was set at 0.2 and 0.5 $mg_{Pt}\ cm^{-2}$ in the anodes and cathodes, respectively. Reproduced with permission.[68] Copyright 2014, Royal Society of Chemistry. (e) Unfilled d-states of Pt foil, commercial 20% w/w Pt/C, commercial 30% w/w PtCo/C, and 20% w/w $Pt/Ti_{0.7}Mo_{0.3}O_2$ measured using X-ray adsorption near-edge spectroscopy (XANES). (f) Current density of commercial 20% w/w Pt/C, commercial 30% w/w PtCo/C and 20% w/w $Pt/Ti_{0.7}Mo_{0.3}O_2$ at 0.9 V versus SHE in 0.5 mol dm^{-3} H_2SO_4 before and after 5000 potential cycles between 0 and 1.1 V at 50 mV s^{-1}. Reproduced with permission.[69] Copyright 2011, American Chemical Society. (g) Proposed models of selective oxygen adsorption and the different reaction pathways for oxygen dissociation on the Pt/d-$Ti_{0.9}Mo_{0.1}O_2$ catalyst at (A) the interface between the Pt and oxygen vacancy and (B) the supported Pt surface, where white, red, blue, and light blue spheres represent Ti, oxygen, Pt, and, Mo, respectively. Reproduced with permission.[70] Copyright 2016, American Chemical Society. (h) Schematic illustration of Pt loading on single-doped and dual-doped TiO_2 supports and the oxygen reduction reaction (ORR). Reproduced with permission.[71] Copyright 2017, Nature Publishing Group. (i) High-resolution (HR) TEM images of Pt on Pt/TiO_2 after reduction under pure H_2 at 473 K. Reproduced with permission.[72] Copyright 2017, Elsevier. (j) Schematic diagram of the correlation between TiO_x film coverage and Pt particle size. The larger the number of Pt atomic layer deposition (ALD) cycles, the larger the Pt particle size, and the smaller the TiO_x surface coverage, and vice versa. (k) Rotating ring disk electrode voltammograms of $Pt/TiO_{2-y}/C$ catalysts prepared with ALD and 5% w/w Pt/C as a reference. Roughness factors (in cm_{Pt}^2/cm_{geo}^2) of the electrodes are shown in the legend. The voltammograms were obtained in the anodic scan direction recorded at 50 mV s^{-1} and 1600 rpm in O_2 saturated 0.1 mol dm^{-3} $HClO_4$. The ring potential was held at 1.2 V versus RHE. Reproduced with permission.[73] Copyright 2020, The Electrochemical Society.

This journal is © The Royal Society of Chemistry 2024

J. Mater. Chem. A, 2024, 12, 18636–18673 | 18645

Table 2 Ionic radii of 6-coordinated cations[82]

Cation	Ionic radius (pm)	Cation	Ionic radius (pm)	Cation	Ionic radius (pm)
Ti^{4+}	60.5	V^{5+}	54	Cr^{4+}	55
Nb^{5+}	64	V^{4+}	58	Cr^{3+}	61.5
Nb^{4+}	68	Mo^{6+}	59	W^{6+}	60
Ta^{5+}	64	Mo^{5+}	61	W^{5+}	62
Ta^{4+}	68	Cr^{5+}	49	W^{4+}	66

structure (anatase or rutile). Careful optimization of these material factors mentioned in the previous sentence and catalyst layer structure such as the PFSI to catalyst ratio and the mass fraction of Pt in Pt/Nb-doped TiO_2 to control the thickness and pore structure may improve the single-cell performance of MEAs employing Pt/Nb-doped TiO_2 catalyst layers.

Kumar and Ramani introduced Ta-doped TiO_2 into PEFC cathodes in the mid-2010s.[56,84] The Ta formed solid solutions with TiO_2 and shifted peaks in the XRD patterns to lower angles, suggesting that the larger Ta^{5+} substituted for smaller Ti^{4+} in TiO_2.[84] Interestingly, the growth of the TiO_2 particle size during annealing at 1123 K for 3 h was inhibited by Ta-doping due to distortion in the crystal lattice. When the composition changed from TiO_2 to $Ta_{0.3}Ti_{0.7}O_2$, the mean particle size decreased from 84 nm to 67 nm, and thus the BET surface area increased from 9 m^2 g^{-1} to 26 m^2 g^{-1}.[84] Pt nanoparticles around 4–5 nm in size were supported on $Ta_{0.3}Ti_{0.7}O_2$ to yield 20% w/w Pt/$Ta_{0.3}Ti_{0.7}O_2$. Although the ECSA and ORR mass activity of 20% w/w Pt/$Ta_{0.3}Ti_{0.7}O_2$ are smaller than those of commercial 46% w/w Pt/C with 3 nm Pt particles in both a half-cell[84] and single cell[56] owing to the larger Pt particle size, 20% w/w Pt/$Ta_{0.3}Ti_{0.7}O_2$ exhibited much higher durability against 10 000 DOE load cycles and 10 000 FCCJ startup/shutdown cycles than 46% w/w Pt/C in a single cell. During both types of cycles, the growth of Pt particle size in 20% w/w Pt/$Ta_{0.3}Ti_{0.7}O_2$ was suppressed, as shown in Fig. 5(c), with the high durability ascribed to the SMSI between Pt nanoparticles and $Ta_{0.3}Ti_{0.7}O_2$ supports.[56] Other researchers following the work of Kumar and Ramani reported that SMSIs were responsible for the higher durability of Pt/Ta-doped TiO_2 versus commercial Pt/C.[68,85] SMSIs in Pt/Ta-doped TiO_2 and Pt/Nb-doped TiO_2 were also reported to enhance the methanol oxidation reaction at 353 K in direct methanol fuel cell (DMFC) anodes and the ORR at temperatures exceeding that of PEFCs (423 K in polybenzimidazole [PBI] membrane fuel cell cathodes, as shown in Fig. 5(d)).[68]

Vanadium, whose maximum valence is 5+, has attracted less attention than Nb^{5+} or Ta^{5+} as a dopant in TiO_2. In 2016, Kim et al. reported that SMSIs were responsible for the three-fold higher durability of Pt nanoparticles supported on spherical V-doped TiO_2 particles compared to Pt/C in a half-cell.[86] Although the half-cell tests were designed with catalyst layers comprising catalysts and carbon black to improve the conductivity, and although the compositions of the catalysts are not described, Kim et al. noted that lattice contraction by substitutional doping of the smaller V^{5+} for Ti^{4+} in TiO_2 shortened the interatomic Pt–Pt bond length to enhance ORR activity. Table 2

shows that the ionic radii of Nb^{5+} and Ta^{5+} are larger than that of Ti^{4+}, and thus the TiO_2 lattice is expanded when Nb^{5+} or Ta^{5+} substituted for Ti^{4+}. Kim et al. also reported that the ORR activity of Pt/V-doped TiO_2 exceeded that of Pt supported on TiO_2 doped with larger cations (Pt/Cr-doped TiO_2 and Pt/Nb-doped TiO_2).[86] Later, Noh et al. reported the higher activity and durability of a 6% w/w Pt/V-TiO_2 nanotube (V-TNT) compared with conventional 20% w/w Pt/C in a half-cell without adding carbon black in catalyst layers. Similar to the work of Kim et al.,[86] they also used Cr-doped and Nb-doped TNT as supports. Among the three 6% w/w Pt/M-TNTs where M = V, Cr, or Nb, Pt/V-TNT displayed the smallest Pt particle size and the highest ORR activity and durability.[87] Using single-cell tests, Bharti and Cheruvally reported higher ORR activity and durability of Pt/V-doped TiO_2 particle catalysts compared with commercial Pt/C.[88]

The Hwang group has focused on Mo-doped TiO_2 supports. By using a hydrothermal method, fine $Ti_{0.7}Mo_{0.3}O_2$ nanoparticles (8–10 nm in size) with a high BET surface area of 230 m^2 g^{-1} were successfully synthesized. The Mo ions with an average valence of 5.75 were dissolved in a single anatase TiO_2 phase. Then 3–4 nm Pt nanoparticles were anchored on $Ti_{0.7}Mo_{0.3}O_2$ using a microwave-assisted polyol method. X-ray adsorption near-edge spectroscopy (XANES) revealed that 20% w/w Pt/$Ti_{0.7}Mo_{0.3}O_2$ displayed a higher electron density around the Pt atoms, and thus a lower d-band vacancy than commercial 20% w/w Pt/C or commercial 30% w/w PtCo/C owing to SMSIs between Pt nanoparticles and $Ti_{0.7}Mo_{0.3}O_2$, as shown in Fig. 5(e). 20% w/w Pt/$Ti_{0.7}Mo_{0.3}O_2$ exhibited the highest initial ORR activity and the highest durability against 5000 potential cycles between 0 and 1.1 V versus RHE in half-cells among the three catalysts, as shown in Fig. 5(f).[69] Later, the composition was optimized after introducing oxygen vacancies by H_2 annealing to $Ti_{0.9}Mo_{0.1}O_y$. The oxygen vacancies enhanced the conductivity and ORR activity by facilitating the dissociative adsorption of O_2 molecules on the Pt surface, with the proposed ORR model by density functional theory (DFT) calculations shown in Fig. 5(g).[70] Rutile TiO_2 doped with other cations such as W and Ir and anatase TiO_2 doped with W have also been reported to enhance the ORR activity and durability of Pt catalysts in half-cells.[89–91]

2.1.1.2.2 Cation and anion codoped titanium dioxide-supported catalysts. While anions such as N^{3-} and F^- have been doped into TiO_2 photocatalysts to decrease the band gap and increase the electrical conductivity, anion-doped TiO_2 has seldom been investigated as a support material in PEFCs. The Hwang group developed Nb/Ta- and N-codoped TiO_2 particles for use as support materials in PEFC cathodes. These dopants successfully formed a solid solution with the anatase TiO_2 crystal structure, and σ at $P = 200$ MPa and the BET surface area were increased by codoping rather than single-cation doping. Interestingly, Ti K-edge XANES analyses revealed that Pt nanoparticles were selectively deposited on oxygen vacancy sites on Nb/Ta- and N-codoped TiO_2 supports compared with Nb/Ta-doped TiO_2. The Pt particles deposited on the oxygen vacancy sites were more electronegative and had fewer hydroxyl groups

18646 | *J. Mater. Chem. A*, 2024, **12**, 18636–18673

This journal is © The Royal Society of Chemistry 2024

on the surface during the ORR, enhancing the activity as illustrated in Fig. 5(h). Due to SMSIs, both Pt/codoped TiO_2 catalysts displayed higher ORR activity and durability against load cycles between 0.6 and 1.0 V at 50 mV s^{-1} than Pt/C in a half-cell.[71] Lee et al. reported N- and C-codoped TiO_2-supported Pt catalysts. Abundant oxygen vacancies and lattice disorder defects formed by the N, C-codoping enhanced the magnitude of the SMSIs to achieve high durability against 5000 FCCJ startup/shutdown cycles in a single cell.[92] The high durability of Pt/N, C-codoped TiO_2 in a half cell was reported by the Bhat group.[93] The codoping of Cu and N into TiO_2 supports has also been shown to enhance ORR activity compared with Pt/C in a single cell.[58]

2.1.1.2.3 Mixed oxide-supported catalysts. Besides the substitutional and/or interstitial doping described above, the Ramani group also reported mixed oxide supports in the 2010s. By using a simple wet chemical route and annealing at 723 K in air, a mixture of anatase TiO_2 and rutile RuO_2 (TRO) supports with a BET surface area of 33 ± 4 m^2 g^{-1} was synthesized. Although the pressure applied for the measurements was not described, the TiO_2-RuO_2 support particles displayed a high σ of 21 ± 5 S cm^{-1}, which is close to that of carbon black (Vulcan XC-72) at 31 ± 5 S cm^{-1}.[94] RuO_2 and IrO_2 have been used as OER catalysts and are known to exhibit metallic conductivities in the range of 0.01–1 times the conductivities of the parent metals. The conductivities of RuO_2 in the [100] and [001] directions at 300 K are 27.7 and 28.0 kS cm^{-1}, respectively, and the average single-crystal conductivity is reported to be 28.4 kS cm^{-1}.[95] Therefore, the high σ-value of TRO particles is reasonable. Pt particles around 4–6 nm in size were deposited on TRO, and 40% w/w Pt/TRO exhibited higher durability against the DOE load and startup/shutdown cycles in a single cell compared with commercial 50% w/w Pt/C owing to SMSIs.[14] Other important findings from this comprehensive work are that carbon corrosion during startup/shutdown resulted in more severe damage than Pt dissolution during load cycles. In addition, CO_2 emissions were observed from the Pt/TRO cathode exit of a single cell. Although the volume of CO_2 emissions from the Pt/TRO cathode was one order of magnitude lower than that of Pt/C, the carbon microporous layer of GDLs was oxidized,[14] which is consistent with the results of Ioroi et al.,[35] suggesting the need to develop carbon-free GDLs. Similarly, Pătru et al. reported that Pt/IrO_2-TiO_2 exhibited higher durability against load cycles and startup/shutdown cycles in single cells compared with commercial 47% w/w Pt/C due to SMSIs.[57] The advantage of both mixed oxide supports is a high conductivity, although a disadvantage is the scarcity of RuO_2 and IrO_2. The use of these mixed oxide supports inevitably causes an increase in PGM loading.

All of the above-cited studies on TiO_2-based supports emphasize the merits of SMSIs for enhancing ORR activity and/or durability in half-cells and single cells. However, contrasting results have been reported since the late 2010s. One disadvantage of SMSIs is the formation of reduced thin titanium oxide (TiO_{2-x}) layers on Pt particles[96] that suppress ORR activity. The Hwang group reported that simple annealing of Pt/TiO_2 at a low temperature (473 K) induced SMSIs between the Pt

nanoparticles and commercial TiO_2 particles (P25; a standard photocatalyst with 80% anatase and 20% rutile; Degussa Co.). The Pt particles on TiO_2 were covered by thin TiO_{2-x} layers, as shown by the arrows in Fig. 5(i). Electrochemical characterization in a half-cell revealed that the thin TiO_{2-x} layers formed during low-temperature annealing decreased the ORR activity of Pt/TiO_2, while the layers were removed by hydrofluoric acid treatment to boost the ORR activity beyond that of the original Pt/TiO_2. Similar results were also observed from Pt/Nb-doped TiO_2. The thin TiO_{2-x} layers suppressed ORR activity, whereas protons could pass through the layers from CVs.[72] Banham et al. suggested Nb and/or Ti dissolution from Nb-doped anatase TiO_2 supports and their redeposition on Pt nanoparticles. The ORR activity of Pt/Nb-doped TiO_2 decreased significantly during potential cycling between 1.0 and 1.4 V versus RHE in a half-cell employing 0.1 mol dm^{-3} $HClO_4$ electrolyte, although its HOR activity did not change. The HOR activity of Pt/Nb-doped TiO_2 was also stable after holding the anode voltage at 1.45 V versus the cathode supplied with H_2 (i.e., the RHE in a single cell).[97] Eckardt et al. reported that Pt/TiO_2 and Pt/TiO_2-CNT composite catalysts degraded faster than Pt/C during startup/shutdown ADTs in a half-cell and suggested that this was due to the thin TiO_{2-x} layers.[98] Stühmeier et al. recently systematically investigated the transport properties of thin TiO_{2-x} layers. The thin TiO_{2-x} layers on Pt particles reduced the ORR, OER, and CO oxidation activity of Pt catalysts, although they did not affect either the HOR activity or the formation of hydrogen underpotential deposition. This indicates that unlike protons and hydrogen, oxygen and oxygenated species could not pass through the layers, making Pt/TiO_2 a highly selective HOR catalyst.[73,99] The researchers deposited Pt nanoparticles on a reduced TiO_{2-y} film synthesized at 973 K for 2 h under 4% v/v H_2/Ar via atomic layer deposition (ALD) and controlled the size of the Pt particles by changing the number of ALD cycles. A schematic diagram of the correlation between the layer coverage and Pt particle size obtained from the electrochemical measurements and transmission electron microscopy (TEM) images is shown in Fig. 5(j). Pt particle size increased and the Pt surface area decreased with increasing number of ALD cycles, while ORR activity increased significantly due to the increase in the exposed Pt surface area, as shown in Fig. 5(k). Hornberger et al. reported that a thin oxide layer gradually grew on the Pt particles during potential cycles between 0.6 and 0.95 V versus RHE at 0.1 V s^{-1} in 0.1 mol dm^{-3} $HClO_4$. The growth of the thin layer due to SMSIs decreased the ECSA and ORR activity of Pt/TRO.[100] The controversial effect of SMSIs on the ORR activity and durability of Pt/(M-)TiO_2 catalysts needs to be further investigated. In many reports, SMSIs between Pt nanoparticles and TiO_2-based supports produce higher ORR activity and durability than conventional Pt/C, although there are exceptions that display lower ORR activity and durability owing to the presence of thin TiO_{2-x} layers on Pt particles, as mentioned above. One of the key factors is Pt particle size, as addressed by Stühmeier et al.[73] In previous studies on Pt/TiO_2 or Pt/Ti_4O_7 in which high ORR activity and durability are reported, the Pt particle sizes are larger (mostly above 4 nm) than those of commercial Pt/C. The surface coverage of the thin TiO_{2-x} layers

This journal is © The Royal Society of Chemistry 2024

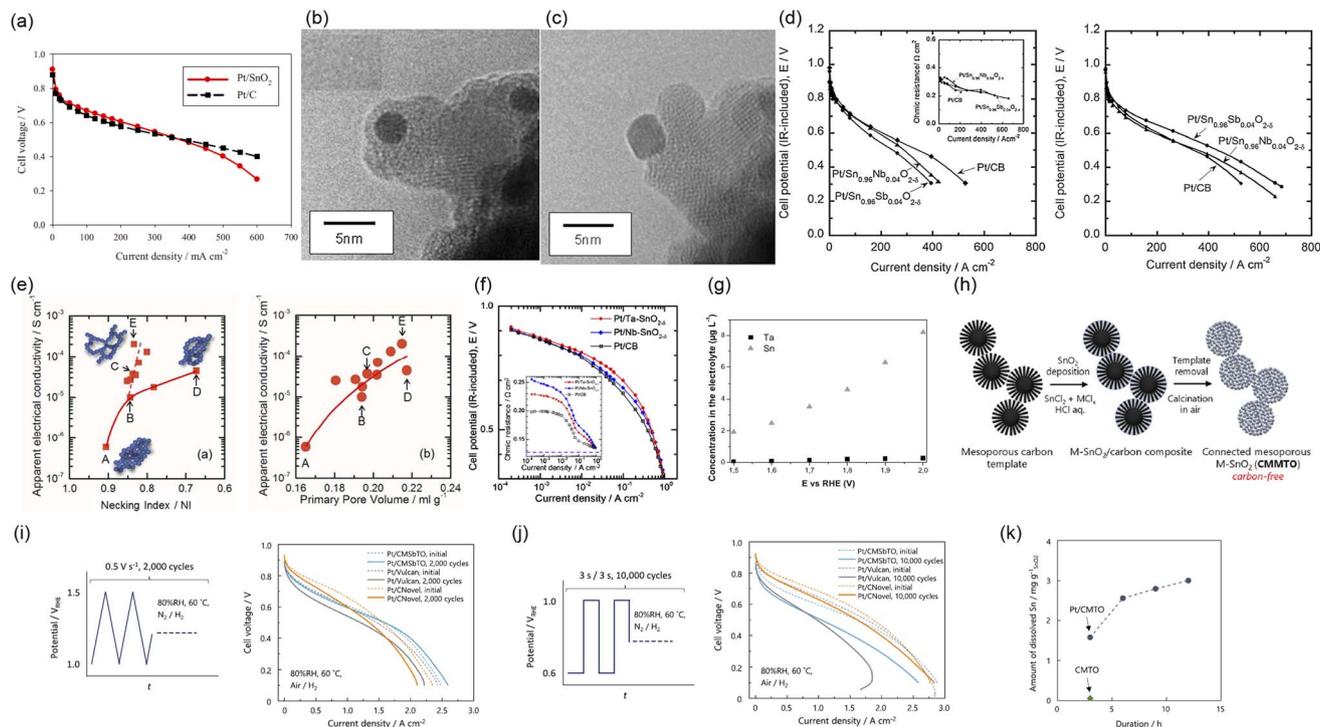J. Mater. Chem. A, 2024, 12, 18636–18673 | 18647

on the Pt particles might be low when the particle size is large, as illustrated in Fig. 5(j). This illustration is a hypothetical model, and discussions around clear high-resolution (HR)-TEM images are needed in future studies.

2.1.1.3 Tin dioxide-supported catalysts. Owing to its abundance and high stability in PEFC cathodes, SnO_2 is one of the most studied supports in this field. The Sasaki group has been developing SnO_2 supports since 2009. SnO_2 particles with a size of the order of several tens of nanometers and a BET surface area of approximately 20 m^2 g^{-1} were synthesized *via* a coprecipitation route. Compared with previous studies on Pt/ titanium suboxide and Pt/titanium oxide-based catalysts, smaller Pt nanoparticles with a diameter of 3 nm were successfully deposited on SnO_2 at a Pt mass fraction of 20% w/ w. The 20% w/w Pt/SnO_2 maintained a higher ECSA than 20% w/ w Pt/C synthesized by the authors after 10 000 potential cycles between 0.6 and 0.9 or 1.3 V *versus* RHE at 0.1 V s^{-1} in 0.1 mol dm^{-3} $HClO_4$. In addition, the single-cell performance of 20% w/ w Pt/SnO_2 was comparable to that of 20% w/w Pt/C, as shown in Fig. 6(a). Similar to reports on Pt/TiO_2 from the Popov group,[67] the Pt/SnO_2 catalyst layer was thinner than its Pt/C counterpart, and displayed lower mass-transport resistance.[101] Later, the Sasaki group doped Nb^{5+} and Sb^{5+} into SnO_2 to enhance conductivity, which was maximized at a composition of $Sn_{0.98}Nb_{0.02}O_2$. The agglomeration of SnO_2 particles was suppressed by Nb-doping to increase the BET surface to around 50 m^2 g^{-1}, and the optimized 20% w/w Pt/$Sn_{0.98}Nb_{0.02}O_2$ displayed a larger ECSA than 20% w/w Pt/C after 10 000 rectangular wave potential cycles between 0.9 and 1.3 V *versus* RHE (held for 30 s at each potential) in 0.1 mol dm^{-3} $HClO_4$. Inductively coupled plasma (ICP) atomic emission spectroscopy analyses on the 0.1 mol dm^{-3} $HClO_4$ electrolyte solution after the durability tests indicate that the amount of Sn and Nb dissolved from 20% w/w Pt/$Sn_{0.98}Nb_{0.02}O_2$ was negligible, while nearly 60% of the Pt was dissolved. The authors concluded that the fraction of dissolved Pt increased with the ECSA, regardless of the support material type.[107] To enhance the conductivity of catalyst layers utilizing optimized $Sn_{0.98}Nb_{0.02}O_2$, which is two orders of magnitude lower than that of carbon black, they then prepared composite supports of vapor-grown carbon fiber (VGCF) and $Sn_{0.98}Nb_{0.02}O_2$. Various platinum alloy (PtCo, Pt_3Co, Pt_4Co, and Pt_3Ni) nanoparticles were then supported on the composite supports. The optimized Pt_3Co/$Sn_{0.98}Nb_{0.02}O_2$/VGCF catalyst survived after 400 000 FCCJ load cycles and 60 000 FCCJ startup/ shutdown cycles in a single cell. However, the decreases in cell performance and increases in catalyst particle size during these two ADTs were not negligible.[59] Kakinuma *et al.* have devoted significant effort to improving SnO_2 conductivity and the cell performance of SnO_2-based catalyst layers. By using a flame combustion route, nano-sized M-doped SnO_2 (M = Sb, Nb, Ta) particles with a unique fused aggregate structure were successfully synthesized as supports for Pt or Pt-alloy catalysts. The structure of these materials is similar to that of conventional carbon black used in PEFCs,[108] and the pore structure strongly affects their conductivity. The diameter of the Pt particle was successfully controlled to 3.0 nm with a nearly monodispersed diameter, as shown in Fig. 6(b). Energy

dispersive X-ray spectroscopy (EDS) analyses revealed that the Pt surface was encapsulated with an amorphous $Sn_{0.96}Sb_{0.04}O_{2-\delta}$ layer with several nanometers in thickness, owing to SMSIs. This is similar to a number of previous reports on TiO_2-based supports. The layer was successfully removed by annealing Pt/ $Sn_{0.96}Sb_{0.04}O_{2-\delta}$ at 573 K under 1% v/v H_2/N_2, as shown in Fig. 6(c). The resulting surface layer-free 19.8% w/w Pt/$Sn_{0.96}$-$Sb_{0.04}O_{2-\delta}$ displayed high durability against rectangular potential cycles between 0.9 and 1.3 V *versus* RHE (held for 30 s at each potential) in 0.1 mol dm^{-3} $HClO_4$. Interestingly, the ECSA increased from 50 to 60.2 m^2 g^{-1} when the cycle number increased from 0 to 1000, and then decreased slightly to 58 m^2 g^{-1} after 5000 cycles, which still exceeds that before cycling. The SMSIs between the Pt nanoparticles and $Sn_{0.96}Sb_{0.04}O_{2-\delta}$ supports suppressed Pt migration or dissolution to maintain the monodisperse distribution of Pt nanoparticle size (mean Pt particle size after the 5000 potential cycles was 3.2 nm, which is almost the same as that before cycling).[102] Later, the single-cell performance was optimized using careful CV measurements and support solubility measurements with ICP. When the potential was lower than 0.4 V, a small amount of Sn was dissolved and deposited on the Pt nanoparticle surface to inhibit the ORR process. Preconditioning before measurement significantly affected the single-cell performance, as shown in Fig. 6(d). When the cathode 12.3% w/w Pt/$Sn_{0.96}Sb_{0.04}O_{2-\delta}$ or 10.0% w/w Pt/$Sn_{0.96}Nb_{0.04}O_{2-\delta}$ catalyst layers were preconditioned at 0.1 V for 24 h before measurement, their current densities were lower than that of the standard 47.9% w/w Pt/CB at cell voltages lower than 0.7 V. However, Pt/$Sn_{0.96}Sb_{0.04}O_{2-\delta}$ and Pt/$Sn_{0.96}Nb_{0.04}O_{2-\delta}$ catalyst layers outperformed their Pt/CB counterpart when the cathode potential was maintained above 0.4 V, as the dissolution/deposition of Sn species from the support was suppressed.[103] The aggregate structure of the supports was later controlled to enhance conductivity, as shown in Fig. 6(e). Kakinuma *et al.* evaluated the level of necking between $Sn_{0.96}Nb_{0.04}O_{2-\delta}$ particles using the "necking index" (NI), defined as the ratio of the BET surface area to the surface area of the sphere, calculated by assuming that the diameter is equal to the mean crystallite size as determined from the XRD pattern. Isolated spheres are expected when NI = 1, and developed necking structures are expected as the NI decreases below 1. Apparent conductivity, defined as σ at P = 19 MPa, increased with decreasing NI for two different types of dependence: the route from B to D and B to E *via* C. The authors attributed the source of the two different routes to the pore structure. The apparent conductivity increased consistently with the volume of the primary pores, which are formed between the aggregated $Sn_{0.96}Nb_{0.04}O_{2-\delta}$ particles and defined as pores below 30 nm in diameter.[104] These findings by Kakinuma *et al.* are truly original and all their studies are among the most meticulous in related literature.

The controlled fused aggregate structure was then applied to Ta-doped SnO_2 supports. Ta-SnO_2 displayed apparent conductivity approximately 40 times higher than that of Nb-SnO_2 due to the higher carrier concentration, with a similar aggregate structure. In addition, the ORR activity of Pt/Ta-doped SnO_2 exceeded that of Pt/Nb-SnO_2 and commercial Pt/C in a single

18648 | *J. Mater. Chem. A*, 2024, **12**, 18636–18673

This journal is © The Royal Society of Chemistry 2024

Fig. 6 (a) Cell voltage *versus* current density curves of MEAs fabricated using 20% w/w Pt/SnO$_2$ and 20% w/w Pt/C in the cathode at 353 K. The anode and cathode gases were almost fully humidified H$_2$ and air, respectively. Commercial 46% w/w Pt/C catalysts were used in the anode. The cathode and anode platinum loadings were set at 0.6 and 0.4 mg$_{Pt}$ cm^{-2}, respectively. Reproduced with permission.[101] Copyright 2009, The Electrochemical Society. *In situ* environmental TEM images of Pt/Sn$_{0.96}$Sb$_{0.04}$O$_{2-\delta}$ (b) before and (c) after annealing at 573 K under 1% v/v H$_2$/N$_2$. Reproduced with permission.[102] Copyright 2011, Elsevier. (d) Cell potential *versus* current density curves of MEAs fabricated using three different catalysts (10% w/w Pt/Sn$_{0.96}$Nb$_{0.04}$O$_{2-\delta}$, 12.3% w/w Pt/Sn$_{0.96}$Sb$_{0.04}$O$_{2-\delta}$, and commercial 47.9% w/w Pt/CB) in the cathode at 353 K. Commercial 47.9% w/w Pt/CB catalysts were used in the anode. The cathode and anode platinum loadings were set at 0.2 and 0.5 mg$_{Pt}$ cm^{-2}, respectively. The anode and cathode gases were H$_2$ and air, respectively, at 53% RH. Each catalyst layer was (left) preconditioned at 0.1 V for 24 h and (right) maintained above 0.4 V. Reproduced with permission.[103] Copyright 2013, Elsevier. (e) (left) Apparent electrical conductivity *versus* necking index (NI) curves and (right) apparent electrical conductivity *versus* primary pore volume curve of Sn$_{0.96}$Nb$_{0.04}$O$_{2-\delta}$. Reproduced with permission.[104] Copyright 2014, Royal Society of Chemistry. (f) Cell potential *versus* current density curves of MEAs fabricated using three different cathode catalysts (15.8% w/w Pt/Ta-SnO$_{2-\delta}$, 15.3% w/w Pt/Nb-SnO$_{2-\delta}$, and commercial 46–48% w/w Pt/CB) at 353 K. The inset shows cell resistance *versus* current density curves. Commercial Pt/CB catalysts were used in the anode. The cathode and anode platinum loadings were set at 0.06 ± 0.002 and 0.5 ± 0.05 mg$_{Pt}$ cm^{-2}, respectively. The anode and cathode gases were H$_2$ and air, respectively at 53% RH. Reproduced with permission.[105] Copyright 2015, Elsevier. (g) Sn and Ta concentrations dissolved from Ta-doped SnO$_2$ in 0.5 mol dm^{-3} H$_2$SO$_4$ electrolyte solution *versus* potential curves at 353 K. The potential was held for 4 h. Reproduced with permission.[51] Copyright 2020, American Chemical Society. (h) Synthesis scheme of connected mesoporous M-doped tin oxide (CMMTO). (i) (left) Potential *versus* time curve of the used FCCJ startup/shutdown cycles and (right) cell voltage *versus* current density curves of MEAs fabricated using three different cathode catalysts (20% w/w Pt/CMSbTO, commercial 30% w/w Pt/Vulcan, and 30% w/w Pt/C$_{novel}$) before (dashed lines) and after (solid lines) 2000 FCCJ startup/shutdown cycles at 333 K. Commercial Pt/C catalysts were used in the anode. The cathode and anode platinum loadings were set at 0.1 and 0.05 mg$_{Pt}$ cm^{-2}, respectively. The anode and cathode gases were H$_2$ and air, respectively, at 80% RH. (j) (left) Potential *versus* time curve of the used FCCJ load cycles and (right) cell voltage *versus* current density curves of MEAs fabricated using the three different cathode catalysts used in (i) before (dashed lines) and after (solid lines) 10 000 FCCJ load cycles at 333 K. Other conditions were identical to those used in (i). (k) Cumulative amount of dissolved Sn from the connected mesoporous tin oxide (CMTO) and Pt/CMTO *versus* the dissolution test duration in 1 M HClO$_4$ at 333 K with H$_2$ bubbling. Reproduced with permission.[106] Copyright 2024, American Chemical Society.

cell, as shown in Fig. 6(f).[105] To the best of the author's knowledge, the cathode Pt loading in Fig. 6(f) (0.06 ± 0.002 mg$_{Pt}$ cm^{-2}) is the lowest among the MEAs utilizing Pt/non-carbon supported catalysts reported to date. The development of Nb/Ta-doped SnO$_2$-supported Pt,[60,109,110] PtCo,[111] and PtCoSn[112] catalysts continues to the present day, with other groups also focusing on such Sb/Nb/Ta-doped SnO$_2$ supports. For example, Cavaliere *et al.* developed Sb/Nb/Ta-doped SnO$_2$ nanofiber supports *via* an electrospinning route.[51,53,113–115] Careful

optimization of the doping level was performed on these supports, and all Pt/M-doped SnO$_2$ catalysts displayed higher durability than Pt/C in half-cells[51,53,114] and in single cells[114] owing to SMSIs. The researchers concluded that Ta-doped SnO$_2$ is the best support for Pt nanoparticles among the three candidates, simultaneously showing higher conductivity than Nb-doped SnO$_2$ and higher stability than Sb-doped SnO$_2$.[51] Nonetheless, Ta and Sn were found to dissolve from the optimal Ta-doped SnO$_2$ in 0.5 mol dm^{-3} H$_2$SO$_4$ solution, with the

quantity of both elements increasing with potential, as shown in Fig. 6(g).[51] Although little of the element was dissolved (less than 0.1% w/w) and the potential holding time was relatively long (4 h), these findings suggest that M-doped SnO$_2$ is more stable in PEFC cathodes than the anode counterparts at potentials exceeding 1.5 V (where PEFC anodes face H$_2$ starvation) (Fig. 6(g)). This is particularly true when combined with the results from Kakinuma et al., in which Sn dissolved at potentials lower than 0.4 V.[103] Many other groups have followed these pioneering studies utilizing Sb/Nb/Ta-doped SnO$_2$ supports.[61,116–119]

Several new strategies have been reported recently. In 2024, Inaba et al. developed unique connected mesoporous M-doped SnO$_2$ supports using a mesoporous carbon template, and the scheme is shown in Fig. 6(h).[106] Mesoporous carbon supports enhance PEFC performance by reducing the amount of Pt poisoned by the sulfonic group of PFSI and reduce oxygen-transport resistance through the PFSI,[120] and are used in FCVs.[121] A carbon-free mesoporous SnO$_2$ support with a single mesopore size has also been developed,[118,122] although the effect of pore size on performance has not been clarified. The impact of the pore size was negligible in a half-cell employing liquid electrolyte but significant in a single cell, owing to the difference in mass-transport properties. Inaba et al. optimized parameters such as the pore size of connected mesoporous Sb-doped SnO$_2$ (CMSbTO) at 7.3 nm for single-cell performance and Sb-doping at around 6 at% for conductivity.[106] From the four tested dopants (Sb, Nb, Ta, and W), they selected Sb as its conductivity was the highest. The optimized Pt/CMSbTO exhibited superior single-cell performance compared with Pt supported on nonporous solid-core Sb-doped SnO$_2$, solid-core carbon (Vulcan) and mesoporous carbon (C$_{novel}$) supports under dry conditions (i.e., when H$_2$ and air gases with 30% RH were supplied to the anode and cathode), owing to the hydrophilic surface of CMSbTO. When these gases were supplied with 80% RH, Pt/C$_{novel}$ exhibited the best cell performance, although this initial high performance deteriorated significantly over 2000 FCCJ startup/shutdown cycles in contrast to the minimal changes in Pt/CMSbTO performance observed, as shown in Fig. 6(i). This indicates the superior durability of Pt/CMSbTO. Interestingly, the higher durability of Pt/CMSbTO over Pt/C$_{novel}$ or Pt/Vulcan was not observed over 10 000 FCCJ load cycles, as shown in Fig. 6(j). One reason for this is the stability of Pt/CMSbTO at low potentials, where Sn ions leach from the CMSbTO support and significantly increase in quantity due to the presence of Pt, as shown in Fig. 6(k).[106] Kakinuma et al.[103] and Jalalpoor et al.[118] reported the dissolution of Sn and Sb ions from Sb-doped SnO$_2$ at low potential, respectively. The selection of other dopants[103,105] may affect the amount of Sn or dopant dissolution. The formation of an SnS$_2$/SnO$_2$ heterojunction[123] and oxygen vacancies in SnO$_2$ (ref. 124) was recently reported to enhance the ORR activity in a half-cell and durability against FCCJ startup/shutdown cycles in a single cell, respectively. A combination of the three new strategies mentioned in this paragraph may drive the practical application of SnO$_2$-based supports in PEFC cathodes.

2.1.1.4 Other oxide (WO$_3$, In$_2$O$_3$, ZrO$_2$, Ta$_2$O$_5$, SiO$_2$, and CeO$_2$)-supported catalysts. Compared with Ti- and Sn-based oxides, less attention has been paid to other oxides due to issues around their natural abundance, cost, stability, and conductivity. For example, from the studies on WO$_3$ supports,[125–129] the higher stability of Pt/WO$_3$ compared with Pt/C has been confirmed in a half-cell employing 0.5 mol dm^{-3} H$_2$SO$_4$,[127] while the dissolution of W species from Pt/WO$_3$ in 0.05 mol dm^{-3} H$_2$SO$_4$ has also been reported.[125] Raghuveer and Viswanathan replaced W^{6+} in WO$_3$ with Ti^{4+} to improve the stability of WO$_3$. However, stability was enhanced only at a low Ti^{4+} substitution level, and Ti^{4+} was not stable in the WO$_3$ framework at a high substitution level.[126] Liu et al. investigated the source of the degradation of Pt/WO$_3$ in a half-cell and reported that it was tied directly to the formation of water-soluble hydrogen tungsten bronze (H$_x$WO$_3$) on the support surface, which facilitated the detachment of Pt nanoparticles.[128] The properties of H$_x$WO$_3$ reported by Liu et al.[128] are unsuitable for use as a support for Pt nanoparticles. However, H$_x$WO$_3$ was later used in PEFC anodes to diminish the reverse currents shown in Fig. 1 and thus keep the cathode potential below a theoretical potential during the startup/shutdown, as described in Section 2.2. In contrast, Kumar et al. reported highly stable interconnected Pt nanoparticles supported on WO$_3$ nanorods used in the anode and cathode of a single cell. The cell containing a 20% w/w Pt/WO$_3$ catalyst remained almost constant after holding the cell voltage at 0.40 V for 6 h. The higher durability of Pt/WO$_3$ against startup/shutdown cycles in a half-cell compared with commercial Pt/C was also reported. Furthermore, the ECSA of Pt/WO$_3$ in the MEA was 3.4 times larger than that of commercial Pt/C at a Pt loading of 0.5 mg$_{Pt}$ cm^{-2}.[129] These contrasting durability results from different groups question the potential of Pt/WO$_3$ in PEFCs. It is key to investigate the effects of WO$_3$ morphology, crystallinity, exposed Pt facet, Pt particle size, and Pt loading on the durability of Pt/WO$_3$ in order to clarify the source of the controversial results reported to date.

Indium tin oxide (ITO), doped In$_2$O$_3$ formed by substituting In^{3+} with Sn^{4+}, is a well-known and commercially available transparent conducting oxide.[130] Chhina et al. reported a Pt/ITO catalyst for use in PEFC cathodes. Pt/ITO displayed higher durability than Pt/C in a half-cell, although the shape of the CVs during 100 potential cycles between 0.6 and 1.8 V versus SHE was not stable.[131] Later, Liu and Mustain developed highly durable Pt/ITO catalysts. Their 22% w/w Pt/ITO displayed negligible changes in rotating disk electrode (RDE) voltammograms and CVs during 1000 potential cycles between 0.0 and 1.4 V versus RHE in 0.1 mol dm^{-3} HClO$_4$. However, TEM analyses revealed several small pores formed on the ITO surface during the potential cycles due to the corrosion and dissolution of the surface Sn. Furthermore, the valence of the surviving Sn surface decreased significantly (the Sn^{4+} content decreased from 91% to 28% and the Sn^{2+} content increased from 9% to 72% during the potential cycles). Although these changes did not affect the ECSA or ORR activity in a half-cell employing acidic electrolyte solution,[132] they may significantly decrease the single-cell performance, as leached cations can decrease the

18650 | J. Mater. Chem. A, 2024, 12, 18636–18673

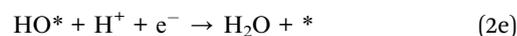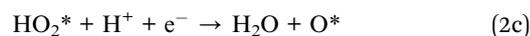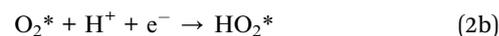This journal is © The Royal Society of Chemistry 2024

proton conductivity of the PFSI *via* ion exchange and/or catalyst poisoning. The Strasser group investigated the degradation pathways of Pt/ITO during load cycles and startup/shutdown cycles using an *in situ* scanning flow cell coupled with ICP mass spectroscopy and *in situ* X-ray techniques. Pt, Sn, and In metals dissolved on first contact between the catalyst layer and 0.1 mol dm^{-3} HClO$_4$ electrolyte under open-circuit potential conditions. Sn and In also dissolved consistently during activation cycles between 0.05 and 1.0 V *versus* RHE and load cycles between 0.6 and 0.95 V *versus* RHE at 0.1 V s^{-1}. The Sn dissolution was greater than the In dissolution in both the load cycles and FCCJ startup/shutdown cycles. Although SMSIs between Pt nanoparticles and ITO suppressed Pt dissolution compared with Pt/C, Pt surface modification due to In and accumulation of Sn was proposed as the source of activity loss during the load cycles.[133] Recently, Cheng *et al.* developed a Pt–In alloy nanocluster catalyst supported on In$_2$O$_3$ (Pt–In/In$_2$O$_3$) using a hydrothermal route. The Pt–In alloy and a single Pt metal nanocluster were synthesized on In$_2$O$_3$ by controlling the atmosphere during hydrothermal synthesis to H$_2$ and N$_2$, respectively. A number of Pt–In nanoclusters with an average diameter of 3.4 nm connected with each other on the In$_2$O$_3$ nanoparticles to give a high σ of 15.4 S cm^{-1} at $P = 20$ MPa for 42% w/w Pt–In/In$_2$O$_3$ nanoparticles. This is almost the same as that of commercial 46% w/w Pt/C (22.0 S cm^{-1}) and is three orders of magnitude higher than that of In$_2$O$_3$ supports (1.02 × 10^{-2} S cm^{-1}). Although a small amount of In dissolution from Pt–In nanoclusters was suggested by post-TEM and XRD analyses, 42% w/w Pt–In/In$_2$O$_3$ exhibited little degradation during load cycles between 0.6 and 1.0 V *versus* RHE at 0.1 V s^{-1} or during startup/shutdown cycles between 1.0 and 1.6 V at 0.1 V s^{-1} in 0.1 mol dm^{-3} HClO$_4$ solution. This was superior to commercial 46% w/w Pt/C due to the alloying effect and SMSIs.[134]

Previous studies from Lv *et al.*[31] and Sasaki *et al.*[26] (Fig. 3) suggest that ZrO$_2$, Ta$_2$O$_5$, Nb$_2$O$_5$, and SiO$_2$ are likely to be highly stable in PEFC cathodes, although they are all white in color and insulating, which is an unfavourable characteristic for a support material in PEFCs. Therefore, carbon materials have been used to achieve conductivity for these oxide-based catalyst layers.[135–140] The Ota group reported a carbon-free sulfonated ZrO$_2$-supported Pt (Pt/S-ZrO$_2$) catalyst with unique behavior in PEFC cathodes. Commercially available S-ZrO$_2$ is ZrO$_2$ modified by sulfonation to offer high proton conductivity. The researchers synthesized 53% w/w Pt/S-ZrO$_2$ catalysts from commercial S-ZrO$_2$ powder and H$_2$PtCl$_6$·6H$_2$O solution using an ultrasonic spray pyrolysis route. The single-cell performance of the 53% w/w Pt/S-ZrO$_2$ cathode exceeded that of its commercial 46% w/w Pt/C counterpart in the absence of PFSI in the catalyst layers, although the trend was reversed in the presence of PFSI indicating that S-ZrO$_2$ provides proton conductivity in the catalyst layer, allowing S-ZrO$_2$ to decrease the PFSI content.[141] Kakinuma *et al.* recently applied their flame combustion route to synthesize a new non-carbon support, Gd-doped CeO$_2$. Gd-doping was used to enhance the conductivity of CeO$_2$ and Pt nanorods oriented along the (1 1 1) facets of the Gd-doped CeO$_2$. Scanning transmission electron microscopy

(STEM)-EDS analyses revealed PtCe alloy formation at the Pt and Gd-doped CeO$_2$ interface. The Pt/Gd-doped CeO$_2$ exhibited higher ORR activity and durability against 5000 FCCJ load cycles compared with commercial 46% w/w Pt/C in a half-cell employing 0.1 mol dm^{-3} HClO$_4$. DFT calculations indicated that the source of the high activity and durability was the exposure of Pt(1 1 1) facets and the oxygen-vacancy-mediated interfacial PtCe alloying.[142]

Most non-carbon oxide supports in PEFC cathodes developed to date have been Ti- and Sn-based oxides owing to their high stability, natural abundance, and high conductivity. In particular, the conductivity of the stoichiometric forms of these oxides (TiO$_2$ and SnO$_2$) can be greatly enhanced by cation doping, as described in Sections 2.1.1.2 and 2.1.1.3. Titanium suboxides also display metallic conductivity. Some of the oxide-supported Pt/Pt-alloy catalysts display excellent activity and durability in both a half-cell and a single cell after removal of any surface layers formed due to SMSIs. The mechanism to enhance the ORR activity of Pt/oxide catalysts by SMSIs has been described as follows. An electron transfer (donation) from the metal of the oxide to Pt causes a decrease in Pt d-band vacancy to downshift the Pt d-band center relative to the Fermi level. Consequently, the interaction between Pt and the oxygenated intermediates formed during the ORR (O, OH, or HO$_2$ shown in eqn 2(b–d)) decreases to facilitate enhanced ORR activity. The four-electron (4e$^-$) ORR in acidic media (eqn (2)) has been assumed to proceed *via* the elementary steps shown below:

$$O_2 + * \rightarrow O_2* \tag{2a}$$

$$O_2* + H^+ + e^- \rightarrow HO_2* \tag{2b}$$

$$HO_2* + H^+ + e^- \rightarrow H_2O + O* \tag{2c}$$

$$O* + H^+ + e^- \rightarrow HO* \tag{2d}$$

$$HO* + H^+ + e^- \rightarrow H_2O + * \tag{2e}$$

where * is the active site.[143,144] In many papers reporting SMSIs as the source of enhanced ORR activity or enhanced durability of Pt/oxide catalysts, the mechanism is described as an electron transfer from the metal of the oxide support to Pt, which downshifts the d-band center as mentioned above. An opposing view, in which an electron transfers from Pt to the oxide support[137,138] resulting in an upshift of the d-band center to enhance ORR activity/durability,[137–139] has also been reported. These competing claims suggest the presence of other factors in determining the ORR activity and durability of Pt/oxide. Matsumoto and coworkers experimentally determined the optimum Pt d-band center using 18 series of Pt/binary and ternary oxides formed on conducting cup-stacked carbon nanotubes (Pt/MO$_x$/CSCNT and Pt/M$_1$M$_2$O$_x$/CSCNT, where M = Ti, Nb, Ta, W, Y, Zr; M$_1$ = Ti, Nb, Ta; and M$_2$ = Nb, Ta, W) with different degrees of SMSIs. Fig. 7 shows the ORR activity in a half-cell as a function of Pt d-band center determined by the analysis of the XPS valence band region. The ORR activity increased with decreasing Pt d-band center from (a) (Pt/CB) to (g) (Pt/TiNbO$_x$(Ti : Nb = 1 : 6.6 in atomic ratio)/CSCNT) because
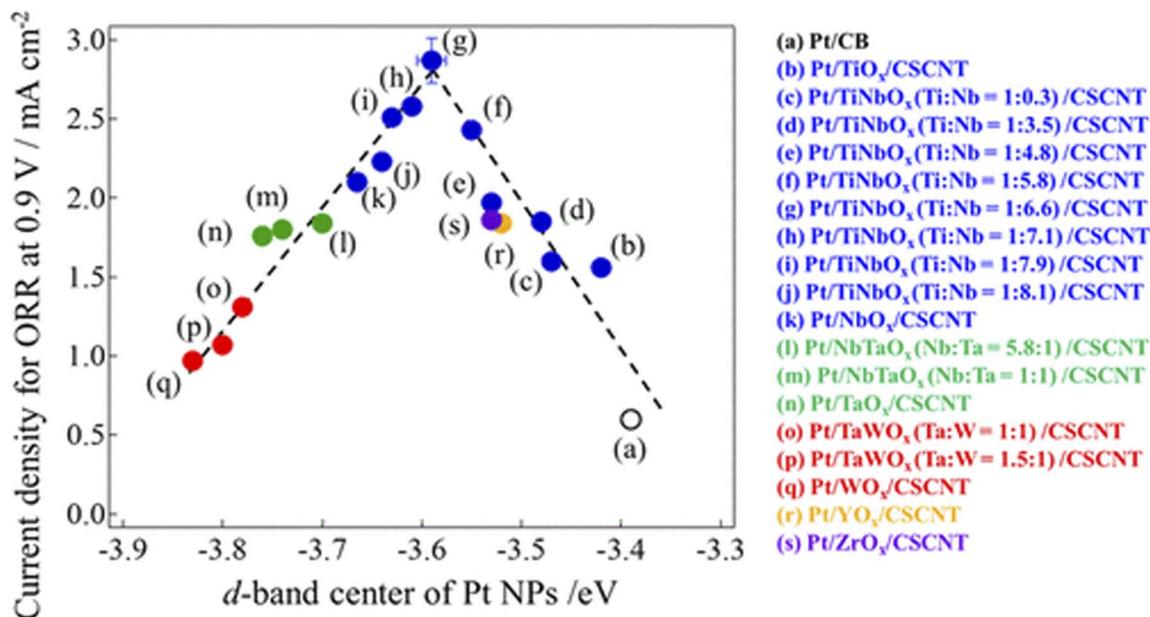
This journal is © The Royal Society of Chemistry 2024

J. Mater. Chem. A, 2024, **12**, 18636–18673 | **18651**

Fig. 7 Current density for the oxygen reduction reaction (ORR) at 0.9 V *versus* the d-band center of Pt nanoparticle curve. Reproduced with permission.[145] Copyright 2021, American Chemical Society.

the interaction between Pt and the oxygenated intermediates formed during the ORR (eqn 2(b–d)) decreases to facilitate enhanced ORR activity. Then ORR activity decreased with further decreasing d-band center to (*q*) (Pt/WO$_x$/CSCNT), as weak binding between Pt and the ORR intermediates lowered their coverage on the Pt surface.[145] The so-called volcano-type dependence of ORR activity on the Pt d-band center has attracted the attention of researchers in this field, and the durability of the optimized Pt/TiNbO$_x$ catalyst after removing the carbon support, CSCNT, is also of interest.

Another important point when selecting the oxide support is the leaching of metals and/or dopant metals from oxides as this significantly affects the durability, particularly in a single cell, as described in Sections 2.1.1.3 and 2.1.1.4. Although the leaching of Ti from TiO$_2$ and Ti$_n$O$_{2n-1}$ is not described in Sections 2.1.1.1 and 2.1.1.2, it has previously been reported and its effect is discussed later in Section 2.2.3.

**2.1.2 Platinum/platinum alloy catalysts on nitride supports**

2.1.2.1 Titanium nitride-supported catalysts. Some nitride materials are known to display a high conductivity and are thus expected to have use as supports in PEFC cathodes. The most studied nitride for PEFC cathodes is TiN, which is a well-known metallic nitride with a conductivity value of 4.6×10^4 S cm^{-1}, which is 17 orders of magnitude greater than that of a TiO$_2$ semiconductor.[42] Earlier studies by Avasarala *et al.* reported the potential[146] and drawbacks[147] of TiN as a support for PEFC cathodes. They used commercial TiN nanoparticles with a surface area of 40–55 m^2 g^{-1} as supports, and then created supported Pt nanoparticles with an average diameter of 2 nm *via* a polyol route. In their initial 2009 work, 20% w/w Pt/TiN exhibited a higher ORR activity and a higher ECSA in a half-cell employing 0.1 mol dm^{-3} HClO$_4$ at 333 K than commercial 20% w/w Pt/C, due to SMSIs. XPS analyses revealed that the

surface was a mixture of TiN and TiO$_2$, while the TiN content increased with Ar$^+$ sputtering time to expose the bulk.[146] A thin surface oxygen-rich oxynitride layer is known to be naturally formed by air moisture.[148] The conductivity of the thin surface layer was lower than that of bulk TiN,[42] although the impact on the initial ORR activity was negligible.[146] Later, in their second work in 2010, Avasarala *et al.* electrochemically treated TiN nanoparticles by cycling the potential between 0 and 1.2 V *versus* RHE at 50 mV s^{-1} for 16 h in 0.1 mol dm^{-3} HClO$_4$ at 333 K. Although the surface oxynitride layers were not transformed to a pure TiO$_2$ layer to maintain the oxynitride surface after 2 years of air exposure, the layer changed significantly during the 16 h-potential cycles, as revealed by XPS analyses. The high surface TiN content of the as-received TiN particles decreased to less than half (31.5% to 14.3%) after the potential cycles, while the oxide and oxynitride contents increased. Furthermore, dissolution was suggested by the XPS analyses, and the decrease in the ECSA of 20% w/w Pt/TiN during potential cycling was ascribed to the passivation nature of TiN.[147] Kakinuma *et al.* synthesized TiN nanoparticle supports using the radio-frequency plasma method to exhibit a high σ (850 S cm^{-1}) when compressed at 60% relative density.[149] Although the exact *P* value at 60% relative density is not clear, the reported σ of 850 S cm^{-1} is the highest among those reviewed in this paper. The resulting 19.5% w/w Pt/TiN displayed much higher durability against startup/shutdown cycles between 0.9 and 1.3 V (rectangular wave, held at 30 s at each potential) compared with commercial 47.9% w/w Pt/C and commercial 46.1% w/w Pt/graphitized carbon black. The TiN supports were crystallized in a nearly perfect cubic form, with the difference in durability between the findings of Avasarala *et al.*[147] and Kakinuma *et al.* ascribed to the degree of crystallization.[149] It is noted that the surface of Pt/TiN was covered with a thin (<1 nm) amorphous

18652 | *J. Mater. Chem. A*, 2024, **12**, 18636–18673

This journal is © The Royal Society of Chemistry 2024

layer, similar to Pt/(M)-TiO$_2$ and Pt/Sn$_{0.96}$Sb$_{0.04}$O$_{2-\delta}$, which could be removed by treating with hydrofluoric acid.[149] The presence of the surface amorphous layer on Pt in Pt/TiN indirectly suggests the presence of SMSIs between Pt and TiN, as reported for Pt/oxide catalysts. The ECSA of Pt/TiN was later enhanced by adding acetylene black powder to achieve an agglomerate structure in the half-cell[150] and a practical single cell with a large geometrical catalyst layer area of 196 cm^2.[151] The cell performance was also improved by adding acetylene black.[151] Seifitokaldani and Savadogo reported the use of TiO$_2$ and TiN mixture supports to maximize the benefits of TiO$_2$ stability and TiN conductivity.[152]

Since these first studies reported from the late 2000s to early 2010s, significant efforts have been made to control the morphology of TiN supports to improve their mass-transport properties. The Sung group reported scaffold-like TiN nanotube supports via an alkaline hydrothermal route. The concept was to reduce the contact resistance between TiN nanoparticles by using TiN nanotubes (NTs), as shown in Fig. 8(a). The σ-value of the TiN NTs was 118.73 S cm^{-1} at $P = 5$ tons cm^{-2}, which is 28 times higher than that of TiN nanoparticles (4.17 S cm^{-1}). 19.2% w/w Pt/TiN NTs displayed a higher activity than 19.7% w/w Pt/TiN nanoparticles and commercial 20% w/w Pt/C in a half-cell employing 0.1 mol dm^{-3} HClO$_4$ due to SMSIs. Both XPS Pt
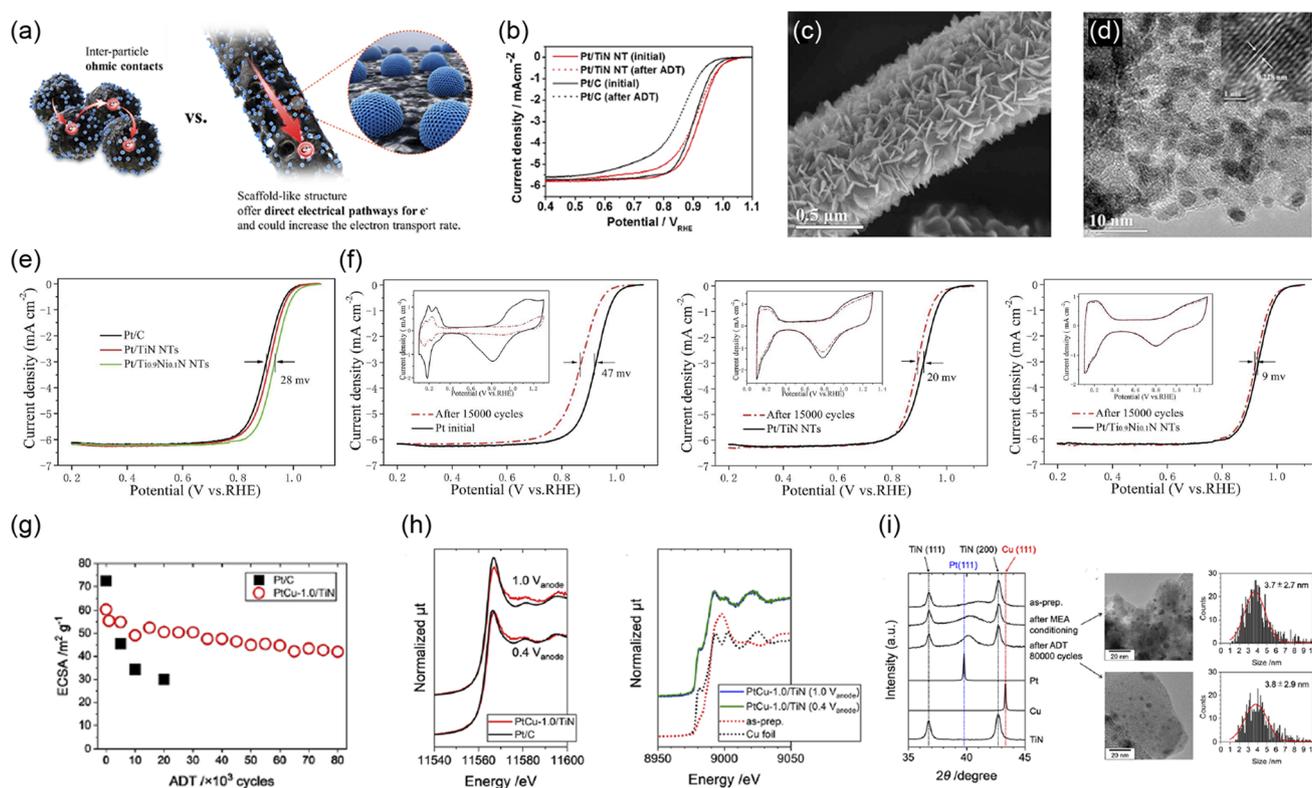
Fig. 8 (a) Schematic images of Pt/TiN nanoparticles and Pt/TiN nanotubes (NTs). (b) Rotating disk electrode (RDE) voltammograms of Pt/TiN NT and commercial Pt/C catalysts before and after an accelerated degradation test (ADT) (10 000 potential cycles between 0.6 and 1.2 V at 50 mV s^{-1}). Reproduced with permission.[153] Copyright 2016, American Chemical Society. (c) SEM and (d) TEM images of the Pt/Ti$_{0.9}$Ni$_{0.1}$N NTs. The inset of (d) shows the HR-TEM image. (e) RDE voltammograms of Pt/C, Pt/TiN NTs, and Pt/Ti$_{0.9}$Ni$_{0.1}$N NTs. (f) RDE voltammograms of (left) Pt/C, (center) Pt/TiN NTs, and (right) Pt/Ti$_{0.9}$Ni$_{0.1}$N NTs before (solid curves) and after (dashed curves) an ADT (15 000 potential cycles between 0.6 and 1.2 V at 50 mV s^{-1}). The inset shows their corresponding CVs. Reproduced with permission.[154] Copyright 2018, Royal Society of Chemistry. (g) Electrochemically active surface area (ECSA) versus FCCJ load cycle number curves of MEAs fabricated using two different cathode catalysts (commercial 50% w/w Pt/C and 20% w/w PtCu-1.0/TiN), in which PtCu-1.0 indicates the atomic ratio of Cu to Pt = 1. Commercial 50% w/w Pt/C catalysts were used in the anode. The cathode and anode platinum loadings were set at 0.11 and 0.5 mg$_{Pt}$ cm^{-2}, respectively, and the cathode catalyst layer contained 30% w/w carbon black, Ketjen Black. The anode and cathode gases were H$_2$ and 20% v/v O$_2$/N$_2$, respectively, at 93% RH and the cell temperature was kept at 353 K. (h) (left) Operando Pt L$_{III}$-edge XANES spectra of the MEAs with PtCu-1.0/TiN (red) and Pt/C (black) cathodes at 0.4 and 1.0 V cell voltages. The data were captured in transmission mode. (right) Operando Cu K-edge XANES spectra of the MEA with the PtCu-1.0/TiN cathode at a cell voltage of 1.0 V (blue) and 0.4 V (green) with those of as-prepared PtCu-1.0/TiN (powder, red dotted line) and Cu foil (black dotted line) as a reference. The data of samples were taken in X-ray fluorescence mode. In the MEAs used for operando XANES measurements, commercial 50% w/w Pd/C was used instead of Pt/C in the anode at a Pd loading of 0.5 mg$_{Pd}$ cm^{-2}. (i) (left) XRD patterns of PtCu-1.0/TiN collected from the cathode catalyst layer of the used MEA. The as-prepared catalyst (powder), after MEA conditioning and after an ADT with 80 000 FCCJ load cycles. XRD reference profiles of Pt (ICSD180981) and Cu (ICSD180109) from the ICSD database are presented. (right) TEM images with the particle size distributions of the PtCu-1.0/TiN catalyst collected from the cathode catalyst layer of the used MEA after the conditioning and after an ADT with 80 000 FCCJ load cycles. The red line in the particle size distribution shows Gaussian fitting to estimate the average particle size. Reproduced with permission.[155] Copyright 2024, Royal Society of Chemistry.

This journal is © The Royal Society of Chemistry 2024

J. Mater. Chem. A, 2024, 12, 18636–18673 | 18653

4f and XANES Pt L_3 edge analyses suggested electron transfer from Ti to Pt, similar to most Pt/TiO_2 catalysts. Further, the durability against 10 000 potential cycles between 0.6 and 1.2 V *versus* RHE also outperformed that of Pt/C, as shown in Fig. 8(b). XPS Ti 2p and XANES Ti K-edge analyses revealed that these spectra did not change during the durability test, indicating a stable TiN surface due to SMSIs.[153] The hydrothermal route is an attractive pathway to control the morphology of nanomaterials at low temperatures, typically below 473 K, and maintain a high surface area compared with a traditional solid-state reaction route, which needs a high synthesis temperature. The solvothermal route belongs to the family of hydrothermal routes and has also been used to synthesize TiN NT supports. When Pan *et al.* deposited 3.75 nm Pt nanoparticles on solvothermally synthesized TiN NTs with a BET surface area of 136 $m^2 g^{-1}$, 20% w/w Pt/TiN NTs showed superior ORR activity and durability compared with commercial 20% w/w Pt/C in a half-cell. Further, the TiN NTs themselves exhibited ORR activity without Pt to act as a co-catalyst to directly strengthen the ORR activity of Pt/TiN NTs.[156] Nan *et al.* developed Ni-doped TiN NTs *via* a solvothermal route. Randomly oriented and inter-connected nanosheets with a thickness of ~13 nm were formed on NTs with a diameter of ~930 nm, and Pt nanoparticles were formed on $Ti_{0.9}Ni_{0.1}N$, as shown in Fig. 8(c) and (d). The ORR activity and durability in the half-cell decreased in the following order: $Pt/Ti_{0.9}Ni_{0.1}N$ NTs > Pt/TiN NTs > commercial Pt/C, as shown in Fig. 8(e) and (f). However, the XPS Pt 4f peak binding energy displayed the opposite trend ($Pt/Ti_{0.9}Ni_{0.1}N$ NTs < Pt/TiN NTs < commercial Pt/C). The source of the higher ORR activity and durability of $Pt/Ti_{0.9}Ni_{0.1}N$ NTs compared with Pt/TiN NTs was ascribed to the electron transfer from Ni to Pt to downshift the d-band center and thus weaken the Pt-oxygenated species interactions (*i.e.*, SMSIs). Furthermore, hollow and porous structures were reported to enhance the activity by introducing efficient mass-transport properties.[154] In a half-cell employing a liquid electrolyte, the mass (O_2 molecules and protons) transport resistance is not large compared with that in a single cell employing a solid electrolyte, PFSI. Vertically aligned TiN nanorod array-supported PtPdCo alloy nanoparticles (PtPdCo/TiN) were used in a single cell by Jiang *et al.*[157] Vertically aligned organic whiskers, which are called nanostructured thin films (NSTFs)[158] and CNTs[159], have been used as supports to enhance the mass-transport properties of Pt-based catalyst layers since the 2000s. In particular, the Pt/NSTF catalyst layers are only 0.27 μm thick, while the thin catalyst layer is free from PFSI.[158] Similar to the previous study, Jiang *et al.* prepared vertically aligned TiN arrays with a thickness of 1.2 μm and formed thin PtPdCo/TiN catalyst layers directly on the surface of carbon paper without using PFSI. Water management to avoid water flooding in the thin catalyst layer remained necessary to enhance the cell performance.[157] Similar ordered catalyst layer structures have been investigated by other groups.[160] Besides controlling the morphology of TiN, doping other metals into TiN or alloying Pt with other metal(s) has also been utilized to enhance the ORR activity and durability of Pt/TiN. Xiao *et al.* reported $Ti_{0.9}Co_{0.1}N$ particles as supports for Pt nanoparticles and evaluated the ORR activity and durability in a half-cell.[161]

Their results were very similar to the results for $Ti_{0.9}Ni_{0.1}N$ NTs as reported by Nan *et al.*,[154] confirming the positive roles of SMSIs between Co and Pt nanoparticles. The Adzic group coated thin Pt layers (~0.11 nm) on TiNiN nanoparticles with a Ti-to-Ni atomic ratio of 19:1 (TiNiN@Pt) using a pulse deposition route.[162] Similar to the work by Nan *et al.*,[154] the activity and durability trend was as follows: TiNiN@Pt > TiN@Pt > commercial Pt/C. However, the trend in XPS Pt 4f binding energy differed from that of Nan *et al.*[154] (TiNiN@Pt < commercial Pt/C < TiN@Pt), and Adzic *et al.* reported that electrons were transferred from Ni to Pt in TiNiN@Pt but from Pt to Ti or N in TiN@Pt. The downshift of the Pt d-band center was suggested as the source of the high activity of TiNiN@Pt, while the source for the superior activity of TiN@Pt compared to Pt/C was not clear.[162] A unique combination of the Pt-alloy reported by Cui *et al.* and the mesoporous TiN *via* Zn-evaporation reported by Goodenough *et al.* produced a highly active and durable $Fe_3Pt/Ti_{0.5}Cr_{0.5}N$. The ORR mass activity in a half-cell was five times higher than that of Pt/C owing to the well-ordered Fe_3Pt catalyst, while the durability against FCCJ startup/shutdown cycles was enhanced by the anti-corrosion nature of the $Ti_{0.5}Cr_{0.5}N$ support. $Ti_{0.5}Cr_{0.5}N$ was also chemically stable after soaking in 0.1 mol dm^{-3} $HClO_4$ solution for 2 weeks, with no change in the XRD pattern. However, 6.5% and 26.8% of Fe leached from ordered and disordered Fe_3Pt/C catalysts, respectively, after 2 weeks of soaking.[163] Fe is known to catalyze the decomposition of H_2O_2 byproducts formed during the ORR (eqn (6)), to produce hydroxyl or hydroperoxyl radicals,[164,165] which degrade PFSI in catalyst layers and PFSI membranes.[166] Leached cations also readily exchange for H^+ in the sulfate group of PFSI to decrease the single-cell performance *via* decreased proton conductivity compared with the performance in a half-cell employing liquid electrolyte solution with abundant protons.[106] Measures to suppress Fe-leaching during the operation of PEFCs (*e.g.*, washing soluble Fe away using acidic solution prior to use) may be necessary for $Fe_3Pt/Ti_{0.5}Cr_{0.5}N$. Matsui *et al.* investigated the stability of PtCu alloy catalysts formed on commercial TiN particles (PtCu/TiN) in PEFC cathodes. The ECSA maintained 70% of the initial value after 80 000 FCCJ load cycles in a single cell, as shown in Fig. 8(g). Operando Pt L_{III}-edge and Cu K-edge XANES analyses revealed that Pt oxidation was suppressed, judging from the smaller difference between the height of the white line at 1.0 V and that at 0.4 V compared with Pt/C. In contrast, some Cu^{2+} species in the as-prepared PtCu/TiN were lost after incorporation in MEAs, and most of the Cu was found in the metallic state in the conditioned MEA as shown in Fig. 8(h). Changes in the PtCu alloy composition were observed after 80 000 cycles, although the size was kept almost constant according to the *ex situ* XRD/TEM analyses shown in Fig. 8(i). Furthermore, the TiN peaks in the XRD pattern exhibited no change during the 80 000 cycles, suggesting the high durability of TiN supports against the load cycles.[155] The results from different researchers indicate that once the surface oxynitride layers are formed on TiN, they prevent further oxidation of TiN, at least below 1 V, in PEFC cathodes. The coverage of the surface oxynitride layer is key for durability, particularly as 31.5% of surface TiN (68.5% of

18654 | *J. Mater. Chem. A*, 2024, **12**, 18636–18673

This journal is © The Royal Society of Chemistry 2024

oxynitride layer coverage) reported by Avasarala et al.[147] seems too high to cause degradation. The surface composition is also discussed in Section 3.

2.1.2.2 Other nitride (WN, VN, BN)-supported catalysts. Compared with TiN, other nitrides have attracted less attention, mainly due to their poorer conductivity and stability. Tungsten nitride (WN) and vanadium nitride (VN) have been used as supports by forming composites with carbon materials to enhance their conductivity.[167,168] Tsai et al. recently coated VN thin films on TaC as a composite support for Pt nanoparticles, as the bulk conductivity of TaC is the highest among the transition metal carbides. However, the single-cell performance of the optimized 2.82% w/w Pt/VN@TaC cathode was lower than that of commercial Pt/C. Although the power density per platinum mass of the Pt/VN@TaC cathode exceeded that of commercial Pt/C owing to the low Pt loading caused by the low Pt mass fraction, an increase in the Pt mass fraction is necessary for practical use, and ADT results are not reported.[169] Recently, porous boron nitrides (p-BNs) have been used as supports for Pt nanoparticles without using carbon materials.[170] The hexagonal structure of these materials is similar to that of graphite, and the inertness makes them suitable as support materials. BN has been used as a catalyst itself and as a support material for Au catalysts, although the ORR activity remains only moderate.[171,172] Li et al. deposited Pt nanoparticles with an average diameter of 2.45 nm onto the edge of micropores in micro-sized rod-like p-BNs. They reported that BN is polar with an electron-deficient B-site that accepts electrons from Pt and an electron-rich N-site that donates electrons to Pt. This allows an electron donation-back process, which strengthens the SMSIs according to DFT calculation results, XPS, and electrochemical analyses with a half-cell configuration.[170]

2.2 Anode catalysts

As shown in Fig. 2, the anode potential increases above that of the cathode to reverse the cell voltage during H_2 starvation if no system-level measures have been taken. Catalysts tolerant to cell reversal are known as reversal tolerant anode (RTA) catalysts, and they have been developed to avoid damage at high potentials. Unlike the widely used startup/shutdown and load cycle protocols for evaluating the durability of supports and the catalyst, respectively, at the cathode,[16,17] no protocol for cell reversal has yet been standardized, and the tested potential and duration at the potential differ in different publications. Therefore, a precise comparison of the reported durability results is not possible in this subsection. Furthermore RTA, ORR-inactive anodes have been reported to avoid high cathode potentials during startup/shutdown, as this effect is caused by anode ORR catalysis, as shown in Fig. 1. In this subsection, RTA catalysts and ORR-inactive anodes are reviewed.

2.2.1 RTA catalysts. Once a cell reversal proceeds in PEFCs, the anode potential increases to 2.0 V or even higher, as shown in Fig. 2, to oxidize carbon supports in Pt/C as described in Section 1. To date, two pathways have been reported to avoid or reduce damage from the high anode potential caused by H_2 starvation without relying on system-level measures: (1) the use

of non-carbon supports that are more resistant to corrosion than carbon materials and (2) the addition of OER catalysts to avoid the COR by maintaining the anode potential in the OER region, which is much lower than that in the absence of OER catalysts. In terms of the first option, oxide-supported Pt catalysts developed for PEFC cathodes may be used, and as such, WO_3, SnO_2, and Ti_4O_7 have been applied as support materials in PEFC anodes. Dou et al. reported WO_3 (ref. 173) and SnO_2 (ref. 174) nanoclusters using mesoporous silica (SBA-15) templates as supports for Pt nanoparticles. Both 6.8% w/w Pt/WO_3 and 14% w/w Pt/SnO_2 catalysts displayed little change in CVs (thus ECSAs) after being held at 1.6 V versus RHE in 0.5 mol dm^{-3} H_2SO_4 for 10 h.[173,174] Ioroi and Yasuda reported excellent durability for Pt/Ti_4O_7 with the addition of a small amount of Ir OER catalyst in a single-cell anode at potentials exceeding those used by Dou et al.[175] Their approach is a combination of pathways (1) and (2). Anode catalyst layers were prepared by mixing commercial Ir black with either Pt/C, Pt/graphitized carbon black (GKB; Ketjen Black), or Pt/Ti_4O_7. Then, the single cell was reversed according to the protocol shown in Fig. 9(a), with the results shown in Fig. 9(b). The cell voltage during cell reversal increased with Ir loading and did not reach −2.0 V after 2 h of cell reversal at higher Ir loading, regardless of the anode catalyst type. This indicates that the OER catalysis of Ir suppressed the increase in anode potential. However, the impact of Ir loading on the cell performance differed for the three catalyst layers. The MEA with Pt/C + Ir anode catalyst layers at an Ir loading of 0.044 mg$_{Ir}$ cm^{-2} degraded significantly during cell reversal to increase the cell resistance by more than twice, suggesting the oxidation of carbon black. The decrease in cell performance and the increase in cell resistance during cell reversal were significantly suppressed when the Ir loading was increased to 0.099 mg$_{Ir}$ cm^{-2}, consistent with the previous results on Pt/C + IrO_2 anode catalyst layers with a much shorter cell reversal time reported by Lim et al.[21] A similar trend was observed from the MEA with Pt/GKB + Ir anode catalyst layers, although the Ir loading was much lower than for the Pt/C + Ir anode catalyst layers, indicating the higher durability of GKB than carbon black. The MEA with Pt/Ti_4O_7 + Ir anode catalyst layers exhibited an enhanced performance compared with the other two anode catalyst layer types, with minimal degradation at much lower Ir loadings. Furthermore, Ir/Ti_4O_7 anode catalyst layers prepared by the authors displayed high durability against cell reversal. As Ir is not a good ORR catalyst, Ir/Ti_4O_7 was suggested to suppress the cathode potential during startup/shutdown.[175] Later, Li et al. added IrO_x/Ti_4O_7 to the Pt/C anode catalyst layers and performed cell reversal tests using the protocol shown in the middle of Fig. 9(a), modified to include the use of air as an oxidant at the cathode and the removal of a set reversal time limit. The OER mass activity of the synthesized amorphous IrO_x catalyst was significantly increased by a factor of three after being supported on Ti_4O_7 particles with a size of 80–150 nm due to the suppressed agglomeration of IrO_x. The IrO_x/Ti_4O_7 OER catalyst did not affect the single-cell performance after being added to the Pt/C anode catalyst layer, and the Pt/C + IrO_x/Ti_4O_7 anode did not degrade after cell reversal for 530 min. The carbon black in Pt/C was protected by IrO_x/Ti_4O_7, while the IrO_x

This journal is © The Royal Society of Chemistry 2024

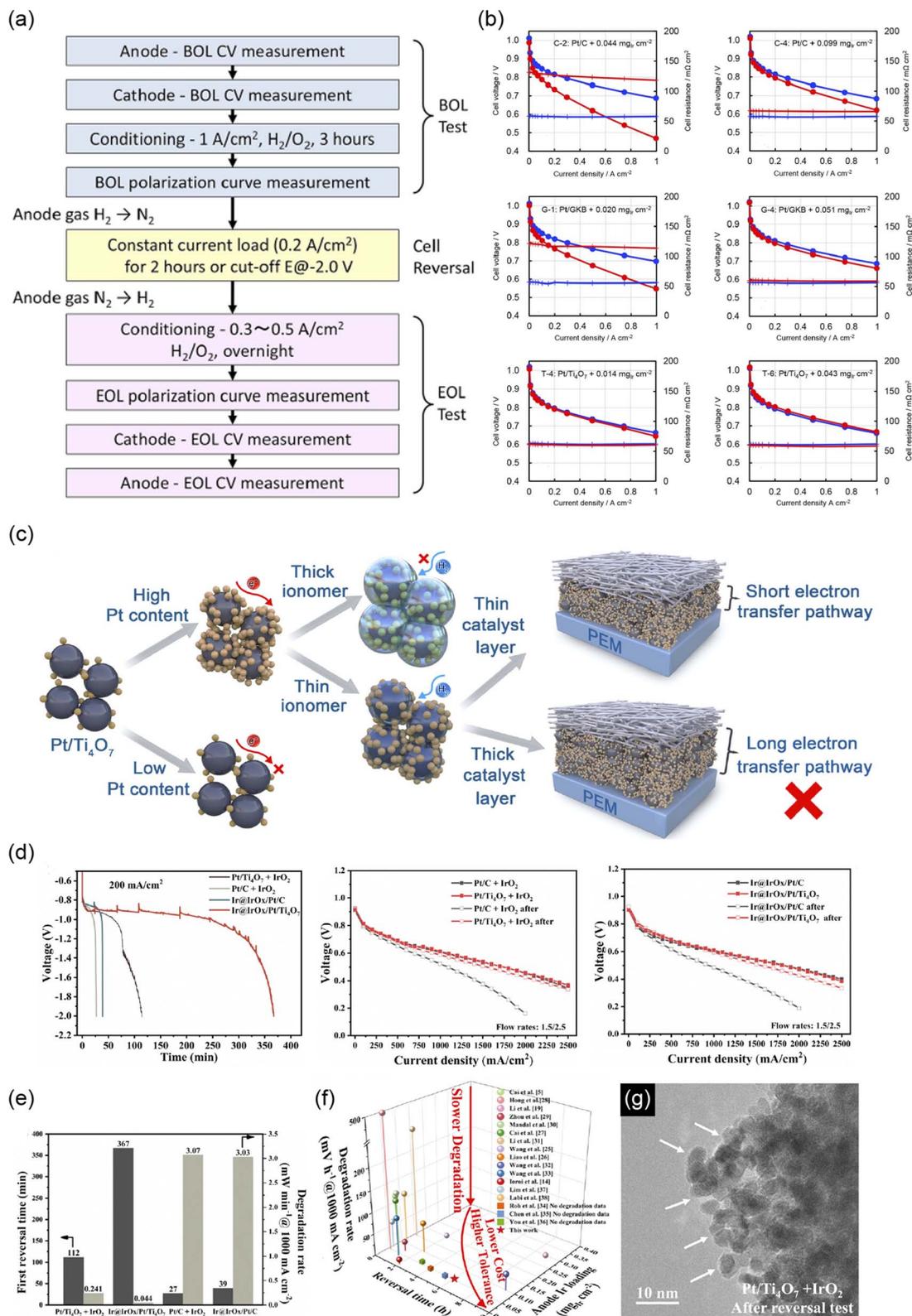J. Mater. Chem. A, 2024, 12, 18636–18673 | 18655

Fig. 9 (a) Evaluation protocol of reversal tolerant anodes (RTAs) at the beginning of life (BoL), at cell reversal, and at the end of life (EoL). (b) Cell voltage (●) and cell resistance (+) *versus* current density curves of MEAs at the BoL and EoL with (top) Pt/C, (middle) Pt/GKB (graphitized Ketjen Black), and (bottom) Pt/Ti$_4$O$_7$ anode catalyst layers mixed with Ir black. All three RTAs were evaluated at the two different Ir loadings shown in the legend. Commercial Pt/C catalysts were used for all cathodes. The anode and cathode Pt loadings were 0.10 ± 0.02 and 0.50 ± 0.05 mg$_{Pt}$ cm^{-2}, respectively. The anode and cathode were supplied with fully humidified H$_2$ and O$_2$, respectively, to evaluate the cell performance and the cell temperature was set at 353 K. Reproduced with permission.[175] Copyright 2020, Elsevier. (c) Schematic image of the optimization of the Pt/Ti$_4$O$_7$ catalyst and the anode catalyst layer for the cell performance. (d) (left) Cell voltage *versus* time curves of MEAs with four anode catalyst layers, Pt/

18656 | *J. Mater. Chem. A*, 2024, **12**, 18636–18673

This journal is © The Royal Society of Chemistry 2024

loading was 0.096 mg cm^{-2}, which roughly equates to 0.082 mg$_{Ir}$ cm^{-2} Ir loading at $x = 2$;[176] this value is approximately six times higher than that used by Ioroi and Yasuda.[175] The RTA was a mixture of Pt/Ti$_4$O$_7$ and Ir black in the work by Ioroi and Yasuda[175] and Pt/C and IrO$_x$/Ti$_4$O$_7$ in the work by Li et al.[176]

In addition to the physical mixing used in these recent studies,[175,176] in 2024, Li et al. synthesized Pt and core–shell structured Ir@IrO$_x$ on fine Ti$_4$O$_7$ particles.[37] The Ti$_4$O$_7$ supports were synthesized via a modified version of the carbothermal reduction reaction reported by our group,[36] to yield a BET surface area of 166 m^2 g^{-1}; then 3–4 nm Pt nanoparticles were deposited on Ti$_4$O$_7$ via ethanol reduction route. Next, the Pt mass fraction in Pt/Ti$_4$O$_7$, PFSI mass fraction in the anode catalyst layers, and Pt loading at the anodes were carefully optimized to 40% w/w, 4% w/w, and 0.1 mg$_{Pt}$ cm^{-2}, respectively, to yield a single-cell performance matching that of a commercial Pt/C anode. The schematic diagram for this process is shown in Fig. 9(c). Ir@IrO$_x$ OER catalysts were then supported on the optimized 40% w/w Pt/Ti$_4$O$_7$ via a hydrothermal route. At an Ir loading of 0.05 mg$_{Ir}$ cm^{-2}, the Ir@IrO$_x$/Pt/Ti$_4$O$_7$ anode catalysts exhibited considerably greater tolerance to cell reversal than Ir@IrO$_x$/Pt/C, a physical mixture of Pt/Ti$_4$O$_7$ + IrO$_2$ and Pt/C + IrO$_2$, as shown in Fig. 9(d) and (e). Cell reversal was performed using the protocol shown in the middle of Fig. 9(a), modified to include the use of air as an oxidant at the cathode and the removal of a set reversal time limit. The results shown in Fig. 9(d) and (e) clearly indicate two important aspects: (i) compared to the physical mixture, depositing Pt and Ir@IrO$_x$ nanoparticles on Ti$_4$O$_7$ supports produces much higher reversal tolerance in the anodes and (ii) Ti$_4$O$_7$ is considerably more tolerant to cell reversal than carbon black. Considering the results in Fig. 9(d) and the results of Li et al. for Pt/C + IrO$_x$/Ti$_4$O$_7$ RTA,[176] we can see that considerably higher Ir loading is necessary for Pt/C than for carbon-support-free Ti$_4$O$_7$ supports in the anodes. The Ir@IrO$_x$/Pt/Ti$_4$O$_7$ anode cell reversal time, defined as the time to reach a cell voltage of −2.0 V during cell reversal, of 367 min was compared with other values reported to date, as shown in Fig. 9(f). The Ir loading used by Li et al.[37] was 3.6 times higher than that used by Ioroi and Yasuda, and it is noted that the 2 h cell reversal cut-off time (shown as a red circle in Fig. 9(f) against "Ioroi et al. [14]") was not the cell reversal time defined by Li et al., not sufficient to reach a cell voltage of −2.0 V.[175] Although the reversal tolerance of the Ir@IrO$_x$/Pt/Ti$_4$O$_7$ anode is high, some degradation in cell performance after cell reversal can be seen in Fig. 9(d). The source was investigated using several techniques. A TEM image of the Pt/Ti$_4$O$_7$ + IrO$_2$ anode after the cell reversal test is shown in Fig. 9(g). The Pt nanoparticles were encapsulated by a thin layer of TiO$_x$ due to

SMSIs, as indicated by the white arrows. Combined with the electrochemical impedance spectra and CVs after cell reversal and XPS analyses, it was concluded that Ti$_4$O$_7$ is stable and that the thin layer on the Pt nanoparticles is permeable to protons and H$_2$ and does not affect HOR activity. However, the formation of the thin TiO$_x$ layer oxidizes the Pt surface, which impedes the electron transfer to degrade cell performance.[37] These results indicate that the combination of the two pathways mentioned at the beginning of this subsection (the use of Ir-based OER catalysts and non-carbon supports) significantly suppresses damage due to cell reversal. However, Ir is an extremely expensive and scarce metal, with a 2021–2023 price approximately five times higher than that of Pt.[177] Non-Ir catalysts have been reported to exhibit higher OER activity and durability than IrO$_2$ in alkaline media; although, as with non-Pt ORR catalysts, they are not active or durable in acidic counterparts. Therefore, attempts have been made to reduce Ir loading in RTAs through means such as the use of IrO$_2$/RuO$_2$ composite,[178,179] PtRu alloy,[180,181] and Co-doped PtRu alloy[182] OER catalysts, with the support of carbon black or graphitized carbon black. Furthermore, the effects of the crystallinity, preferred orientation of IrO$_x$,[183] and microstructure of IrO$_x$[184] on cell reversal performance have been reported. When (1) these modified composite or alloy OER catalysts[178–182] are supported on Pt/Ti$_4$O$_7$ or other Pt/oxides and/or (2) properties of IrO$_x$[183,184] in Ir@IrO$_x$/Pt/Ti$_4$O$_7$ without carbon supports are tuned, the Ir loading may be reduced. Two-dimensional transition metal carbides, known as MXenes, with a composition of Ti$_3$C$_2$T$_z$ were recently used as supports for Pt particles in PEFC anodes, where T$_z$ is the surface terminal group (typically –O, –OH, or –F). Cell reversal tests were performed using the protocol shown in Fig. 9(a), and the tolerance to 2 h of cell reversal was improved by Ta-doping in the composition (Ti$_{0.95}$Ta$_{0.05}$)$_3$C$_2$T$_z$. The single-cell performance with a Pt/(Ti$_{0.95}$Ta$_{0.05}$)$_3$C$_2$T$_z$ anode was moderate, although it did not significantly degrade after the 2 h reversal without OER catalysts. Although the mechanism for the durability enhancement was not clearly described and the stability of the Ta-dopants has not been shown,[185] the metal doping used in cathode non-carbon supports can be applied to non-carbon anode supports other than MXenes.

2.2.2 ORR-inactive anodes to suppress cathode degradation during startup/shutdown. Cathode degradation during the startup/shutdown of PEFCs via the reverse current decay mechanism shown in Fig. 1 can be suppressed if the anodes are inactive toward the ORR. Several approaches have been applied to produce such anodes. The first four approaches reviewed in this subsection use selective anode HOR catalysts, which maintain HOR activity while simultaneously impeding ORR

Ti$_4$O$_7$ + IrO$_2$, Pt/C + IrO$_2$, Ir@IrO$_x$/Pt/C, and Ir@IrO$_x$/Pt/Ti$_4$O$_7$ during cell reversal. (center) Cell voltage versus current density curves of MEAs with two anode catalyst layers, Pt/Ti$_4$O$_7$ + IrO$_2$ and Pt/C + IrO$_2$, before and after cell reversal. (right) Cell voltage versus current density curves of MEAs with two anode catalyst layers, Ir@IrO$_x$/Pt/C and Ir@IrO$_x$/Pt/Ti$_4$O$_7$, before and after cell reversal. The cathode for all MEAs was commercial Pt/C. The anode and cathode Pt loadings were set at 0.1 and 0.4 mg$_{Pt}$ cm^{-2}, respectively. The Ir loading was set at 0.05 mg$_{Ir}$ cm^{-2}. The anode and cathode were supplied with fully humidified H$_2$ and air, respectively, to evaluate the cell performance, and the cell temperature was set at 353 K. (e) First reversal time and degradation in the maximum power density of the four RTAs shown in (d). (f) Comparison of the anode Ir loading, first reversal time, and degradation date of RTAs reported in the literature. (g) TEM image of Pt/Ti$_4$O$_7$ + IrO$_2$ anode catalysts after cell reversal. Reproduced with permission.[37] Copyright 2024, Royal Society of Chemistry.

This journal is © The Royal Society of Chemistry 2024

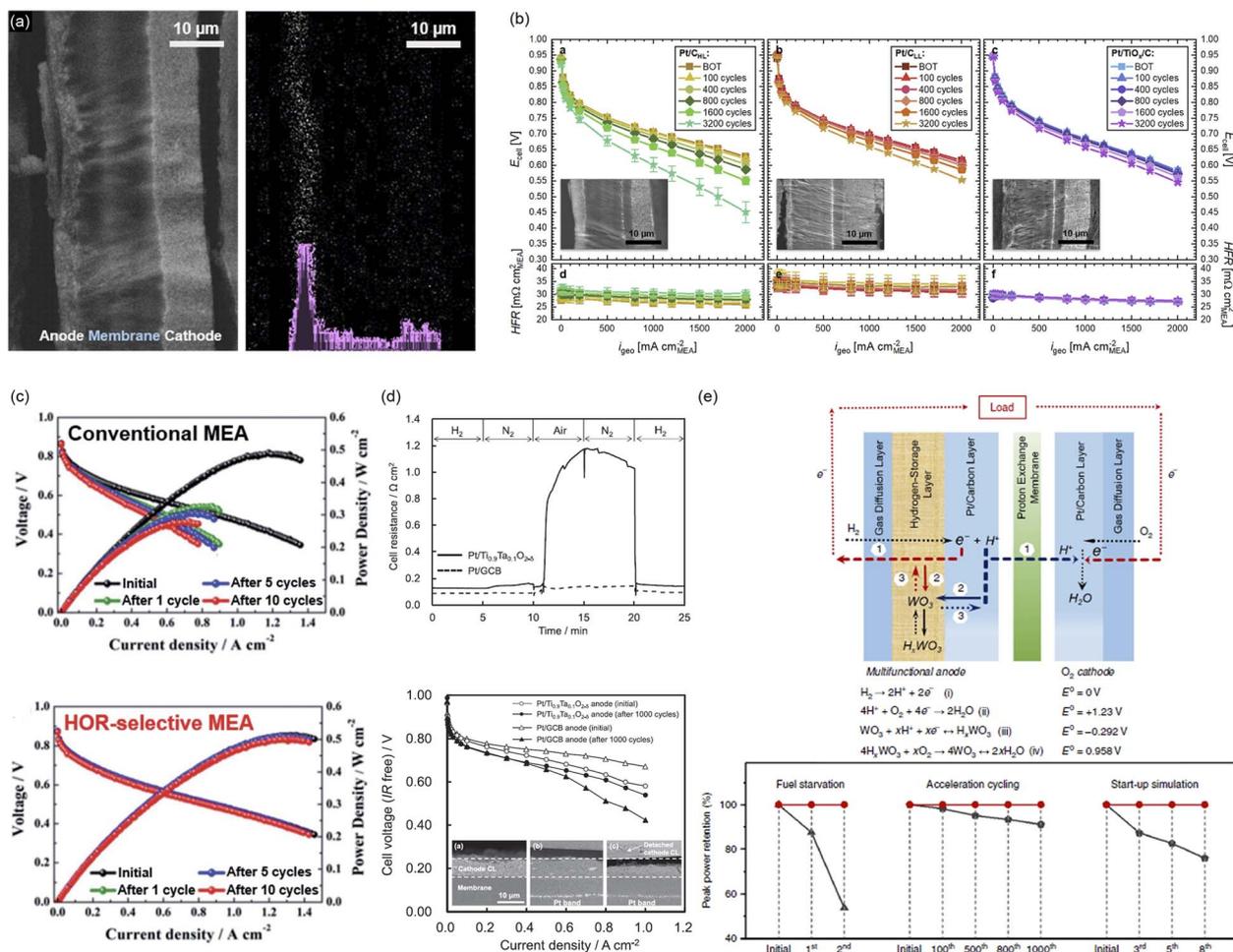J. Mater. Chem. A, 2024, **12**, 18636–18673 | 18657

activity. A fifth approach is to insert a multifunctional layer between the conventional Pt/C catalyst layer and GDL that stores hydrogen and inhibits the ORR.

2.2.2.1 Thin layers on Pt surfaces. Most research into suppressing cathode damage during startup/shutdown by novel anodes has adopted this approach. The thin layers required are formed *via* several pathways in order to inhibit O_2 transport, suppressing the ORR on Pt and allowing proton and H_2 permeation to achieve the HOR. The Marković group attached a self-assembled monolayer of calix[4]arene molecules on a Pt (1 1 1) surface without any loss in HOR activity but with significantly reduced ORR activity in a half-cell employing 0.1 mol dm^{-3} $HClO_4$. From the CVs, the Pt surface coverage was well controlled and at the maximum, 98% of the Pt (1 1 1) surface was covered by calix[4]arene, while the remaining 2% Pt surface was sufficient to maintain the original HOR activity of uncovered Pt (1 1 1). The ORR activity of Pt (1 1 1) decreased with increasing surface coverage, with no limiting current plateau. Instead, a certain amount of H_2O_2 was produced *via* a two-electron reaction (eqn (6)) after the coverage.[186] Later, Marković *et al.* applied a self-assembled monolayer of calix[4] arene to commercial Pt/C and commercial Pt/NSTF catalysts, and the HOR selectivity was confirmed in a half-cell.[187] The self-assembled monolayer approach was also reported by Yun *et al.*, who attached dodecanethiol on the surface of commercial Pt/C. The HOR-selective Pt/C + dodecanethiol anode exhibited less loss in cell performance than the Pt/C anode after 10 startup/shutdown cycles in a single cell.[188] The startup/shutdown cycle protocol for a single cell with HOR-selective anodes used by Yu *et al.*[188] and other researchers[189–191] involved injecting air into the anodes to produce H_2/air front (interface between Region A and B at anode in Fig. 1) instead of the widely used potential cycles between 1.0 and 1.5 V *versus* RHE as recommended by FCCJ/DOE. This was because the anode potential was suppressed owing to the decreased ORR activity at the anode and did not increase to 1.5 V. As described in Section 2.1.1.2, thin TiO_x layers on Pt nanoparticles in Pt/TiO_x formed by SMSIs also inhibit O_2 transport, while protons and H_2 can pass through, making Pt/TiO_x a selective HOR catalyst in a half-cell.[73,99] Stühmeier *et al.* evaluated the startup/shutdown durability of Pt/TiO_x/C, where C is carbon black Vulcan XC-72R, in a single-cell anode. Fig. 10(a) shows a cross-sectional SEM image and corresponding EDS line scan profile of a MEA with a 13.0% w/w Pt/TiO_x/C anode and commercial 45.6% w/w Pt/C cathode. The image depicts the MEA after the initial cell performance evaluation. A number of Ti ions dissolved to permeate the membrane and were deposited at the cathode, with an EDS signal intensity slightly exceeding the background level. The dissolved Ti ions decreased the cell performance due to decreasing proton conductivity in both catalyst layers and the membrane, for example. Furthermore, the HOR selectivity of Pt/TiO_x/C was moderate, and only slightly higher than that of Pt/C in a single cell. However, the Pt/TiO_x/C anode nevertheless mitigates the degradation of the Pt/C cathode during startup/shutdown in a single cell to a greater extent than Pt/C, as shown in Fig. 10(b). The proposed mechanism by Stühmeier *et al.* is a pseudo-capacitance effect due to the reversible

spillover of the adsorbed hydrogen atoms from Pt onto TiO_x supports.[189] The careful and systematic studies on Pt/TiO_x/C conducted by Stühmeier *et al.*[73,99,189] suggest the importance of the degree of HOR selectivity and Ti dissolution. Although the ORR activity of Pt/TiO_x/C is suppressed by the presence of thin TiO_x surface layers, it is still non-negligible, as shown in Fig. 5(k). Jang *et al.* reported less ORR active, and thus more HOR selective, catalysts that avoid leaching of cations by encapsulating Pt nanoparticles on carbon black with graphitized carbons to block O_2, while H_2 and protons pass through the shell.[190] They selected a graphitized carbon "molecular sieve" because the organic molecules reported in previous papers[186–188] may become detached during long-term operation.[190] The carbon molecular sieve layers originating from a Pt acetylacetonate precursor successfully covered the Pt nanoparticles to suppress size and ORR activity in a half-cell, even after high-temperature annealing. The ORR activity increased dramatically after 3000 potential cycles between 0.05 and 1.05 V *versus* RHE in 0.1 mol dm^{-3} $HClO_4$, indicating the detachment of carbon molecular sieve layers that were not annealed or annealed at a low temperature (873 K). However, the ORR activity during the 3000 cycles did not increase when the catalyst was annealed at 1173 K to increase the degree of graphitization of the carbon molecular sieve layers. The graphitized carbon molecular sieve layers successfully blocked O_2-transport, while H_2 and protons could permeate through to exhibit high HOR selectivity in both a half-cell and a single cell (Fig. 10(c)). The MEA with HOR-selective carbon-encapsulated Pt anodes displayed a negligible change in single-cell performance, in contrast to conventional Pt/C anodes which were severely degraded after 10 simulated startup/shutdown cycles.[190] All anode Pt catalysts based on the thin layer approach utilized carbon supports. The damage caused by startup/shutdown was suppressed by these anode catalysts, although the carbon supports at the anode will be oxidized during cell reversal. Similar to the cathode, the removal of carbon supports from these anode catalysts is of interest.

2.2.2.2 Control of support conductivity during operation. Shintani *et al.* switched the conductivity of Ta-doped TiO_2 ($Ti_{0.9}Ta_{0.1}O_{2-\delta}$) supports between high under H_2 and low under an air atmosphere in the anode, respectively, to impede the ORR at startup/shutdown and to promote the HOR under normal operation. The concept is to suppress electron transport from the $Ti_{0.9}Ta_{0.1}O_{2-\delta}$ support to the Pt-catalyst surface by decreasing the conductivity of $Ti_{0.9}Ta_{0.1}O_{2-\delta}$ only in the presence of O_2 contaminants during startup/shutdown, thus maintaining $Ti_{0.9}Ta_{0.1}O_{2-\delta}$ conductivity and HOR activity on Pt in the presence of H_2 gas during normal anode operation. Consistent with the known decrease in the conductivity of conducting oxide nanoparticles in an oxidizing atmosphere, the resistance of a cell with a Pt/$Ti_{0.9}Ta_{0.1}O_{2-\delta}$ anode was one order of magnitude higher in air than in H_2, as shown in Fig. 10(d). The Pt/$Ti_{0.9}Ta_{0.1}O_{2-\delta}$ anode exhibited higher durability against 1000 simulated startup cycles than graphitized carbon black-supported platinum (Pt/GCB), as shown in Fig. 10(d). The detachment of carbon supports due to corrosion at the Pt/GCB

18658 | *J. Mater. Chem. A*, 2024, **12**, 18636–18673

This journal is © The Royal Society of Chemistry 2024

Fig. 10 (a) (left) Cross-sectional SEM image of an MEA with a Pt/TiO$_x$/C anode after initial cell performance characterization and (right) the corresponding EDS line profile of Ti depicted in purple. (b) Cell potential versus current density ($E_{cell} - i_{geo}$) curves of MEAs with three different anodes (commercial 19.8% w/w Pt/C at high and low Pt loading, Pt/C$_{HL}$, and Pt/C$_{LL}$, respectively) and 13.0% w/w Pt/TiO$_x$/C at 353 K. The anode Pt loading in Pt/C$_{HL}$ and Pt/TiO$_x$/C was set at 45 $\pm$ 5 μg$_{Pt}$ cm^{-2} and that in Pt/C$_{LL}$ was set at one-third that of Pt/C$_{HL}$ (15 $\pm$ 2 μg$_{Pt}$ cm^{-2}). In all MEAs, the cathode catalysts were commercial 45.6% w/w Pt/C with 0.40 $\pm$ 0.04 mg$_{Pt}$ cm^{-2} Pt loading. The anode and cathode were supplied with H$_2$ and O$_2$, respectively, with 90% RH. The corresponding high frequency resistance of each cell was also shown as a function of i_{geo} at the bottom. Reproduced with permission.[189] Copyright 2023, Elsevier. (c) Cell voltage versus current density curves of MEAs fabricated using two different anode catalysts, (top) commercial 20% w/w Pt/C and (bottom) 20% w/w Pt@C/C 900; carbon black-supported Pt nanoparticles encapsulated in nanoporous carbon shells annealed at 1173 K; before and after 1, 5 and 10 simulated startup/shutdown cycles. In both MEAs, the cathode catalysts were commercial 20% w/w Pt/C, and the Pt loading was 0.2 mg$_{Pt}$ cm^{-2} in the anode and cathode. The anode and cathode were supplied with humidified H$_2$ and air, respectively, and the cell temperature was maintained at 343 K. Reproduced with permission.[190] Copyright 2019, American Chemical Society. (d) (top) Cell resistance versus time curves of MEAs with two different Pt/Ti$_{0.9}$Ta$_{0.1}$O$_{2-\delta}$ anodes (solid line) and Pt/GCB (dashed line) measured at 338 K with humidified (348 K dew point) H$_2$, N$_2$, and air. (bottom) IR-free cell voltage versus current density curves of MEAs with two different Ti$_{0.9}$Ta$_{0.1}$O$_{2-\delta}$ anodes (circles) and Pt/GCB (triangles) at 338 K. In all MEAs, commercial Pt/GCB was used at the cathode. The anode and cathode Pt loading was set at 0.1 mg$_{Pt}$ cm^{-2} and 0.3 mg$_{Pt}$ cm^{-2}, respectively. The anode and cathode were supplied with fully humidified H$_2$ and air, respectively. The utilization of H$_2$ and O$_2$ in air was set at 70% and 40%, respectively. For both MEAs, open and solid symbols represent the curves before and after 1000 air/air startup cycles. The inset shows the cross-sectional SEM images of the Pt/GCB cathode regions; (i) MEA with the Pt/GCB anode before 1000 startup cycles and MEAs after the cycles with (ii) the Pt/Ti$_{0.9}$Ta$_{0.1}$O$_{2-\delta}$ anode and (iii) the Pt/GCB anode. Reproduced with permission.[191] Copyright 2015, Elsevier. (e) (top) Schematic image of an MEA for a hybrid PEFC with a WO$_3$/CNT-based multifunctional anode. The cell functions through reactions (i) and (ii), whereby electrons and protons proceed through pathway 1. The WO$_3$ layer serves as a rapid-response hydrogen reservoir, storing and releasing electrons and protons based on reaction (iii) through pathways 2 and 3, respectively. The WO$_3$ layer also serves as an O$_2$ scavenger invading the anodes through reaction (iv) and as a regulator for the hydrogen-disassociation reaction (i). (bottom) Retention of the peak power density of the three control cells and a hybrid cell after three different ADTs. H$_2$ starvation tests were performed by switching the H$_2$ supply to a N$_2$ flow to a control cell and hybrid cell while operating under a constant current density of 0.2 A cm^{-2}. The cell voltage was recorded during the measurement, and each cycle lasted for 10 s after switching to a N$_2$ flow. Acceleration tests were conducted by oscillating the current output of a control cell and the hybrid cell between 50 and 1000 mA cm^{-2}, with a holding time of 120 and 30 s, respectively. Startup tests were performed using the following steps: both cells were kept at an open-circuit voltage (OCV) supplied with H$_2$ and O$_2$ at the anode and cathode, respectively. The gas for the anodes was switched from H$_2$ to N$_2$ (30 mL min^{-1}) for 10 s to purge the anode compartment. Then, 1 cm^3 of air was injected into the anodes, and the equilibrium OCV of the cells was recorded. The cells were then maintained at a constant voltage of 0.8 V for a period of 20 s. The hybrid cell was used throughout all three tests

This journal is © The Royal Society of Chemistry 2024

J. Mater. Chem. A, 2024, 12, 18636–18673 | 18659

cathode was successfully suppressed by the $Pt/Ti_{0.9}Ta_{0.1}O_{2-\delta}$ anode, as shown in the inset.[191]

2.2.2.3 Small Pt clusters. Luo *et al.* reported an HOR-selective Pt/TiN catalyst with extremely low Pt mass fractions. Small Pt clusters, which are not visible on the TEM image, were deposited on TiN. The Pt clusters lacked ordered facets and were mostly in an unsaturated coordination environment to display low ORR activity and high HOR activity in a half-cell. The difference in ORR and HOR activity on Pt/TiN was attributed to differences in O_2 and H_2 bond types, which are sensitive to the coordination environment of Pt.[193] Kanai *et al.*[194] reported HOR-selective catalysts based on atomic Pt supported on covalent triazine frameworks and carbon black composites (Pt/CTF). In both studies, the Pt mass fractions were one or two orders of magnitude lower than those of commercial Pt/C (0.29–1.46% w/w for Pt/TiN[193] and 2.8% w/w for Pt/CTF).[194] Such low Pt mass fractions can increase the thickness of the anode catalyst layers in MEAs. The effect of Pt loading at anode catalyst layers in MEAs on thickness and HOR performance is of interest.

2.2.2.4 Use of non-Pt anode catalysts with HOR selectivity. To date, this concept has been reported solely by Ioroi and Yasuda. They suggested that Ir/Ti_4O_7 anodes suppress damage at the cathodes during startup/shutdown due to the high HOR activity of Ir, which is just 2.6 times lower than that of Pt, and its insufficient ORR activity, which is substantially lower than that of Pt. The reported RTA performance of the Ir/Ti_4O_7 catalyst was high and similar to that of the Pt/Ti_4O_7 + Ir black catalyst shown in Fig. 9(b).[175] The startup/shutdown durability of MEAs with an Ir/Ti_4O_7 anode and Pt/C or PtCo/C cathode is of particular interest. Although many non-Pt cathode ORR catalysts have already been reported, few non-Pt anode HOR catalysts have been described. Examples include WC and bimetallic carbides (NiWC, CoMoC, MoWC, and CoWC) supported on carbon black, as reported by the Nagai group in the late 2000s,[195–197] carbon-encapsulated Ni nanocrystals reported by Haslam *et al.* in 2011,[198] nickel-diphosphine complexes on multiwalled carbon nanotubes (MWCNTs) published by several groups since 2011,[199,200] and hafnium oxynitride thin films described by the Koel group in 2019.[201] The carbide anode catalyst series described by Nagai *et al.* suffered from low single-cell performance to display a power density that was one order of magnitude lower than that of the Pt/C anode.[195–197] This suggests that the low HOR activity changed the rate-determining step from the ORR at the cathodes to the HOR at the anodes due to the carbide anodes. Furthermore, the stability of these carbides in PEFCs remains unclear. Haslam *et al.* evaluated the HOR activity of their Ni catalysts under the atypical conditions of 0.27 V *versus* SHE in a strongly acidic medium (1.5 mol dm^{-3} H_2SO_4).[198] Metallic nickel is not ORR active, although it can readily leach out in acidic media if the protected carbon shell is absent. The HOR activity of a nickel-diphosphine
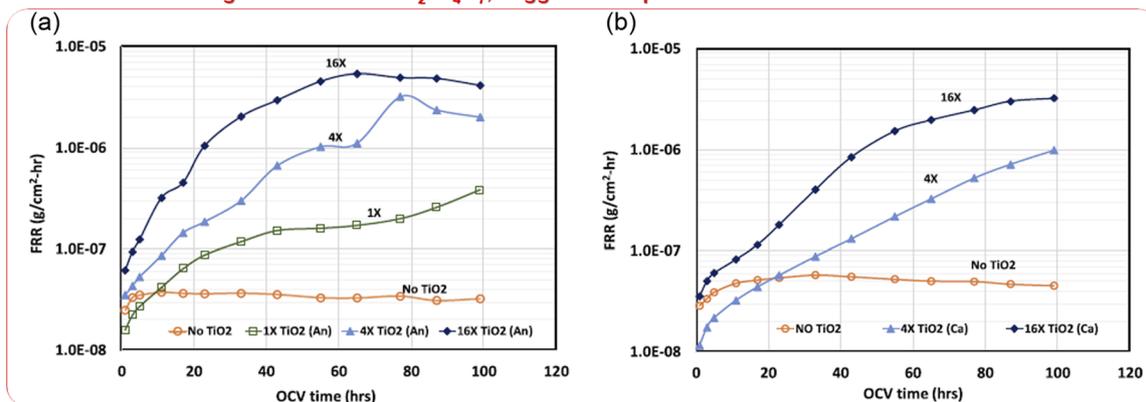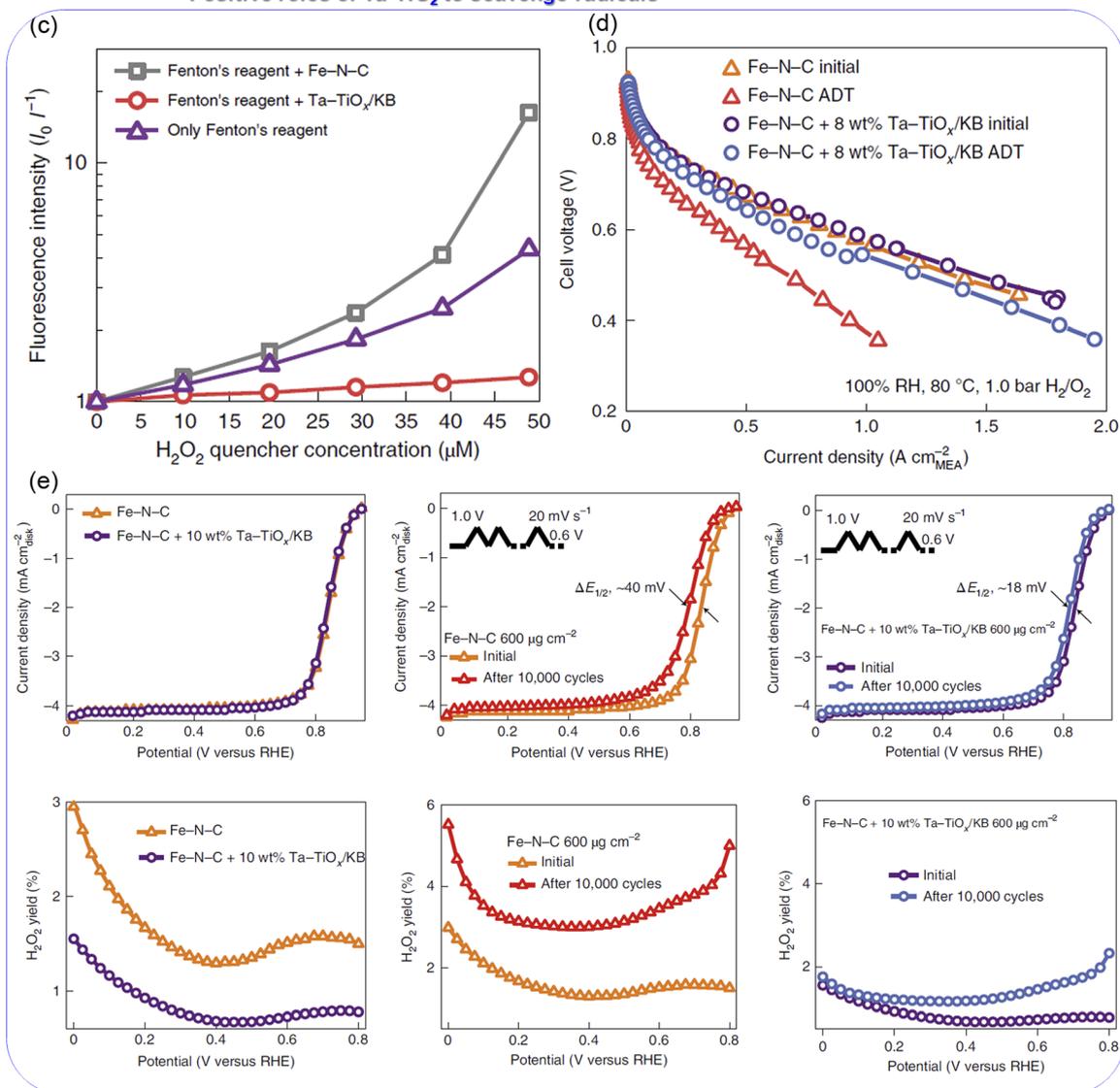
complex catalyst was evaluated under typical conditions in a common electrolyte, 0.5 mol dm^{-3} H_2SO_4.[199,200] The superior CO tolerance of MEAs compared with commercial Pt/C is another attractive point.[199] The hafnium oxynitride HOR catalysts described by the Koel group[201] have also been reported as ORR catalysts in acidic media after being supported on carbon black.[202] Although they are highly stable in acidic media, it is necessary to decrease ORR activity through precise control of the surface composition[202] and crystallinity,[203] as they are both dominant factors for the ORR activity of hafnium oxynitride catalysts. The PGM-free HOR catalysts reviewed in this paragraph rely on carbon supports to confer conductivity in the catalyst layer. However, their durability has not been evaluated in a single cell. The non-Pt, PGM catalyst, Ir/Ti_4O_7, is carbon-support-free and therefore durable against cell reversal, as experimentally confirmed in a single cell.[175] Its potential to suppress cathode degradation during startup/shutdown makes it more attractive than other non-Pt HOR catalysts, at least at this stage.

2.2.2.5 Multifunctional layer between a conventional anode catalyst layer and a GDL. Apart from the selective HOR catalyst approach, Shen *et al.* introduced a new concept, as shown in Fig. 10(e). A "hydrogen storage layer" formed from a WO_3/CNT composite was sandwiched between the Pt/C catalyst layer and GDL to form a multifunctional anode that suppresses damage at the anode and cathode during H_2 starvation and startup/shutdown, respectively. The supplied H_2 molecules pass through the hydrogen storage layer to generate protons and electrons at the Pt/C layer, some of which react with WO_3 in the storage layer to form H_xWO_3 *via* eqn (iii) in Fig. 10(e). When starved of H_2, H_xWO_3 releases protons and electrons to suppress the OER and COR at the adjacent Pt/C layer. When the anode is subjected to air contamination during startup/shutdown, H_xWO_3 reacts with O_2 in the air to form WO_3 and H_2O, *via* eqn (iv) in Fig. 10(e). The single cell with and without the multifunctional WO_3/CNT layer-inserted anode (denoted as a hybrid cell and a control cell, respectively) displays interesting results. WO_3 did not affect the initial single-cell performance, while it significantly increased the durability, as shown in Fig. 10(e). The durability against H_2 starvation was evaluated at a constant current density of 0.2 A cm^{-2} and persisted for 10 s after switching the anode gas from H_2 to N_2. The hybrid cell exhibited negligible reduction in peak power density, while the control cell lost ~47% of the initial value after two rounds of H_2 starvation tests. The hybrid cell also displayed higher durability against the original simulated acceleration cycles and startup cycles as H_xWO_3 quickly scavenged O_2 molecules in contaminated anodes. The WO_3 material cost was estimated to be <\$50 per unit for a mid-sedan-type FCV sold by Toyota (MIRAI).[192]

2.2.3 Avoidance of Ti oxides. Zhang *et al.* cautioned against the use of TiO_2 and Ti_4O_7 supports in both PEFC anodes and

(red line). For the control-cell testing (black line), one cell was used for each test. The anode and cathode Pt loading was set at 0.05 mg$_{Pt}$ cm^{-2} and 0.40 mg$_{Pt}$ cm^{-2}, respectively. The anode and cathode were supplied with fully humidified H_2 and O_2, respectively, to record cell voltage *versus* current density curves, and the single cell was maintained at 323 K. Reproduced with permission.[192] Copyright 2020, Nature Publishing Group.

18660 | *J. Mater. Chem. A*, 2024, **12**, 18636–18673

This journal is © The Royal Society of Chemistry 2024

Fig. 11 Fluoride release rate (FRR) *versus* OCV time curves of MEAs fabricated using a mixture of commercial 20% w/w Pt/C and TiO_2 at the (a) anode and (b) cathode. The Pt loading was set at a constant 0.05 mg_{Pt} cm^{-2}, while four different TiO_2 loadings, 0, 0.33, 1.32, and 5.28 μg_{TiO_2} cm^{-2}, were used, denoted as No TiO_2, 1×, 4×, and 16×, respectively. Commercial 30% PtCo/C with 0.1 mg_{Pt} cm^{-2} Pt loading was used at the cathode and anode in (a) and (b), respectively. The anode and cathode were supplied with H_2 and air, respectively, at 25% RH, and the absolute back pressure was 0.15 MPa for both electrodes. The cell temperature was set at 383 K. Reproduced with permission.[204] Copyright 2021, The Electrochemical Society. (c) Stem−Volmer plots obtained using 6-carboxy fluorescein (6CFL) dye in the radical solution containing Fenton's reagent and Fe−N−C or Ta–TiO_x/KB as a function of the H_2O_2 radical quencher concentration. (d) Cell voltage *versus* current density curves of

This journal is © The Royal Society of Chemistry 2024

J. Mater. Chem. A, 2024, **12**, 18636–18673 | **18661**

cathodes, primarily based on two types of degradation test results reported in 2021.[204] The first was an OCV test to evaluate the degradation of a 12 μm-thick PFSI membrane in MEAs with TiO_2/Ti_4O_7 catalyst layers, which was conducted with an absolute back pressure of 0.15 MPa at 383 K for 100 h. The second was a leaching test of TiO_2 in 0.05 mol dm^{-3} H_2SO_4 at 368 K, with the leached Ti ions measured using ICP analyses. The membrane thinning proceeded during the OCV tests, and the rate of released fluoride from the PFSI membrane (FRR) increased with TiO_2 loading in the anodes and cathodes, as shown in Fig. 11(a) and (b). Fluoride release was also confirmed from Ti_4O_7, and the FRR was higher when TiO_2 or Ti_4O_7 was used in the anodes compared with the cathodes. Dissolved Ti ions, which catalyze Fenton reactions similar to previously reported Fe ions,[164] were considered the source of this process through degradation of PFSI membranes by H_2O_2 radicals formed by the decomposition of byproducts during the ORR.[166] Under the conditions tested by Zhang et al., TiO_2 and Ti_4O_7 degraded the PFSI membranes,[204] thus undoubtedly decreasing cell performance. One year later, Xie et al. used carbon black-supported $Ta-TiO_2$ nanoparticles ($Ta-TiO_2$/KB) to scavenge radicals formed from Fe-based PGM-free ORR catalysts, so-called Fe/N/C or Fe–N–C.[205] $Ta-TiO_2$ was a mixture of Ta_2O_5, TaO_2, and TiO_2 phases, and captured H_2O_2 radicals to enhance the durability of Fe/N/C in both a half-cell and a single cell, as shown in Fig. 11(c)–(e). The well-known low durability of the Fe/N/C catalyst in a single cell was dramatically improved by the addition of 8% w/w $Ta-TiO_2$/KB at 353 K. The results from Zhang et al. and Xie et al. appear contradictory at first glance, in that radicals were produced by Ti oxides but captured by $Ta-TiO_2$. However, some important differences should be noted. First, the cell temperature used in the work of Zhang et al., 383 K,[204] was 30 K higher than that used by Xie et al.[205] The higher temperature could accelerate the membrane degradation significantly. Second and most importantly, the crystal structure of $Ta-TiO_2$ differs considerably from that of TiO_2. The H_2O_2 yield of Fe/N/C + $Ta-TiO_2$/KB decreased with increasing Ta : Ti atomic ratio, from 2 : 8 to 6 : 4, and then increased with further increases in the ratio to 8 : 2. At a ratio of 2 : 8, a single anatase TiO_2 phase was formed with minor rutile TaO_2 at 4 : 6. At a ratio of 6 : 4, a $Ta_2O_5/TaO_2/TiO_2$ mixture was formed, followed by a single Ta_2O_5 phase at a ratio of 8 : 2. The high Ta content in the optimized Ta : Ti ratio of 6 : 4 greatly exceeds that in the Ta-doped TiO_2 supports reviewed in Sections 2.1.1.2 and 2.2.2.2, which ranged from 1 : 9 (ref. 191) to 3 : 7.[56] The three mixed phases in the $Ta-TiO_2$ described by Xie et al. have not been reported and clearly also differ from the TiO_2 supports used by

Zhang et al.[204] Zhang et al. concluded that efforts should be directed toward corrosion-resistant oxides as alternatives to Ti oxides, without noting the exact material to be developed.[204] The results of Xie et al. on PGM-free catalysts[205] suggest the presence of stable-support alternatives to pure Ti oxides for use as Pt supports, at least at a cell temperature of 353 K.

3 Carbon-support-free non-platinum catalysts

The high loading of expensive and scarce Pt catalysts and the low durability of carbon supports are the major motivators to seek cathode materials utilizing neither Pt catalysts nor carbon supports. Conductive PGMs or their oxides can be used as carbon-support-free non-Pt catalysts, including the porous IrO_2 catalysts used by Takasu et al.,[206] although Ir is extremely scarce in nature and much more expensive than Pt.[177] This section focuses on carbon-support-free non-PGM catalysts, which may be considered the ultimate catalysts. Because of the high potential and oxidative acidic environment of PEFC cathodes, as mentioned in Section 1, only two viable non-PGM catalyst types have been reported in the last two decades. Researchers in the PGM-free catalyst community have tended to develop the so-called M/N/C catalysts, which are graphitic carbons with abundant defects doped with N and one or two metals (M), typically Fe,[207–212] Co,[213] or Mn.[214] The highest activity reported to date has been seen with Fe/N/C catalysts, although durability remains an issue, as reported in the literature.[210] The formation of carbon dioxide by the oxidation of carbon species in Fe/N/C[208,210] and Co/N/C[213] has been experimentally verified, even at potentials below 1.0 V,[208,210,213] and is regarded as one of the pivotal causes of the degradation of M/N/C catalysts. To minimize carbon oxidation, a recent standardized protocol for evaluating the activity of M/N/C catalysts has limited the upper potential to 0.925 V,[212] which is lower than that for automotive carbon-supported platinum–cobalt catalysts (1.0 V (ref. 16) or 0.95 V (ref. 17)). The equilibrium potential in eqn (4) is 0.207 V versus SHE and the reaction rate in eqn (4) is accelerated at high potentials. Thus, even when M/N/C catalysts are used, system-level measures used for protecting the carbon black of the PtCo/C catalysts (as mentioned in Section 1) remain necessary. However, the practical use of M/N/C as a cathode catalyst in FCVs has attracted skepticism from industry due to the previously described durability issues and the greater catalyst loading requirement, which leads to a thicker catalyst layer compared with conventional PtCo/C catalysts.[215,216] Another type of non-PGM catalyst, oxides/oxynitrides containing group IV

MEAs with Fe−N−C and Fe−N−C + 8% w/w Ta-TiO$_x$/KB cathodes before and after 20 voltage cycles between 0.85 V and 0.40 V (ADT). During the ADT, the cell voltage was held at 0.85 V for 5 min and 0.40 V for 55 min per unit cycle, and the cell was maintained at 353 K and supplied with H$_2$ and air at the anode and cathode, respectively. The cathode catalyst loading was set at 6.0 mg cm^{-2}. In all MEAs, the anode was commercial 46.5% w/w Pt/C with 0.2 mg$_{Pt}$ cm^{-2} Pt loading. The anode and cathode were supplied with fully humidified H$_2$ and O$_2$, and the cell temperature was set at 353 K. (e) (top) RDE voltammograms and (bottom) H$_2$O$_2$ yield versus potential curves of (left) Fe−N−C and Fe−N−C + 10% w/w Ta-TiO$_x$/KB, (center) Fe−N−C, and (right) Fe−N−C + 10% w/w Ta-TiO$_x$/KB before and after 10 000 potential cycles between 0.6 and 1.0 at 20 mV s^{-1}. The scans were performed under an O$_2$ atmosphere using a rotation speed of 900 rpm and a staircase potential step of 25 mV at intervals of 25 s in 0.5 mol dm^{-3} H$_2$SO$_4$. Reproduced with permission.[205] Copyright 2022, Nature Publishing Group.

18662 | J. Mater. Chem. A, 2024, 12, 18636–18673

This journal is © The Royal Society of Chemistry 2024

or V metals, has attracted fewer researchers in this community compared with M/N/C, owing to the moderate ORR activity and difficulty in evaluating the activity, even in a half-cell. However, this type of catalyst can eliminate the use of carbon supports, as the active sites are hosted in oxide/oxynitride, unlike M/N/C catalysts where the active sites are assumed to be M-coordinated with N atoms located at the edge of graphitic carbon supports.[207–214] Oxide-based catalysts were first reported by the Ota group in the mid-2000s. In their initial work, WC was investigated as a non-PGM catalyst because of its similar electronic structure to Pt. However, the WC was found to be unstable in acidic media and required passivation to WO_3. The WC was stabilized by adding Ta, a group V metal.[217] Since then, Ota et al. focused on binary oxides containing group IV and V metals as ORR catalysts. The chemical stability in 0.1 mol dm^{-3} H_2SO_4 solution analyzed by ICP spectroscopy revealed a small amount of leached metal from ZrO_2,[218] TiO_2,[219] N-doped ZrO_2,[220] or Ta_3N_5 with oxidized surface Ta_2O_5.[221] Later, we also reported a small Hf leaching amount in monoclinic HfO_2 and Hf_2ON_2 after 2 days of leaching tests in an identical solution.[202] These chemical stabilities are a particular benefit of this type of oxide/oxynitride catalyst. The disadvantage of this type of catalyst, however, is the difficulty in evaluating its ORR activity, as displayed in Fig. 12(a). The Ota group synthesized ZrO_2 powder catalysts via a sol–gel route, followed by annealing under a reductive atmosphere, and evaluated their ORR activity in a half-cell.[222] The four curves shown in Fig. 12(a) clearly differ from each other, even though they all originate from an identical catalyst with different catalyst layers due to mixing with different carbon black materials and different carbon black contents in order to achieve conductivity in the catalyst layer. These results indicate that the optimization of the catalyst layer structure is necessary, even for screening active oxide/oxynitride catalysts. Because the surface area and particle size of the catalysts differ and depend substantially on the route and conditions of synthesis, such optimization is necessary for every catalyst. This is a time-consuming process. Therefore, some researchers synthesized oxide/oxynitride catalysts on conductive carbon materials such as carbon black,[202,203,225,231,232] CNTs,[223,233] reduced graphene oxide,[234,235] and carbon nanocages.[236] One of the carbon-supported oxynitride catalysts, N-doped ZrO_2 on MWCNTs (N-ZrO_2/MWCNTs), exhibited a single-cell performance comparable to that of Fe/N/C, as shown by curve 1 in Fig. 12(b).[223] This finding attracted the attention of the pioneers of Fe/N/C catalysts, the Dodelet group.[237] However, the single-cell performance was not stable for 10 000 FCCJ load cycles and even at a constant $j = 0.1$ A cm^{-2}, as shown in Fig. 12(c) and (d), respectively.[223] One reason could be the oxidation of the carbon supports, making oxide/oxynitride catalysts free from carbon supports an attractive option. However, when group IV or V oxide/oxynitride catalysts were used as catalysts without carbon supports, the current was too low even in a half-cell. Indeed, until the mid-2010s, the reported geometrical current density was only at the μA cm^{-2} level in practical potential regions above 0.6 V versus RHE.[218–221,238] Although the conductivity of oxide supports for Pt particles can be enhanced by metal doping, as described in Sections 2.1.1.2

and 2.1.1.3, their conductivity is not sufficient to evaluate ORR activity without Pt. This is because the σ-value of oxide supports is in general enhanced by 2–4 order of magnitude after depositing Pt particles, as the introduction of conductive Pt enhances the σ of catalyst particles.[105] Because TiN offers an excellent σ without Pt,[149,156] we have recently focused on conductive nitride, TiN, to produce carbon-support-free, non-PGM catalysts. The first catalyst was obtained via the pyrolysis of a hydrothermally synthesized Ti_4O_7 fiber, TiF_4, and a urea precursor mixture prepared in HCl solution.[38] Unfortunately, the Ti_4O_7 fiber oxidized during the pyrolysis to form insulating rutile TiO_2, whereas TiF_4-derived TiN produced ORR active sites on the oxidized surface, of which the majority was nitrogen-substituted TiO_2, as revealed by the control experiment shown in Fig. 12(e).[224] The geometrical current density in a practical potential range (>0.6 V versus RHE) in a half-cell was three orders of magnitude higher than that of previous carbon-support-free catalysts.[218–221,238] Several control experimental results, including the one shown in Fig. 12(e), revealed that carbon residues from the urea precursor were not the source of the ORR activity or conductivity of this catalyst.[38,224] However, the conductivity was insufficient to use carbon black in the cathode catalyst layer to obtain single-cell performance, as shown by curve 2 in Fig. 12(b).[38] The ORR activity increased with N content, which substituted for O in the surface TiO_2 lattice, while the surface TiN content was simultaneously maintained below 20%.[38,224] The surface TiN was also unstable, which decreased the activity as illustrated in Fig. 12(f).[225] This is consistent with the work of Avasarala et al., in which 31.5% of surface TiN content was unstable.[147] When the TiN surface was covered with nitrogen-substituted TiO_2 layers to decrease the surface TiN content, there was no change in surface chemical states during the ORR, as revealed by post-XPS analyses.[224] An oxygen vacancy is created when two oxygen atoms in the TiO_2 lattice are substituted by two nitrogen atoms to compensate for the charge imbalance due to the nitrogen substitution. An oxygen vacancy is one possible site for the adsorption of O_2 molecules, which is the first step for the ORR, eqn (2a). Indeed, the Lyubinetsky group reported the dissociative adsorption of O_2 molecules on bridging oxygen vacancies on the (1 1 0) plane of rutile TiO_2 at room temperature using in situ scanning tunneling microscopy (STM) in 2008.[239] One of the oxygen atoms of O_2 filled one oxygen vacancy, while the other was deposited on a five-fold titanium atom next to the vacancy. Two years later, Lyubinetsky et al. presented a subsequent model on the same rutile (1 1 0) plane and used STM and DFT calculations to show that O_2 molecules adsorbed on the titanium rows, while the charge from the oxygen vacancy promoted the dissociation of O_2 molecules.[240] The dissociative adsorption of O_2 molecules on the (1 1 0) plane of rutile TiO_2 with an oxygen vacancy was also reported using STM by Wendt et al., although the proposed source of charge to promote O_2 dissociation differed.[241] These thought-provoking studies provide valuable context for the discussion of the ORR active sites on our N-TiO_2-covered TiN. The material reported in the aforementioned studies was N-free TiO_2, and STM experiments were conducted in an ultra-high-vacuum system free from protons,[239–241] which was different

This journal is © The Royal Society of Chemistry 2024

J. Mater. Chem. A, 2024, 12, 18636–18673 | 18663
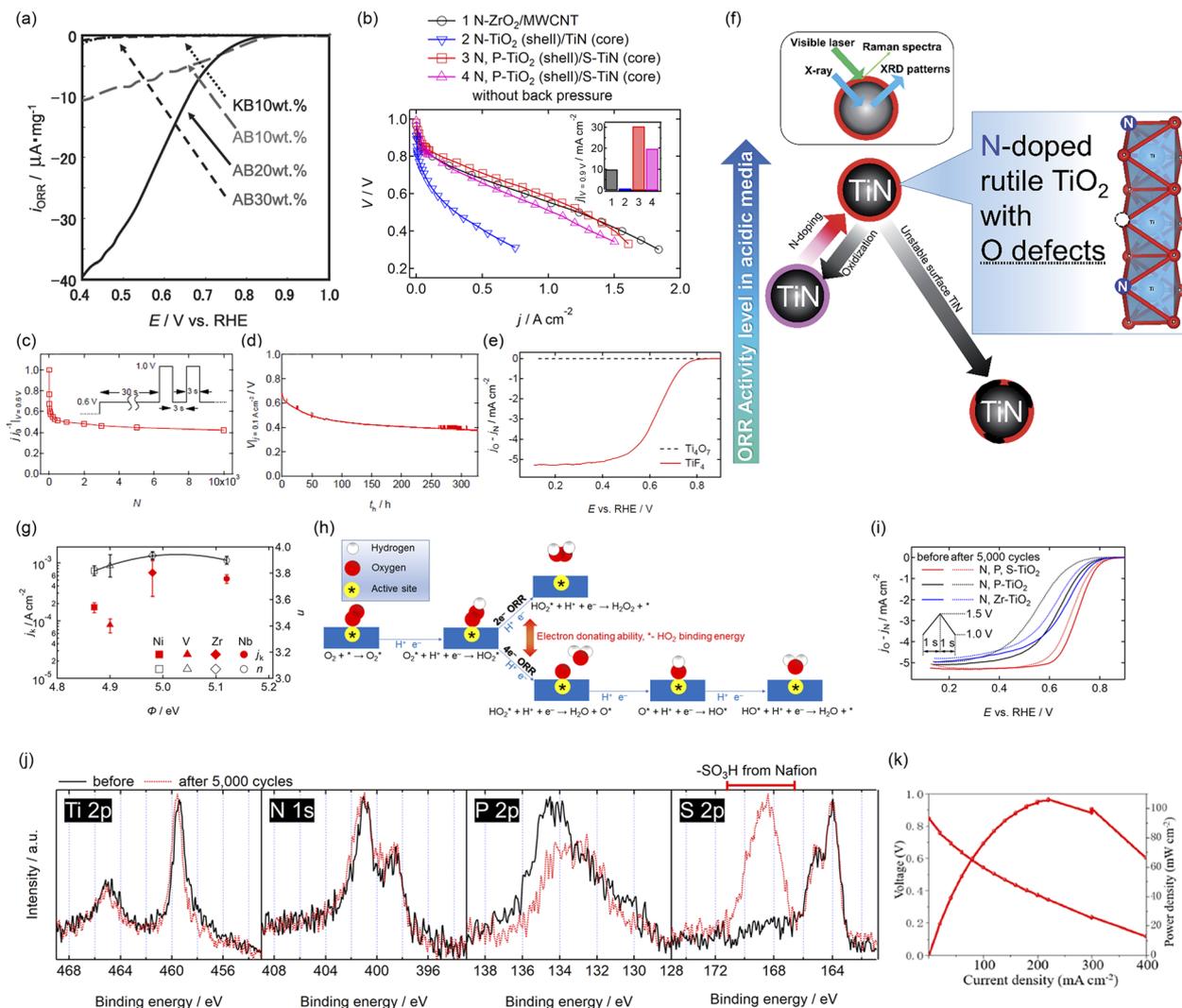
Fig. 12 (a) ORR mass activity *versus* potential ($i_{ORR} − E$) curves of a ZrO_2 catalyst for four different catalyst layers in 0.1 mol dm^{-3} H_2SO_4 without rotation. The catalyst layers were formed by mixing the ZrO_2 catalyst with two different carbon black materials, Ketjen Black EC300J (KB) or acetylene black (AB). The mass fraction of KB was set constant at 10% w/w, whereas that of AB was set at 10, 20, and 30% w/w. Reproduced with permission.[222] Copyright 2011, The Electrochemical Society of Japan. (b) $V−j$ curves of MEAs for three different catalysts at the cathode, (1) N-ZrO_2/MWCNT, (2) N-TiO_2 (shell)/TiN (core), and (3) N, P-TiO_2 (shell)/S-TiN (core) at 353 K. The cathode catalyst loadings, m, were 10, 4.7, and 5.8 mg cm^{-2}, respectively, for MEAs 1, 2, and 3. In all MEAs, the anode was commercial 46% w/w Pt/C with 0.3 mg$_{Pt}$ cm^{-2} Pt loading. The anode and cathode were supplied with fully humidified H_2 with 0.2 MPa (gauge) and O_2 with 0.3 MPa (gauge) back pressures, respectively. MEA 3 was also operated without back pressure at the anode and cathode, and is labeled as 4. The inset shows j at $V = 0.9$ V from the four curves. Reproduced with permission.[38,223] Copyright 2016, Elsevier, Copyright 2017, American Chemical Society. (c) A normalized j at $V = 0.6$ V *versus* FCCJ load cycle number ($j j_0^{-1}|_{V=0.6 V} − N$) curve and (d) a cell voltage *versus* time held at 0.1 A cm^{-2} ($V|_{j=0.1 A cm^2} − t_h$) curves of MEAs with the N-ZrO_2/MWCNT cathode catalyst. m was 8.3 and 8.9 mg cm^{-2} for (c) and (d), respectively. Reproduced with permission.[223] Copyright 2017, American Chemical Society. (e) RDE voltammograms of two N-TiO_2 catalysts synthesized by mixing urea and one of the two titanium sources, Ti_4O_7 and TiF_4, in 1.0 mol dm^{-3} HCl solution, followed by pyrolysis at 1123 K. The scans were performed under N_2 and O_2 atmospheres, with a rotation speed of 1500 rpm and a scan rate of −5 mV s^{-1} (cathodic) in 0.1 mol dm^{-3} H_2SO_4. Reproduced with permission.[224] Copyright 2018, American Chemical Society. (f) A schematic image of N-TiO_2 catalysts and the ORR active site. Reproduced with permission.[225] Copyright 2016, Royal Society of Chemistry. (g) Kinetic current density and number of electrons transferred per unit O_2 molecule *versus* the work function curves ($j_k − \Phi$ and $n − \Phi$ curves, respectively) derived from the RDE voltammograms of four N, M-TiO_2/S-TiN catalysts, where M = Zr, Nb, Ni, and V. (h) Two reaction pathways for the ORR on conventional catalysts. Reproduced with permission.[226] Copyright 2022, Royal Society of Chemistry. (i) RDE voltammograms of N, P-TiO_2/S-TiN, N, Zr-TiO_2/S-TiN, and N, P, S-TiO_2/S-TiN catalysts before (solid curves) and after (dashed curves) 5000 FCCJ startup/shutdown cycles; the protocol is shown in the inset. Reproduced with permission.[227–229] Copyright 2020, American Chemical Society, Copyright 2022, American Chemical Society, Copyright 2024, Royal Society of Chemistry. (j) X-ray photoelectron spectra of the N, P, S-TiO_2/S-TiN catalyst before (solid curves) and after (dashed curves) 5000 FCCJ startup/shutdown cycles. The N, P, S-TiO_2/S-TiN catalyst after 5000 cycles contains Nafion PFSI in the catalyst layer. Reproduced with permission.[229] Copyright 2024, Royal Society of Chemistry. (k) Cell voltage and power density *versus* current density curves of an MEA fabricated using $Ti_{0.8}Co_{0.2}N$ at $m = 4$ mg cm^{-2} and commercial 60% w/w Pt/C catalysts at 0.1 mg$_{Pt}$ cm^{-2} in the cathode and anode, respectively, at 343 K. The anode and cathode were supplied with fully humidified H_2 and air, respectively. Reproduced with permission.[230] Copyright 2018, American Chemical Society.

18664 | *J. Mater. Chem. A*, 2024, **12**, 18636–18673

This journal is © The Royal Society of Chemistry 2024

from the acidic media where the ORR activity of N-TiO$_2$ was evaluated. It is difficult to conduct similar STM experiments under realistic PEFC conditions in the presence of acidic PFSI electrolytes. Nonetheless, oxygen vacancies in rutile N-TiO$_2$ were revealed to produce ORR active sites through a low-temperature annealing process combined with Raman, XPS, and electrochemical analyses.[242] Although the bulk of this catalyst was the metallic character of the conductive TiN, the surface TiO$_2$ layers should have much lower conductivity than the bulk. We recently doped cationic phosphorous onto surface N-TiO$_2$ layers to enhance surface conductivity by introducing an electron donor, P^{5+}.[227,243] P^{5+} was doped into the bulk and surface to more than double the ORR mass activity in a half-cell without changing the number of oxygen vacancies in surface rutile TiO$_2$ layers on S-TiN (S is from the TiOSO$_4$ precursor) formed by N-doping. The enhanced mass activity was also greater than that of N-ZrO$_2$/MWCNT.[243] The MEA with an N, P-TiO$_2$/S-TiN cathode exhibited a single-cell performance significantly improved compared with that of P-free N-TiO$_2$/TiN, and even higher than that of the previous best carbon-supported oxynitride catalyst, N-ZrO$_2$/MWCNT at $V \geq 0.6$ V (the operating range of FCVs[16,17]), as shown by curve 3 in Fig. 12(b). Furthermore, the j at $V = 0.9$ V from N, P-TiO$_2$/S-TiN without back pressure exceeded that of N-ZrO$_2$/MWCNT with high back pressures, as shown in the inset. These results could be due to the synergetic effects of (1) the higher ORR activity of N, P-TiO$_2$/S-TiN than the other two catalysts and (2) improved mass-transport properties owing to the smaller particle size of N, P-TiO$_2$/S-TiN than N-TiO$_2$/TiN, as the aggregation during high-temperature synthesis was suppressed by P-doping.[243] Nonetheless, all V–j curves were obtained after mixing carbon black with the catalyst particles to induce conductivity in the catalyst layer. The σ of N, P-TiO$_2$/S-TiN is sufficient without using carbon black in a half-cell; however, it is insufficient in a thicker catalyst layer in a single cell, which produces a current density three orders of magnitude higher than that of the catalyst layer in a half-cell.

On the N-TiO$_2$/TiN and N, P-TiO$_2$/S-TiN catalysts, the ORR proceeded *via* two- (2e$^-$) and four-electron (4e$^-$) pathways, described by eqn (6) and (2), respectively.[224,227,243] We recently revealed that ORR selectivity can be enhanced in the 4e$^-$ pathway by tuning the work function, Φ, of N-TiO$_2$/S-TiN *via* metal doping, as shown in Fig. 12(g).[226,228] Φ is the difference in the potential energy of an electron between the vacuum and Fermi levels, which corresponds to the minimum energy required to extract an electron from a solid surface. Therefore, 4e$^-$ selectivity (*i.e.*, the number of electrons transferred per unit O$_2$ molecule, n) increases with decreasing magnitude of Φ. The 2e$^-$ ORR in acidic media has been assumed to proceed *via* the following three elementary steps:[143,144]

$$O_2 + * \rightarrow O_2* \qquad (6a)$$

$$O_2* + H^+ + e^- \rightarrow HO_2* \qquad (6b)$$

$$HO_2* + H^+ + e^- \rightarrow H_2O_2 + * \qquad (6c)$$
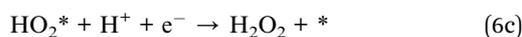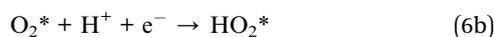
In the 4e$^-$ and 2e$^-$ ORR processes shown in Fig. 12(h), a peroxy-intermediate, HO$_2$, is produced (eqn (2b) and (6b)). The electron-donating ability from the active site expressed by * and the strength of binding between HO$_2$ and * are key factors in determining n. When the magnitude of Φ is too small, the catalyst-HO$_2$ intermediate interaction becomes stronger and ultimately slows the ORR process. Besides this interaction between the HO$_2$ intermediate and the catalyst, the smaller the Φ, the more negative the potential at which the ORR proceeds.[244] This could be one reason for the decrease in ORR selectivity with Φ. The Φ was decreased (*i.e.*, the Fermi level of TiN was upshifted by doping foreign metals) in the following order: Nb > Zr > V > Ni. Either Zr or Nb was close to optimum tuning of the Fermi level to donate electrons to O$_2$ molecules but not to bind strongly with the reaction intermediate at the potential where the ORR proceeds. Rutile TiO$_2$ has been investigated as a catalyst for the OER, which is the reverse reaction of the ORR. García-Mota *et al.* investigated the binding energy of HO$_2$ and * of the (1 1 0) plane on various metal-doped rutile TiO$_2$ catalysts using first principles DFT calculations.[245] Although zirconium was not included in their study, niobium, nickel and vanadium were investigated as dopants. The binding energy increased in the order of Nb < V < Ni.[245] This trend is the reverse of n shown in Fig. 12(g), suggesting that strong *–HO$_2$ interactions inhibited the breaking of O–O bonds in the HO$_2$ intermediate to favor the 2e$^-$ ORR, to produce H$_2$O$_2$.

As these TiN-based catalysts are free from carbon supports, a high durability against startup/shutdown cycles is expected. Fig. 12(i) shows the RDE voltammograms of these catalysts before and after 5000 FCCJ startup/shutdown cycles. Unfortunately, N, P-TiO$_2$/S-TiN catalysts significantly decrease the ORR activity measured by a half-wave potential ($E_{1/2}$, *i.e.*, the potential at which half of the limiting current density is obtained) by 0.08 V after the 5000 cycles. During the cycles, both N and P atoms were removed from the surface, as revealed by XPS analyses.[227] The N, Zr-codoped TiO$_2$/S-TiN with an optimized composition was more durable against the 5000 FCCJ startup/shutdown cycles, decreasing the $\Delta E_{1/2}$ by half that of N, P-TiO$_2$/S-TiN (0.04 V), owing to the high selectivity toward the 4e$^-$ ORR.[228] We recently enhanced the startup/shutdown durability further using a new catalyst, N, P, S-tridoped TiO$_2$ supported on S-TiN, to successfully reduce $\Delta E_{1/2}$ to 0.02 V without diminishing the limiting current plateau. This result is among the highest of any PGM-free catalysts. Anatase and rutile TiO$_2$ hetero-phase junctions formed in the N, P, S-TiO$_2$/S-TiN catalyst promoted ORR activity, and the surface anionic dopants were not removed during the 5000 cycles to maintain activity, as shown in Fig. 12(j).[229] The stabilization of the cationic P^{5+} dopant, whose binding energy is 134–135 eV, is the remaining challenge in terms of diminishing $\Delta E_{1/2}$. Although this non-PGM catalyst type is rarely studied by this community, other researchers have recently focused on TiN. For example, Tian *et al.* synthesized Ti$_{0.8}$Co$_{0.2}$N catalysts *via* a combination of a solvothermal route and NH$_3$ annealing. The catalysts were evaluated in a single-cell cathode without adding carbon black to the catalyst layer, as shown in Fig. 12(k).[230] Control

This journal is © The Royal Society of Chemistry 2024

J. Mater. Chem. A, 2024, **12**, 18636–18673 | **18665**

experiments to evaluate the contribution of possible Co/N/C species in catalysts and the durability of the carbon black-free catalyst layers will be of interest.

4 Possibility of carbon-support-free catalyst use in future vehicles

In order to achieve conductivity in the catalyst layer, carbon-support-free non-PGM catalysts are limited to TiN-based cathode catalysts. The low current density of carbon support-free oxide/oxynitride catalysts arising from the low conductivity has been improved using TiN to the order of mA cm^{-2} in a half-cell; however, the enhanced conductivity is still insufficient to add carbon black in a single-cell catalyst layer in most cases. The durability in a single cell has therefore seldom been evaluated, and it is therefore too early to discuss the possibility of using this approach in future FCVs.

Carbon-support-free Pt-based catalysts have been developed extensively in PEFC anodes and cathodes in the last two decades, although they retain several challenges with respect to their use in FCVs.

(1) Pt loading

As mentioned in Section 1, the target of ~6 g_{PGM} per midsedan FCV[9] is comparable to the amount of PGMs per gasoline-fueled LDV,[11] and needs to be achieved to make PEFC-powered passenger vehicles affordable and widespread. The target has been set with 0.0625 g_{PGM} kW^{-1} PGM usage per unit power and 1 W cm^{-2} power density, which correspond to 0.0125 and 0.05 mg_{PGM} cm^{-2} PGM loading at the anode and cathode catalyst layers, respectively.[9] Considering the currently available PtCo/C cathode and Pt/C anode catalysts, the target PGM loading values can be assumed to be equal to the Pt loading. The Pt loading used in Pt/non-carbon cathode catalyst layers has been much higher than the target of 0.05 mg_{Pt} cm^{-2} in general, as listed in Table 1 and seen in the captions for Fig. 4–11. Rare exceptions include Pt/Ta-SnO$_{2-\delta}$ and Pt/Nb-SnO$_{2-\delta}$ cathode catalysts with a Pt loading of 0.06 ± 0.002 mg_{Pt} cm^{-2},[105] which is close to the target value. Although the advantage of these Pt/oxide catalysts in terms of durability should be taken into account in the comparison with the currently available PtCo/C catalysts, a decrease in Pt loading to the target level without decreasing cell performance is needed for widespread use in FCVs. It will be highly challenging for Pt/non-carbon catalysts, as Pt nanoparticles enhance the conductivity of non-carbons by 2–4 orders of magnitude[105] to exceed the proton conductivity of PFSI, and thus prevent electron transport from being the rate-determining step. As illustrated in Fig. 9(c), when it is necessary to have Pt particles that are connected or in close proximity to each other to improve conductivity in the catalyst layer, lowering the Pt content (i.e., reducing Pt loading) is difficult without compromising cell performance. Indeed, 0.1 mg_{Pt} cm^{-2} Pt loading was necessary for the Pt/Ti$_4$O$_7$ anode, and the cell performance decreased significantly when the anode Pt loading was decreased to 0.05 mg_{Pt} cm^{-2}.[37] This indicates that electron transport restricted the cell performance of MEAs with the Pt/Ti$_4$O$_7$ anode, despite the faster HOR kinetics on Pt than

the ORR counterparts. When standard 47% w/w Pt/C catalysts were used in anode catalyst layers and the anode Pt loading was decreased from 0.40 to 0.05 mg_{Pt} cm^{-2}, the drop in the cell voltage at a current density of 1 A cm^{-2} was negligible, in the order of 10 mV.[246] The effect of anode Pt loading on the cell performance of MEAs with a Pt/Ti$_4$O$_7$ (ref. 37) anode (significant) and Pt/C[246] anode (negligible) clearly differed, as mentioned above, when the loading was decreased to 0.05 mg_{Pt} cm^{-2}, which is four times higher than the target value. The σ-value of some non-carbon supports does not restrict the single-cell performance when they are used as supports for Pt catalysts to levels similar to that of Pt/C, at least when the Pt loading exceeded the target value. Further increases in the σ of non-carbon supports to the order of 10 S cm^{-1} in any P range shown in Fig. 4(k) by, for example, controlling the morphology[104] will be necessary. It will be particularly important for use as cathode catalyst supports owing to the slow ORR kinetics and thicker catalyst layer compared with anode counterparts. Theoretically, less than 0.01 mg_{Pt} cm^{-2} cathode Pt loading with power density maintained above 1 W cm^{-2} is expected by optimizing the O$_2$ and proton transport properties when electron transport across the catalyst layer is sufficiently fast.[247] Furthermore, the control of the Pt mass fraction in Pt/non-carbon catalysts will be of particular importance. In most catalysts reviewed in this paper, this was set at around 20% w/w Pt/non-carbon. A support particle size of ~100 nm, which is smaller than that of most non-carbon supports, will be necessary to increase the Pt mass fraction beyond 20% w/w without an increased Pt nanoparticle size penalty. In addition, a lower Pt mass fraction in Pt/non-carbon catalysts leads to a higher catalyst mass and thicker catalyst layer compared with conventional Pt/C. These properties are unsuitable for use in vehicles. In future studies, cell performance with Pt/non-carbon catalysts at (i) target low Pt loading (0.05 and 0.0125 mg_{Pt} cm^{-2} at the cathode and anode, respectively) and (ii) a high Pt mass fraction (above 40% w/w) will attract significant attention. Although unsupported Pt-alloy anode[248] and cathode[249] catalysts are beyond the scope of this paper, the evaluation of their performance at (i) will also be of interest.

(2) Metal leaching

To date, no complete non-carbon supports which do not leach in the catalyst layer have been reported. Metals used in non-carbon supports leach as cations to some extent when their chemical stability is evaluated, as reviewed in Section 2. The leached cations exchange H$^+$ in the sulfate groups in PFSI catalyst layers and membranes to decrease the proton conductivity or catalyze the Fenton reaction in some cases. Cation-doped SnO$_2$ is one of the most widely studied non-carbon supports, where the aim of doping was mainly to increase σ. Substantial leaching of the doped cations and Sn at potentials lower than 0.4 V (ref. 103) and higher than 1.5 V has also been reported.[51] These systems are therefore more suited for use in cathodes than anodes due to their higher stability in the cathode potential window.[103,106] Similarly, the selection of the potential window is necessary when considering other non-carbon supports that are less studied than SnO$_2$-based materials. Another widely studied non-carbon support, TiO$_2$ and

Ti_4O_7, also leaches, while recent results on the radical scavenging properties of Ta-TiO$_x$ reported by Xie et al.[205] suggest the potential to suppress leaching by Ta-doping or controlling the crystal structure. Doping Ta into effective Ti_4O_7-based RTAs with an evaluation of the amount of leaching will be of interest.

(3) Scalability

The difficulty in scaling up the batch size of non-carbon supports has seldom been reported, even though many researchers face this issue, even in a laboratory. The solid-state reaction route is a simple, easy, and well-known method suited to the mass production of inorganic supports, although most studies reviewed in this paper utilized other routes to increase the surface area. Hydrothermal routes are also suited for mass production without increasing the synthesis temperature to the level of a solid-state reaction route and have been used to synthesize non-carbon supports for PEFCs; however, the batch size is frequently not reported. Examples of studies reporting the batch size include 10 g of $Sn_{0.96}Sb_{0.04}O_{2-\delta}$ particle supports synthesized with a flame combustion route,[102] 2 g of Ti_4O_7 synthesized via a carbothermal reduction reaction route,[36] and 2 g of $(Ti_{0.91}V_{0.09})_4O_7$ produced by a solid-state reaction.[64] There should be considerable interest both in the batch size itself and difficulties for increasing it. For example, vanadium doping increased the batch size of Ti_4O_7, although excessive amounts of vanadium dopants formed a Ti_2O_3 phase rather than the target Ti_4O_7.[64]

(4) Carbon-free microporous layers and GDLs

As shown by Ioroi's early work on Pt/Ti_4O_7 cathodes[35] and Ramani's work on Pt/TRO cathodes,[14] conventional carbon-based microporous layers on GDLs and/or GDLs themselves are oxidized at high potential, complicating the evaluation of Pt/non-carbon catalyst durability. Although carbon papers have been used as GDLs in the latest FCVs produced by multiple companies,[121,250] the use of carbon-free GDLs should be the focus of research in academia to help understand the phenomena in Pt/non-carbon catalyst layers at high potentials.

For carbon-supported Pt[251–253] and X–Pt core–shell (X = Ni, Cu, Pd, Co, Ag, Au)[254] nanoparticle catalysts, theoretical modeling has been performed to clarify their degradation mechanisms. Particularly, the diameter of Pt in Pt/C[252] and the thickness of the Pt shell in X–Pt/C[254] significantly affected the dissolution rate of Pt and the resulting ECSA after ADTs. Similar theoretical modeling studies on Pt/non-carbon or Pt-alloy/non-carbon catalysts with various degrees of SMSIs and various amounts of leached metals from the supports are expected.

5 Conclusions

Carbon-support-free Pt/Pt-alloy and non-Pt catalysts for use in PEFCs are reviewed in this paper. Particular attention is placed on automotive PEFCs, where lower Pt loading, lower catalyst mass, and a lower cost of materials and operations are required compared with currently available Pt/C anode and PtCo/C cathode catalysts to allow their widespread use in LDVs/MDVs/HDVs. Binary and nonbinary oxides show potential as alternative stable supports to state-of-the-art carbon black, reducing the system cost to protect carbon black from corrosion

in anodes and cathodes. Their conductivity, more than six orders of magnitude lower than that of carbon black, has been increased by different routes including foreign metal doping and the formation of suboxides. Binary and ternary nitrides have also been developed, although their variety is limited compared with oxide supports for TiN-based materials, owing to the poorer particle conductivity and stability of other nitrides.

Over the last two decades, more effort has been devoted to developing cathode supports than their anode counterparts. Various non-carbon supports have been developed and they display a single-cell performance similar to that of commercial Pt/C catalysts under some conditions. Examples of Pt-based catalysts that have shown this performance and even higher durability at the cathode during startup/shutdown cycles include Magnèli-phase Ti_4O_7, metal-doped TiO_2, and metal-doped-SnO_2-supported catalysts. Pt/Ti_4O_7 also exhibited higher durability against cell reversal at the anode than Pt/C. The excellent activity and durability of these systems are mostly ascribed to SMSIs between Pt particles and metals in the oxide supports, although the mechanism around the d-band center is still under debate. Cathode carbon corrosion during the startup/shutdown is caused by the ORR at the Pt-catalyst anode and has been suppressed by a new approach within the last decade. Anode ORR catalysis has been suppressed by developing HOR-selective catalysts, leveling off the conductivity of supports by using contaminated O_2 molecules, and by using a multifunctional hydrogen reservoir layer to capture contaminated O_2. Carbon-support-free non-PGM catalysts have been developed only for the cathode sides, where a larger PGM loading is needed compared with the anode counterparts. Such ultimate catalysts are attractive but limited to TiN-based materials owing to the conductivity of other candidates. Oxide materials can be used as supports for Pt particles as the conductivity of the Pt/oxide catalyst is conferred by the Pt particles, whereas the conductivity of the supports themselves is too low to evaluate ORR activity, even in a half-cell. Few single-cell results with TiN-based non-PGM cathodes have been reported to date, and the catalysts were mixed with carbon black in the catalyst layer to obtain more than 1 A cm^{-2} current density. This is because conductivity is still insufficient for use in a single cell as the current density is three orders of magnitude larger than that in a half-cell. Recent N, P, S-tridoped TiO_2 catalysts supported on S-doped TiN are durable against startup/shutdown cycles in a half-cell, although conductivity issues still need to be overcome.

Remaining challenges for the use of carbon-support-free Pt catalysts in future FCVs include reduction in Pt loading, suppression of leaching metals from supports, and scalability. Even state-of-the-art Pt/oxide catalysts rely on the conductivity of Pt particles, and thus decreasing the MEA Pt loading to the target set for the widespread use of FCVs (0.0625 mg$_{Pt}$ cm^{-2}, corresponding to 0.0125 and 0.05 mg$_{Pt}$ cm^{-2} at the anode and cathode, respectively) is highly challenging at this stage. When the pressure applied to supports is <10 MPa, the conductivity required for non-carbon supports to meet the stringent Pt loading target will be similar to that of currently available carbon black (of the order of 10 S cm^{-1}). Metal leaching from supports seriously degrades cell performance via a decrease in proton

This journal is © The Royal Society of Chemistry 2024

J. Mater. Chem. A, 2024, 12, 18636–18673 | 18667

conductivity, with ion exchange of sulfonate groups in PFSI catalyst layers and PFSI membranes, and even the production of radicals. Recently developed Ta-TiO$_x$ radical scavengers are potential supports to overcome the issue. The scalability of non-carbon supports, which has seldom been reported in the literature, is particularly important for use in FCVs, and further description of this aspect is needed. Pioneering studies have revealed that carbon in microporous layers on GDLs and that in GDLs are oxidized at high potential to form CO$_2$. Non-carbon GDLs are required to precisely evaluate the tolerance of non-carbon supports in catalyst layers against high potential. Overall, the development of non-carbon materials after factoring these challenges/issues may position these materials at a level close to that needed for practical use in FCVs.

Data availability

No primary research results, software or code has been included in this paper.

Author contributions

Mitsuharu Chisaka: conceptualization, writing – original draft, writing – review & editing, and funding acquisition.

Conflicts of interest

The author declares no competing financial interests.

Acknowledgements

References

1 U. S. EPA, *Sources of Greenhouse Gas Emissions*, https://www.epa.gov/ghgemissions/sources-greenhouse-gas-emissions, last accessed on Apr. 16, 2024.

2 K. L. Fleming, A. L. Brown, L. Fulton and M. Miller, *Curr. Sustainable/Renewable Energy Rep.*, 2021, **8**, 180.

3 W. Jia, Z. Jiang, Q. Wang, B. Xu and M. Xiao, *Transport Policy*, 2023, **135**, 21.

4 https://ww2.arb.ca.gov/news/california-approves-groundbreaking-regulation-accelerates-deployment-heavy-duty-zevs-protect, last accessed on Apr. 16, 2024.

5 https://ww2.arb.ca.gov/news/california-transitioning-all-electric-public-bus-fleet-2040, last accessed on Apr. 16, 2024.

6 O. Gröger, H. A. Gasteiger and J. P. Suchsland, *J. Electrochem. Soc.*, 2015, **162**, A2605.

7 D. A. Cullen, K. C. Neyerlin, R. K. Ahluwalia, R. Mukundan, K. L. More, R. L. Borup, A. Z. Weber, D. J. Myers and A. Kusoglu, *Nat. Energy*, 2021, **6**, 462.

8 T. Nakamichi, *Nikkei Electron.*, 2022, **6**, 73.

9 A. Kongkanand and M. F. Mathias, *J. Phys. Chem. Lett.*, 2016, **7**, 1127.

10 M. M. Whiston, I. L. Azevedo, S. Litster, K. S. Whitefoot, C. Samaras and J. F. Whitacre, *Proc. Natl. Acad. Sci. U. S. A.*, 2019, **116**, 4899.

11 U.S. Department of Energy and Office of Energy Efficiency and Renewable Energy, *Program Record 16006, Platinum Group Metals (P.G.M.) for light-Duty vehicles*, https://www.hydrogen.energy.gov/pdfs/16006_pgm_light_duty_vehicles.pdf, last accessed on Apr. 16, 2024.

12 C. A. Reiser, L. Bregoli, T. W. Patterson, J. S. Yi, J. D. Yang, M. L. Perry and T. D. Jarvi, *Electrochem. Solid State Lett.*, 2005, **8**, A273.

13 N. Linse, G. G. Scherer, A. Wokaun and L. Gubler, *J. Power Sources*, 2012, **219**, 240.

14 J. Parrondo, T. Han, E. Niangar, C. Wang, N. Dale, K. Adjemian and V. Ramani, *Proc. Natl. Acad. Sci. U. S. A.*, 2014, **111**, 45.

15 U. Eberle, B. Müller and R. von Helmolt, *Energy Environ. Sci.*, 2012, **5**, 8780.

16 A. Ohma, K. Shinohara, A. Iiyama, T. Yoshida and A. Daimaru, *ECS Trans.*, 2011, **41**, 775.

17 U.S. Department of Energy and Hydrogen and Fuel Cell Technology Office, *Fuel Cell Technologies Office Multi-year Research, Development, and Demonstration Plan*, updated in, 2016, https://www.energy.gov/sites/prod/files/2016/10/f33/fcto_myrdd_fuel_cells.pdf, last accessed on Apr. 16, 2024.

18 C. Song, Y. Tang, J. L. Zhang, J. Zhang, H. Wang, J. Shen, S. McDermid, J. Li and P. Kozak, *Electrochim. Acta*, 2007, **52**, 2552.

19 A. Taniguchi, T. Akita, K. Yasuda and Y. Miyazaki, *J. Power Sources*, 2004, **130**, 42.

20 S. D. Knights, K. M. Colbow, J. St-Pierre and D. P. Wilkinson, *J. Power Sources*, 2004, **127**, 127.

21 K. H. Lim, W. H. Lee, Y. Jeong and H. Kim, *J. Electrochem. Soc.*, 2017, **164**, F1580.

22 W. R. R. Baumgartner, E. Wallnöfer, T. Schaffer, V. Hacker, V. Peinecke and P. Prenninger, *ECS Trans.*, 2006, **3**, 811.

23 C. W. Roh, H. E. Kim, J. Choi, J. Lim and H. Lee, *J. Power Sources*, 2019, **443**, 227270.

24 W. Lü, Z. Liu, C. Wang, Z. Mao and M. Zhang, *Int. J. Energy Res.*, 2011, **35**, 24.

25 T. Arai, O. Takashi, K. Amemiya and T. Takahashi, *SAE Int. J. Alt. Power*, 2017, **6**, 145.

26 K. Sasaki, F. Takasaki, Z. Noda, S. Hayashi, Y. Shiratori and K. Ito, *ECS Trans.*, 2010, **33**, 473.

27 T. Ioroi, Z. Siroma, S. Yamazaki and K. Yasuda, *Adv. Energy Mater.*, 2019, **9**, 1801284.

18668 | *J. Mater. Chem. A*, 2024, **12**, 18636–18673

This journal is © The Royal Society of Chemistry 2024

28 S. J. Percival, J. E. Dick and A. J. Bard, *Anal. Chem.*, 2017, **89**, 3087.

29 M. Inoue, A. Nakazawa and M. Umeda, *J. Power Sources*, 2011, **196**, 4579; Y. Sugawara, T. Okayasu, A. P. Yadav, A. Nishikata and T. Tsuru, *J. Electrochem. Soc.*, 2012, **159**, F779.

30 Z. Wang, Y. R. Zheng, I. Chorkendorff and J. K. Nørskov, *ACS Energy Lett.*, 2020, **5**, 2905.

31 H. Lv, N. Cheng, T. Peng, M. Pan and S. Mu, *J. Mater. Chem.*, 2012, **22**, 1135.

32 Y. Li, S. Song, H. Kim, K. Nomoto, H. Kim, X. Sun, S. Hori, K. Suzuki, N. Matsui, M. Hirayama, T. Mizoguchi, T. Saito, T. Kamiyama and R. Kanno, *Science*, 2023, **381**, 50.

33 F. C. Walsh and R. G. A. Wills, *Electrochim. Acta*, 2010, **55**, 6342.

34 T. Ioroi, Z. Siroma, N. Fujiwara, S. Yamazaki and K. Yasuda, *Electrochem. Commun.*, 2005, **7**, 183.

35 T. Ioroi, H. Senoh, S. Yamazaki, Z. Siroma, N. Fujiwara and K. Yasuda, *J. Electrochem. Soc.*, 2008, **155**, B321.

36 M. Chisaka, W. Nagano, B. Delgertsetseg and T. Takeguchi, *Chem. Commun.*, 2021, **57**, 12772.

37 Z. Li, Y. Mu, Q. Zhang, H. Huang, X. Wei, L. Yang, G. Wang, T. Zhao, G. Wu and L. Zeng, *Energy Environ. Sci.*, 2024, **17**, 1580.

38 M. Chisaka, Y. Ando, Y. Yamamoto and N. Itagaki, *Electrochim. Acta*, 2016, **214**, 165.

39 T. Ioroi, T. Akita, S. Yamazaki, Z. Siroma, N. Fujiwara and K. Yasuda, *J. Electrochem. Soc.*, 2011, **158**, C329.

40 S. Andersson and A. Magnéli, *Naturwissenschaften*, 1956, **43**, 495.

41 R. F. Bartholomew and D. R. Frankl, *Phys. Rev.*, 1969, **187**, 828.

42 F. Cardarelli, in *Properties of Pure Ceramics in Materials Handbook: A Concise Desktop Reference*, ed. F. Cardarelli, Springer-Verlag, London, 2nd edn, 2008, ch. 10, p. 660–667.

43 T. Ioroi, H. Kageyama, T. Akita and K. Yasuda, *Phys. Chem. Chem. Phys.*, 2010, **12**, 7529.

44 K. Senevirathne, R. Hui, S. Campbell, S. Ye and J. Zhang, *Electrochim. Acta*, 2012, **59**, 538.

45 C. Yao, F. Li, X. Li and D. Xia, *J. Mater. Chem.*, 2012, **22**, 16560.

46 S. J. Tauster, S. C. Fung and R. L. Garten, *J. Am. Chem. Soc.*, 1978, **100**, 170.

47 F. Dong, Y. Liu, Z. Lv, C. Wang, W. Yang and B. Wang, *J. Mater. Chem. A*, 2023, **11**, 23106.

48 R. T. K. Baker, E. B. Prestridge and R. L. Garten, *J. Catal.*, 1979, **56**, 390.

49 R. T. K. Baker, E. B. Prestridge and R. L. Garten, *J. Catal.*, 1979, **59**, 293.

50 A. D. Duma, Y. C. Wu, W. N. Su, C. J. Pan, M. C. Tsai, H. M. Chen, J. F. Lee, H. S. Sheu, V. T. T. Ho and B. J. Hwang, *ChemCatChem*, 2018, **10**, 1155.

51 I. Jiménez-Morales, F. Haidar, S. Cavaliere, D. Jones and J. Rozière, *ACS Catal.*, 2020, **10**, 10399.

52 C. J. Pan, M. C. Tsai, W. N. Su, J. Rick, N. G. Akalework, A. K. Agegnehu, S. Y. Cheng and B. J. Hwang, *J. Taiwan Inst. Chem. Eng.*, 2017, **74**, 154.

53 I. Jiménez-Morales, S. Cavaliere, D. Jones and J. Rozière, *Phys. Chem. Chem. Phys.*, 2018, **20**, 8765.

54 R. A. M. Esfahani and E. B. Easton, *Appl. Catal., B*, 2020, **268**, 118743.

55 S. Y. Huang, P. Ganesan and B. N. Popov, *Appl. Catal., B*, 2011, **102**, 71.

56 A. Kumar and V. Ramani, *ACS Catal.*, 2014, **4**, 1516.

57 A. Pătru, A. Rabis, S. E. Temmel, R. Kotz and T. J. Schmidt, *Catal. Today*, 2016, **262**, 161.

58 P. Dhanasekaran, S. V. Selvaganesh and S. D. Bhat, *New J. Chem.*, 2017, **41**, 13012.

59 S. Matsumoto, M. Nagamine, Z. Noda, J. Matsuda, S. M. Lyth, A. Hayashi and K. Sasaki, *J. Electrochem. Soc.*, 2018, **165**, F1164.

60 C. Takei, R. Kobayashi, Y. Mizushita, Y. Hiramitsu, K. Kakinuma and M. Uchida, *J. Electrochem. Soc.*, 2018, **165**, F1300.

61 C. He, X. Wang, S. Sankarasubramanian, A. Yadav, K. Bhattacharyya, X. Liang and V. Ramani, *ACS Appl. Energy Mater.*, 2020, **3**, 5774.

62 M. Zhang, Y. Wang, Y. Zhang, J. Song, Y. Si, J. Yan, C. Ma, Y. T. Liu, J. Yu and B. Ding, *Angew. Chem., Int. Ed.*, 2020, **59**, 23252.

63 M. Marezio and P. D. Dernier, *J. Solid State Chem.*, 1970, **3**, 340.

64 M. Chisaka, W. Nagano, S. Takahashi, B. Delgertsetseg, H. Wakita and T. Takeguchi, *J. Electroanal. Chem.*, 2023, **934**, 117308.

65 R. A. M. Esfahani, S. K. Vankova, A. H. A. M. Videla and S. Specchia, *Appl. Catal., B*, 2017, **201**, 419.

66 R. A. M. Esfahani, I. I. Ebralidze, S. Specchia and E. B. Easton, *J. Mater. Chem. A*, 2018, **6**, 14805.

67 S. Y. Huang, P. Ganesan, S. Park and B. N. Popov, *J. Am. Chem. Soc.*, 2009, **131**, 13898.

68 X. Liu, X. Wu and K. Scott, *Catal. Sci. Technol.*, 2014, **4**, 3891.

69 V. T. T. Ho, C. J. Pan, J. Rick, W. N. Su and B. J. Hwang, *J. Am. Chem. Soc.*, 2011, **133**, 11716.

70 M. C. Tsai, T. T. Nguyen, N. G. Akalework, C. J. Pan, J. Rick, Y. F. Liao, W. N. Su and B. J. Hwang, *ACS Catal.*, 2016, **6**, 6551.

71 B. J. Hsieh, M. C. Tsai, C. J. Pan, W. N. Su, J. Rick, J. F. Lee, Y. W. Yang and B. J. Hwang, *NPG Asia Mater.*, 2017, **9**, e403.

72 B. J. Hsieh, M. C. Tsai, C. J. Pan, W. N. Su, J. Rick, H. L. Chou, J. F. Lee and B. J. Hwang, *Electrochim. Acta*, 2017, **224**, 452.

73 T. N. Geppert, M. Bosund, M. Putkonen, B. M. Stühmeier, A. T. Pasanen, P. Heikkilä, H. A. Gasteiger and H. A. El-Sayed, *J. Electrochem. Soc.*, 2020, **167**, 084517.

74 S. von Kraemer, K. Wikander, G. Lindbergh, A. Lundblad and A. E. C. Palmqvist, *J. Power Sources*, 2008, **180**, 185.

75 N. G. Akalework, C. J. Pan, W. N. Su, J. Rick, M. C. Tsai, J. F. Lee, J. M. Lin, L. D. Tsai and B. J. Hwang, *J. Mater. Chem.*, 2012, **22**, 20977.

76 K. W. Park and K. S. Seol, *Electrochem. Commun.*, 2007, **9**, 2256.

77 T. B. Do, M. Cai, M. S. Ruthkosky and T. E. Moylan, *Electrochim. Acta*, 2010, **55**, 8013.

This journal is © The Royal Society of Chemistry 2024

J. Mater. Chem. A, 2024, **12**, 18636–18673 | 18669

78 L. Chevallier, A. Bauer, S. Cavaliere, R. Hui, J. Rozière and D. J. Jones, *ACS Appl. Mater. Interfaces*, 2012, **4**, 1752.

79 J. H. Kim, G. Kwon, H. Lim, C. Zhu, H. You and Y. T. Kim, *J. Power Sources*, 2016, **320**, 188.

80 S. Y. Huang, P. Ganesan and B. N. Popov, *Appl. Catal., B*, 2010, **96**, 224.

81 C. He, S. Sankarasubramanian, I. Matanovic, P. Atanassov and V. Ramani, *ChemSusChem*, 2019, **12**, 3468.

82 R. D. Shannon, *Acta Crystallogr., Sect. A: Found. Crystallogr.*, 1976, **32**, 751.

83 Y. Ma, T. Nagai, Y. Inoue, K. Ikegami, Y. Kuroda, K. Matsuzawa, T. W. Napporn, Y. Liu, S. Mitsushima and A. Ishihara, *Mater. Des.*, 2021, **203**, 109623.

84 A. Kumar and V. Ramani, *J. Electrochem. Soc.*, 2013, **160**, F1207.

85 M. T. Anwar, X. Yan, S. Shen, N. Husnain, F. Zhu, L. Luo and J. Zhang, *Int. J. Hydrogen Energy*, 2017, **42**, 30750.

86 J. H. Kim, G. Kwon, H. Lim, C. Zhu, H. You and Y. T. Kim, *J. Power Sources*, 2016, **320**, 188.

87 K. J. Noh, H. Im, C. Lim, M. G. Jang, I. Nam and J. W. Han, *Chem. Eng. J.*, 2022, **427**, 131568.

88 A. Bharti and G. Cheruvally, *J. Power Sources*, 2017, **363**, 413.

89 C. V. Subban, Q. Zhou, A. Hu, T. E. Moylan, F. T. Wagner and F. J. DiSalvo, *J. Am. Chem. Soc.*, 2010, **132**, 17531.

90 A. V. Nguyen, T. T. Huynh, H. Q. Pham, V. T. T. Thi Phan, S. T. Nguyen and V. T. T. Ho, *Int. J. Hydrogen Energy*, 2019, **44**, 2361.

91 T. M. Phan, K. Im and J. Kim, *Appl. Surf. Sci.*, 2023, **611**, 155740.

92 E. Lee, C. Park, D. W. Lee, G. Lee, H. Y. Park, J. H. Jang, H. J. Kim, Y. E. Sung, Y. Tak and S. J. Yoo, *ACS Catal.*, 2020, **10**, 12080.

93 P. Dhanasekaran, S. V. Selvaganesh and S. D. Bhat, *J. Power Sources*, 2016, **304**, 360.

94 C. P. Lo, G. Wang, A. Kumar and V. Ramani, *Appl. Catal., B*, 2013, **140–141**, 133.

95 W. D. Ryden, A. W. Lawson and C. C. Sartain, *Phys. Rev. B: Solid State*, 1970, **1**, 1494.

96 S. J. Tauster, *Acc. Chem. Res.*, 1987, **20**, 389.

97 D. Banham, S. Ye, A. O'Toole, A. Lemke and E. Eisenbraun, *Nano Energy*, 2016, **27**, 157.

98 M. Eckardt, C. Gebauer, Z. Jusys, M. Wassner, N. Hüsing and R. J. Behm, *J. Power Sources*, 2018, **400**, 580.

99 B. M. Stühmeier, S. Selve, M. U. M. Patel, T. N. Geppert, H. A. Gasteiger and H. A. El-Sayed, *ACS Appl. Energy Mater.*, 2019, **2**, 5534.

100 E. Hornberger, A. Bergmann, H. Schmies, S. Kühl, G. Wang, J. Drnec, D. J. S. Sandbeck, V. Ramani, S. Cherevko, K. J. J. Mayrhofer and P. Strasser, *ACS Catal.*, 2018, **8**, 9675.

101 A. Masao, S. Noda, F. Takasaki, K. Ito and K. Sasaki, *Electrochem. Solid State Lett.*, 2009, **12**, B119.

102 K. Kakinuma, M. Uchida, T. Kamino, H. Uchida and M. Watanabe, *Electrochim. Acta*, 2011, **56**, 2881.

103 K. Kakinuma, Y. Chino, Y. Senoo, M. Uchida, T. Kamino, H. Uchida, S. Deki and M. Watanabe, *Electrochim. Acta*, 2013, **110**, 316.

104 Y. Senoo, K. Kakinuma, M. Uchida, H. Uchida, S. Deki and M. Watanabe, *RSC Adv.*, 2014, **4**, 32180.

105 Y. Senoo, K. Taniguchi, K. Kakinuma, M. Uchida, H. Uchida, S. Deki and M. Watanabe, *Electrochem. Commun.*, 2015, **51**, 37.

106 M. Inaba, R. Murase, T. Takeshita, K. Yano, S. Kosaka, N. Takahashi, N. Isomura, K. Oh-Ishi, W. Yoshimune, K. Tsuchiya, T. Nobukawa and K. Kodama, *ACS Appl. Mater. Interfaces*, 2024, **16**, 10295.

107 F. Takasaki, S. Matsuie, Y. Takabatake, Z. Noda, A. Hayashi, Y. Shiratori, K. Ito and K. Sasaki, *J. Electrochem. Soc.*, 2011, **158**, B1270.

108 M. Uchida, Y. Fukuoka, Y. Sugawara, N. Eda and A. Ohta, *J. Electrochem. Soc.*, 1996, **143**, 2245.

109 K. Kakinuma, R. Kobayashi, A. Iiyama and M. Uchida, *J. Electrochem. Soc.*, 2018, **165**, J3083.

110 G. Shi, T. Tano, D. A. Tryk, A. Iiyama, M. Uchida and K. Kakinuma, *ACS Catal.*, 2021, **11**, 5222.

111 K. Kakinuma, M. Hayashi, T. Hashimoto, A. Iiyama and M. Uchida, *ACS Appl. Energy Mater.*, 2020, **3**, 6922.

112 G. Shi, T. Hashimoto, D. A. Tryk, T. Tano, A. Iiyama, M. Uchida and K. Kakinuma, *Electrochim. Acta*, 2021, **390**, 138894.

113 S. Cavaliere, S. Subianto, I. Savych, M. Tillard, D. J. Jones and J. Rozière, *J. Phys. Chem. C*, 2013, **117**, 18298.

114 S. Cavaliere, I. Jiménez-Morales, G. Ercolano, I. Savych, D. Jones and J. Rozière, *ChemElectroChem*, 2015, **2**, 1966.

115 I. Jiménez-Morales, S. Cavaliere, M. Dupont, D. Jones and J. Rozière, *Sustainable Energy Fuels*, 2019, **3**, 1526.

116 G. Cognard, G. Ozouf, C. Beauger, G. Berthomé, D. Riassetto, L. Dubau, R. Chattot, M. Chatenet and F. Maillard, *Appl. Catal., B*, 2017, **201**, 381.

117 C. He, S. Sankarasubramanian, A. Ells, J. Parrondo, C. C. Gumeci, M. Kodali, I. Matanovic, A. K. Yadav, K. Bhattacharyya, N. Dale, P. Atanassov and V. K. Ramani, *ACS Catal.*, 2021, **11**, 7006.

118 D. Jalalpoor, D. Göhl, P. Paciok, M. Heggen, J. Knossalla, I. Radev, V. Peinecke, C. Weidenthaler, K. J. J. Mayrhofer, M. Ledendecker and F. Schüth, *J. Electrochem. Soc.*, 2021, **168**, 024502.

119 G. Ozouf, G. Cognard, F. Maillard, M. Chatenet, L. Guétaz, M. Heitzmann, P. A. Jacques and C. Beauger, *J. Electrochem. Soc.*, 2018, **165**, F3036.

120 V. Yarlagadda, M. K. Carpenter, T. E. Moylan, R. S. Kukreja, R. Koestner, W. Gu, L. Thompson and A. Kongkanand, *ACS Energy Lett.*, 2018, **3**, 618.

121 T. Yoshizumi, H. Kubo and M. Okumura, *SAE Tech. Pap. Ser.*, 2021, DOI: **10.4271/2021-01-0740**.

122 P. Zhang, S. Y. Huang and B. N. Popov, *J. Electrochem. Soc.*, 2010, **157**, B1163.

123 Z. Lin, J. Liu, S. Li, J. Liang, X. Liu, L. Xie, G. Lu, J. Han, Y. Huang and Q. Li, *Adv. Funct. Mater.*, 2023, **33**, 2211638.

124 S. Li, J. Liu, J. Liang, Z. Lin, X. Liu, Y. Chen, G. Lu, C. Wang, P. Wei, J. Han, Y. Huang, G. Wu and Q. Li, *Appl. Catal., B*, 2023, **320**, 122017.

125 K. Y. Chen and A. C. C. Tseung, *J. Electrochem. Soc.*, 1996, **143**, 2703.

18670 | *J. Mater. Chem. A*, 2024, **12**, 18636–18673

This journal is © The Royal Society of Chemistry 2024

126 V. Raghuveer and B. Viswanathan, *J. Power Sources*, 2005, **144**, 1.

127 H. Chhina, S. Campbell and O. Kesler, *J. Electrochem. Soc.*, 2007, **154**, B533.

128 Y. Liu, S. Shrestha and W. E. Mustain, *ACS Catal.*, 2012, **2**, 456.

129 S. Kumar, S. N. Bhange, R. Soni and S. Kurungot, *ACS Appl. Energy Mater.*, 2020, **3**, 1908.

130 T. Minami, *Thin Solid Films*, 2008, **516**, 5822.

131 H. Chhina, S. Campbell and O. Kesler, *J. Power Sources*, 2006, **161**, 893.

132 Y. Liu and W. E. Mustain, *J. Am. Chem. Soc.*, 2013, **135**, 530.

133 H. Schmies, A. Bergmann, J. Drnec, G. Wang, D. Teschner, S. Kühl, D. J. S. Sandbeck, S. Cherevko, M. Gocyla, M. Shviro, M. Heggen, V. Ramani, R. E. Dunin-Borkowski, K. J. J. Mayrhofer and P. Strasser, *Adv. Energy Mater.*, 2018, **8**, 1701663.

134 Y. Cheng, X. Zhao, Y. Yu, L. Chen, T. Cheng, J. Huang, Y. Liu, M. Harada, A. Ishihara and Y. Wang, *J. Power Sources*, 2020, **446**, 227332.

135 W. Guo, L. Cheng, X. Gao, J. Xu, C. Chen, P. Liu, D. He, L. Tian, J. Song, H. Zhou and Y. Wu, *ACS Catal.*, 2023, **13**, 5397.

136 O. A. Baturina, Y. Garsany, T. J. Zega, R. M. Stroud, T. Schull and K. E. Swider-Lyons, *J. Electrochem. Soc.*, 2008, **155**, B1314.

137 W. Gao, Z. Zhang, M. Dou and F. Wang, *ACS Catal.*, 2019, **9**, 3278.

138 Q. Jia, S. Ghoshal, J. Li, W. Liang, G. Meng, H. Che, S. Zhang, Z. F. Ma and S. Mukerjee, *J. Am. Chem. Soc.*, 2017, **139**, 7893.

139 C. Xu, J. Yang, E. Liu, Q. Jia, G. M. Veith, G. Nair, S. DiPietro, K. Sun, J. Chen, P. Pietrasz, Z. Lu, M. Jagner, K. K. Gath, S. Mukerjee and J. R. Waldecker, *J. Power Sources*, 2020, **451**, 227709.

140 S. Takenaka, H. Matsumori, K. Nakagawa, H. Matsune, E. Tanabe and M. Kishida, *J. Phys. Chem. C*, 2007, **111**, 15133.

141 Y. Suzuki, A. Ishihara, S. Mitsushima, N. Kamiya and K. Ota, *Electrochem. Solid State Lett.*, 2007, **10**, B105.

142 G. Shi, T. Tano, D. A. Tryk, A. Iiyama, M. Uchida, Y. Kuwauchi, A. Masuda and K. Kakinuma, *J. Catal.*, 2022, **407**, 300.

143 J. K. Nørskov, J. Rossmeisl, A. Logadottir, L. Lindqvist, J. R. Kitchin, T. Bligaard and H. Jónsson, *J. Phys. Chem. B*, 2004, **108**, 17886.

144 S. Siahrostami, S. J. Villegas, A. H. B. Mostaghimi, S. Back, A. B. Farimani, H. Wang, K. A. Persson and J. Montoya, *ACS Catal.*, 2020, **10**, 7495.

145 F. Ando, T. Gunji, T. Tanabe, I. Fukano, H. D. Abruña, J. Wu, T. Ohsaka and F. Matsumoto, *ACS Catal.*, 2021, **11**, 9317.

146 B. Avasarala, T. Murray, W. Li and P. Haldar, *J. Mater. Chem.*, 2009, **19**, 1803.

147 B. Avasarala and P. Haldar, *Electrochim. Acta*, 2010, **55**, 9024.

148 N. C. Saha and H. G. Tompkins, *J. Appl. Phys.*, 1992, **72**, 3072.

149 K. Kakinuma, Y. Wakasugi, M. Uchida, T. Kamino, H. Uchida and M. Watanabe, *Electrochemistry*, 2011, **79**, 399.

150 K. Kakinuma, Y. Wakasugi, M. Uchida, T. Kamino, H. Uchida, S. Deki and M. Watanabe, *Electrochim. Acta*, 2012, **77**, 279.

151 H. Shintani, K. Kakinuma, H. Uchida, M. Watanabe and M. Uchida, *J. Power Sources*, 2015, **280**, 593.

152 A. Seifitokaldani and O. Savadogo, *Electrochim. Acta*, 2015, **167**, 237.

153 H. Shin, H. Kim, D. Y. Chung, J. M. Yoo, S. Weon, W. Choi and Y. E. Sung, *ACS Catal.*, 2016, **6**, 3914.

154 H. Nan, D. Dang and X. L. Tian, *J. Mater. Chem. A*, 2018, **6**, 6065.

155 H. Matsui, A. Shoji, C. Chen, X. Zhao, T. Uruga and M. Tada, *Catal. Sci. Technol.*, 2024, **14**, 1501.

156 Z. Pan, Y. Xiao, Z. Fu, G. Zhan, S. Wu, C. Xiao, G. Hu and Z. Wei, *J. Mater. Chem. A*, 2014, **2**, 13966.

157 S. Jiang, B. Yi, H. Zhang, W. Song, Y. Bai, H. Yu and Z. Shao, *ChemElectroChem*, 2016, **3**, 734.

158 M. K. Debe, A. K. Schmoeckel, G. D. Vernstrom and R. Atanasoski, *J. Power Sources*, 2006, **161**, 1002.

159 W. Li, X. Wang, Z. Chen, M. Waje and Y. Yan, *Langmuir*, 2005, **21**, 9386.

160 A. Perego, G. Giuffredi, P. Mazzolini, M. Colombo, R. Brescia, M. Prato, D. C. Sabarirajan, I. V. Zenyuk, F. Bossola, V. D. Santo, A. Casalegno and F. D. Fonzo, *ACS Appl. Energy Mater.*, 2019, **2**, 1911.

161 Y. Xiao, G. Zhan, Z. Fu, Z. Pan, C. Xiao, S. Wu, C. Chen, G. Hu and Z. Wei, *J. Power Sources*, 2015, **284**, 296.

162 X. Tian, J. Luo, H. Nan, H. Zou, R. Chen, T. Shu, X. Li, Y. Li, H. Song, S. Liao and R. R. Adzic, *J. Am. Chem. Soc.*, 2016, **138**, 1575.

163 Q. Liu, L. Du, G. Fu, Z. Cui, Y. Li, D. Dang, X. Gao, Q. Zheng and J. B. Goodenough, *Adv. Energy Mater.*, 2019, **9**, 1803040.

164 C. Walling, *Acc. Chem. Res.*, 1975, **8**, 125.

165 I. A. Salem, M. El-Maazawi and A. B. Zaki, *Int. J. Chem. Kinet.*, 2000, **32**, 643.

166 T. Kinumoto, M. Inaba, Y. Nakayama, K. Ogata, R. Umebayashi, A. Tasaka, Y. Iriyama, T. Abe and Z. Ogumi, *J. Power Sources*, 2006, **158**, 1222.

167 S. Jing, L. Luo, S. Yin, F. Huang, Y. Jia, Y. Wei, Z. Sun and Y. Zhao, *Appl. Catal., B*, 2014, **147**, 897.

168 J. Yin, L. Wang, C. Tian, T. Tan, G. Mu, L. Zhao and H. Fu, *Chem.–Eur. J.*, 2013, **19**, 13979.

169 L. C. Tsai, T. K. Chin, W. S. Liu and T. P. Perng, *ACS Appl. Energy Mater.*, 2020, **3**, 11610.

170 Q. Li, L. Li, X. Yu, X. Wu, Z. Xie, X. Wang, Z. Lu, X. Zhang, Y. Huang and X. Yang, *Chem. Eng. J.*, 2020, **399**, 125827.

171 K. Uosaki, G. Elumalai, H. Noguchi, T. Masuda, A. Lyalin, A. Nakayama and T. Taketsugu, *J. Am. Chem. Soc.*, 2014, **136**, 6542.

172 G. Elumalai, H. Noguchi, A. Lyalin, T. Taketsugu and K. Uosaki, *Electrochem. Commun.*, 2016, **66**, 53.

This journal is © The Royal Society of Chemistry 2024

J. Mater. Chem. A, 2024, **12**, 18636–18673 | **18671**

173 M. Dou, M. Hou, H. Zhang, G. Li, W. Lu, Z. Wei, Z. Shao and B. Yi, *ChemSusChem*, 2012, **5**, 945.

174 M. Dou, M. Hou, D. Liang, W. Lu, Z. Shao and B. Yi, *Electrochim. Acta*, 2013, **92**, 468.

175 T. Ioroi and K. Yasuda, *J. Power Sources*, 2020, **450**, 227656.

176 Y. Li, W. Song, G. Jiang, Y. Yang, H. Yu, Z. Shao, F. Duan and Y. Yang, *Front. Energy*, 2022, **16**, 852.

177 *U.S. Geological Survey, Mineral Commodity Summaries*, 2024, p. 136, DOI: 10.3133/mcs2024.

178 X. Zhou, H. Ji, B. Li and C. Zhang, *ACS Omega*, 2020, **5**, 10099.

179 J. Wang, X. Zhou, B. Li, D. Yang, H. Lv, Q. Xiao, P. Ming, X. Wei and C. Zhang, *Int. J. Hydrogen Energy*, 2020, **45**, 8930.

180 E. You, M. Min, S. A. Jin, T. Kim and C. Pak, *J. Electrochem. Soc.*, 2018, **165**, F3094.

181 T. Y. Kim, S. W. Lee and C. Pak, *J. Ind. Eng. Chem.*, 2020, **85**, 87.

182 Y. Li, L. Zhao, X. Du, W. Gao, C. Zhang, H. Chen, X. He, C. Wang and Z. Mao, *Chem. Eng. J.*, 2023, **461**, 141823.

183 J. Liao, S. Zaman, Y. Wang, M. Yang, L. Yang, M. Chen and H. Wang, *ACS Appl. Mater. Interfaces*, 2023, **15**, 4092.

184 Y. Wang, Y. Jiang, J. Liao, Z. Li, T. Zhao and L. Zeng, *ACS Appl. Mater. Interfaces*, 2022, **14**, 56867.

185 B. Favelukis, S. Chakrabartty, V. Kumar, S. H. Kim, A. El-Zoka, M. Krämer, D. Raabe, B. Gault, N. Eliaz, A. Natan, M. Sokol and B. A. Rosen, *Adv. Funct. Mater.*, 2024, **34**, 2309749.

186 B. Genorio, D. Strmcnik, R. Subbaraman, D. Tripkovic, G. Karapetrov, V. R. Stamenkovic, S. Pejovnik and N. M. Marković, *Nat. Mater.*, 2010, **9**, 998.

187 B. Genorio, R. Subbaraman, D. Strmcnik, D. Tripkovic, V. R. Stamenkovic and N. M. Markovic, *Angew. Chem., Int. Ed.*, 2011, **50**, 5468.

188 S. W. Yun, S. A. Park, T. J. Kim, J. H. Kim, G. W. Pak and Y. T. Kim, *ChemSusChem*, 2017, **10**, 489.

189 B. M. Stühmeier, A. M. Damjanović, K. Rodewald and H. A. Gasteiger, *J. Power Sources*, 2023, **558**, 232572.

190 J. Jang, M. Sharma, D. Choi, Y. S. Kang, Y. Kim, J. Min, H. Sung, N. Jung and S. J. Yoo, *ACS Appl. Mater. Interfaces*, 2019, **11**, 27735.

191 H. Shintani, Y. Kojima, K. Kakinuma, M. Watanabe and M. Uchida, *J. Power Sources*, 2015, **294**, 292.

192 G. Shen, J. Liu, H. B. Wu, P. Xu, F. Liu, C. Tongsh, K. Jiao, J. Li, M. Liu, M. Cai, J. P. Lemmon, G. Soloveichik, H. Li, J. Zhu and Y. Lu, *Nat. Commun.*, 2020, **11**, 1191.

193 J. Luo, H. Tang, X. Tian, S. Hou, X. Li, L. Du and S. Liao, *ACS Appl. Mater. Interfaces*, 2018, **10**, 3530.

194 R. Kamai, K. Kamiya, K. Hashimoto and S. Nakanishi, *Angew. Chem., Int. Ed.*, 2016, **55**, 13184.

195 M. Nagai, M. Yoshida and H. Tominaga, *Electrochim. Acta*, 2007, **52**, 5430.

196 S. Izhar and M. Nagai, *J. Power Sources*, 2008, **182**, 52.

197 S. Izhar, M. Yoshida and M. Nagai, *Electrochim. Acta*, 2009, **54**, 1255.

198 G. E. Haslam, X. Y. Chin and G. T. Burstein, *Phys. Chem. Chem. Phys.*, 2011, **13**, 12968.

199 P. D. Tran, A. Le Goff, J. Heidkamp, B. Jousselme, N. Guillet, S. Palacin, H. Dau, M. Fontecave and V. Artero, *Angew. Chem., Int. Ed.*, 2011, **50**, 1371.

200 T. N. Huan, R. T. Jane, A. Benayad, L. Guetaz, P. D. Tran and V. Artero, *Energy Environ. Sci.*, 2016, **9**, 940.

201 X. Yang, F. Zhao, Y. W. Yeh, R. S. Selinsky, Z. Chen, N. Yao, C. G. Tully, Y. Ju and B. E. Koel, *Nat. Commun.*, 2019, **10**, 1543.

202 M. Chisaka, T. Iijima, T. Yaguchi and Y. Sakurai, *Electrochim. Acta*, 2011, **56**, 4581.

203 M. Chisaka, Y. Suzuki, T. Iijima and Y. Sakurai, *J. Phys. Chem. C*, 2011, **115**, 20610.

204 J. Zhang, F. Coms and S. Kumaraguru, *J. Electrochem. Soc.*, 2021, **168**, 024520.

205 H. Xie, X. Xie, G. Hu, V. Prabhakaran, S. Saha, L. Gonzalez-Lopez, A. H. Phakatkar, M. Hong, M. Wu, R. Shahbazian-Yassar, V. Ramani, M. I. Al-Sheikhly, D. Jiang, Y. Shao and L. Hu, *Nat. Energy*, 2022, **7**, 281.

206 Y. Takasu, H. Fukunaga, H. S. Yang, T. Ohashi, M. Suzuki and W. Sugimoto, *Electrochim. Acta*, 2013, **105**, 224.

207 E. Proietti, F. Jaouen, M. Lefèvre, N. Larouche, J. Tian, J. Herranz and J. P. Dodelet, *Nat. Commun.*, 2011, **2**, 416.

208 C. H. Choi, C. Baldizzone, J. P. Grote, A. K. Schuppert, F. Jaouen and K. J. J. Mayrhofer, *Angew. Chem., Int. Ed.*, 2015, **54**, 12753.

209 K. Strickland, E. Miner, Q. Jia, U. Tylus, N. Ramaswamy, W. Liang, M. T. Sougrati, F. Jaouen and S. Mukerjee, *Nat. Commun.*, 2015, **6**, 7343.

210 Y. Shao, J. P. Dodelet, G. Wu and P. Zelenay, *Adv. Mater.*, 2019, **31**, 1807615.

211 X. Zhao, X. Yang, M. Wang, S. Hwang, S. Karakalos, M. Chen, Z. Qiao, L. Wang, B. Liu, Q. Ma, D. A. Cullen, D. Su, H. Yang, H. Y. Zang, Z. Feng and G. Wu, *Appl. Catal., B*, 2020, **279**, 119400.

212 H. Zhang, L. Osmieri, J. H. Park, H. T. Chung, D. A. Cullen, K. C. Neyerlin, D. J. Myers and P. Zelenay, *Nat. Catal.*, 2022, **5**, 455.

213 X. Xie, C. He, B. Li, Y. He, D. A. Cullen, E. C. Wegener, A. J. Kropf, U. Martinez, Y. Cheng, M. H. Engelhard, M. E. Bowden, M. Song, T. Lemmon, X. S. Li, Z. Nie, J. Liu, D. J. Myers, P. Zelenay, G. Wang, G. Wu, V. Ramani and Y. Shao, *Nat. Catal.*, 2020, **3**, 1044.

214 M. Chen, X. Li, F. Yang, B. Li, T. Stracensky, S. Karakalos, S. Mukerjee, Q. Jia, D. Su, G. Wang, G. Wu and H. Xu, *ACS Catal.*, 2020, **10**, 10523.

215 S. Gottesfeld, *J. Electrochem. Soc.*, 2022, **169**, 124518.

216 K. Kodama, T. Nagai, A. Kuwaki, R. Jinnouchi and Y. Morimoto, *Nat. Nanotechnol.*, 2021, **16**, 140.

217 K. Lee, A. Ishihara, S. Mitsushima, N. Kamiya and K. Ota, *Electrochim. Acta*, 2004, **49**, 3479.

218 Y. Liu, A. Ishihara, S. Mitsushima, N. Kamiya and K. Ota, *Electrochem. Solid State Lett.*, 2005, **8**, A400.

219 J. H. Kim, A. Ishihara, S. Mitsushima, N. Kamiya and K. Ota, *Electrochim. Acta*, 2007, **52**, 2492.

220 S. Doi, A. Ishihara, S. Mitsushima, N. Kamiya and K. Ota, *J. Electrochem. Soc.*, 2007, **154**, B362.

18672 | *J. Mater. Chem. A*, 2024, **12**, 18636–18673

This journal is © The Royal Society of Chemistry 2024

221 A. Ishihara, S. Doi, S. Mitsushima and K. Ota, *Electrochim. Acta*, 2008, **53**, 5442.

222 K. Ukita, A. Ishihara, Y. Ohgi, K. Matsuzawa, S. Mitsushima and K. Ota, *Electrochemistry*, 2011, **79**, 340.

223 M. Chisaka, A. Ishihara, H. Morioka, T. Nagai, S. Yin, Y. Ohgi, K. Matsuzawa, S. Mitsushima and K. I. Ota, *ACS Omega*, 2017, **2**, 678.

224 M. Chisaka, Y. Yamamoto, N. Itagaki and Y. Hattori, *ACS Appl. Energy Mater.*, 2018, **1**, 211.

225 M. Chisaka, Y. Ando and N. Itagaki, *J. Mater. Chem. A*, 2016, **4**, 2501.

226 M. Chisaka, T. Abe, R. Xiang, S. Maruyama and H. Daiguji, *Phys. Chem. Chem. Phys.*, 2022, **24**, 29328.

227 M. Chisaka, R. Xiang, S. Maruyama and H. Daiguji, *ACS Appl. Energy Mater.*, 2020, **3**, 9866.

228 M. Chisaka, R. Xiang, S. Maruyama and H. Daiguji, *Energy Fuels*, 2022, **36**, 539.

229 M. Chisaka, J. A. Shamim, W. L. Hsu and H. Daiguji, *J. Mater. Chem. A*, 2024, **12**, 11277.

230 X. L. Tian, L. Wang, B. Chi, Y. Xu, S. Zaman, K. Qi, H. Liu, S. Liao and B. Y. Xia, *ACS Catal.*, 2018, **8**, 8970.

231 G. Liu, H. M. Zhang, M. R. Wang, H. X. Zhong and J. Chen, *J. Power Sources*, 2007, **172**, 503.

232 J. Seo, D. H. Anjum, K. Takanabe, J. Kubota and K. Domen, *Electrochim. Acta*, 2014, **149**, 76.

233 M. Chisaka, A. Ishihara, N. Uehara, M. Matsumoto, H. Imai and K. Ota, *J. Mater. Chem. A*, 2015, **3**, 16414.

234 M. Chisaka and H. Muramoto, *ChemElectroChem*, 2014, **1**, 544.

235 G. Zhang, D. Sebastián, X. Zhang, Q. Wei, C. Lo Vecchio, J. Zhang, V. Baglio, W. Wang, S. Sun, A. S. Aricò and A. C. Tavares, *Adv. Energy Mater.*, 2020, **10**, 2000075.

236 T. Sun, Q. Wu, R. Che, Y. Bu, Y. Jiang, Y. Li, L. Yang, X. Wang and Z. Hu, *ACS Catal.*, 2015, **5**, 1857.

237 R. Chenitz, U. I. Kramm, M. Lefèvre, V. Glibin, G. Zhang, S. Sun and J. P. Dodelet, *Energy Environ. Sci.*, 2018, **11**, 365.

238 C. Gebauer, J. Fischer, M. Wassner, T. Diemant, J. Bansmann, N. Hüsing and R. J. Behm, *Electrochim. Acta*, 2014, **146**, 335.

239 Y. Du, Z. Dohnálek and I. Lyubinetsky, *J. Phys. Chem. C*, 2008, **112**, 2649.

240 Y. Du, N. A. Deskins, Z. Zhang, Z. Dohnálek, M. Dupuis and I. Lyubinetsky, *Phys. Chem. Chem. Phys.*, 2010, **12**, 6337.

241 S. Wendt, P. T. Sprunger, E. Lira, G. K. H. Madsen, Z. Li, J. Ø. Hansen, J. Matthiesen, A. Blekinge-Rasmussen, E. Laegsgaard, B. Hammer and F. Besenbacher, *Science*, 2008, **320**, 1755.

242 M. Chisaka, *Phys. Chem. Chem. Phys.*, 2018, **20**, 15613.

243 M. Chisaka and H. Morioka, *Catal. Sci. Technol.*, 2019, **9**, 611.

244 S. Trasatti, *Pure Appl. Chem.*, 1986, **58**, 955.

245 M. García-Mota, A. Vojvodic, H. Metiu, I. C. Man, H. Y. Su, J. Rossmeisl and J. K. Nørskov, *ChemCatChem*, 2011, **3**, 1607.

246 H. A. Gasteiger, J. E. Panels and S. G. Yan, *J. Power Sources*, 2004, **127**, 162.

247 M. Chisaka and H. Daiguji, *Electrochem. Commun.*, 2006, **8**, 1304.

248 S. Henning, R. Shimizu, J. Herranz, L. Kühn, A. Eychmüller, M. Uchida, K. Kakinuma and T. J. Schmidt, *J. Electrochem. Soc.*, 2018, **165**, F3001.

249 T. Tamaki, H. Kuroki, S. Ogura, T. Fuchigami, Y. Kitamoto and T. Yamaguchi, *Energy Environ. Sci.*, 2015, **8**, 3545.

250 P. von Tettau, S. Sterlepper, P. Mauermann, M. Wick, S. Tinz, M. Jesser, M. Walters and S. Pischinger, *Int. J. Hydrogen Energy*, 2024, **52**, 1127.

251 N. Goswami, A. N. Mistry, J. Grunewald, T. F. Fuller and P. P. Mukherjee, *J. Electrochem. Soc.*, 2020, **167**, 084519.

252 N. Goswami, J. B. Grunewald, T. F. Fuller and P. P. Mukherjee, *J. Mater. Chem. A*, 2022, **10**, 15101.

253 N. Goswami, J. B. Grunewald, T. F. Fuller and P. P. Mukherjee, *Electrochim. Acta*, 2024, **486**, 144143.

254 N. Goswami, K. Chen, X. Wang, J. S. Spendelow, R. L. Borup and P. P. Mukherjee, *Chem. Eng. J.*, 2024, **484**, 149672.

This journal is © The Royal Society of Chemistry 2024

J. Mater. Chem. A, 2024, **12**, 18636–18673 | 18673